Numerical Simulations of Bubble Dynamics Near Viscoelastic Media

by

Mauro Rodriguez

A dissertation submitted in partial fulfillment
of the requirements for the degree of
Doctor of Philosophy
(Mechanical Engineering)
in the University of Michigan
2018

Doctoral Committee:

Associate Professor Eric Johnsen, Chair
Professor Steven L. Ceccio
Professor Krishnakumar Garikipati
Professor Ronald G. Larson
Professor Kenneth G. Powell

Mauro Rodriguez
mrdz@umich.edu
ORCID iD: # 0000-0003-0545-0265

DEDICATION

For all my kin from La Villita in Chicago, because I love you so.

ACKNOWLEDGMENTS

I am forever grateful to my advisor, Prof. Eric Johnsen, for his seemingly eternal patience and proactive diligence towards furthering my success as a scholar. Without his mentorship and guidance this dissertation and my development would not have been possible. My deepest gratitude to the dissertation committee members, Prof. Steven L. Ceccio, Prof. Krishnakumar Garikipati, Prof. Ronald G. Larson, and Prof. Kenneth G. Powell for your guidance and advice in the development of this dissertation.

I am grateful to all of my Scientific Computing and Flow Physics lab colleagues and friends: Shahaboddin, Brandon, Marc, Kevin, Kazuya, Siddhesh, Suyash, Samuel, Lauren, Minki, Griffin, Michael, and Grace for making my doctoral journey intellectually stimulating and enjoyable. All of you are brilliant and I am grateful for your mentorship and friendship. I want to thank Dean Alec Gallimore, Prof. Alan Wineman, Prof. Smadar Karni, Prof. William Schultz, Prof. Krzysztof Fidkowski, Prof. Michael Solomon, Prof. Susan Montgomery, and Prof. John Foster for all their wisdom and guidance they have imparted onto me throughout these past six years. Having been part of numerous service and teaching roles at U-M, I am grateful to have worked alongside the both previous and current U-M staff, including Robert D. Scott, Derrick Scott, Hans Sowder, Tiffany Porties, Kim Elliot, and Shira Washington. Thank you to my friends at the Society of Hispanic Professional Engineers, U-M, Mario Gutierrez, Ariel Murphy, and Johanna Heureaux-Torres for making my doctoral experience enjoyable. A special thank you to Prof. Nayarana R. Aluru from my years at Illinois for taking the time and effort of guiding a young, Chicano

mechanical engineering undergraduate student to look at fluid mechanics with a child-like wonder and as a life-long pursuit. I am grateful to my family and community in Chicago for their support and being my inspiration throughout my life. I dedicate this dissertation to them as I make my life's work a bridge for the youth of my community. I especially dedicate this to my grandmother Maria Socorro Lupercio Rodriguez and aunt Maria Elena Rodriguez who passed away during the final week of me preparing this work, may they rest in peace.

This work was supported in part by the Ford Foundation Dissertation Writing Fellowship, the University of Michigan Rackham Graduate School Dissertation Writing Fellowship, University of Michigan Rackham Merit Fellowship, ONR grants N00014-12-1-0751 (under Dr. Ki-Han Kim) and N00014-17-1-2058 (under Dr. Timothy Bentley), and NSF grant number CBET 1253157. This work used resources at the Oak Ridge Leadership Computing Facility, a DOE Office of Science User Facility operated by the Oak Ridge National Laboratory, and the Blue Waters sustained-petascale computing project, which is supported by the National Science Foundation (awards OCI-0725070 and ACI-1238993) and the state of Illinois. Blue Waters is a joint effort of the University of Illinois at Urbana-Champaign and its National Center for Supercomputing Applications.

TABLE OF CONTENTS

LIST OF FIGURES

LIST OF TABLES

LIST OF ABBREVIATIONS

AUSM Advection Upstream Splitting Method

ESWL extracorporeal shock wave lithotripsy

EOS equation of state

FDS Flux-difference splitting

FVS flux-vector splitting

HDF hierarchical data format

NASG Noble-Abel Stiffened-Gas equation of state

TVD Total Variation Diminishing

RK Runge-Kutta

TVD Total Variation Diminishing

WENO Weighted Essentially Non-Oscillatory

ABSTRACT

Cavitation-induced damage occurs in a wide range of applications, including in naval hydrodynamics, medicine, and the Spallation Neutron Source. Local transient pressure decreases in liquid flow may give rise to explosive bubble growth and violent collapse, with shock waves produced at collapse interacting with neighboring solids. Although the mechanisms of erosion to hard, metallic solids can be predicted in relatively simple geometries, damage to soft materials (e.g., elastomeric coatings, soft tissue) or in confined geometries is less well understood. In such problems, the constitutive models describing the medium are non-trivial and include effects such as (nonlinear) elasticity, history (relaxation effects) and viscosity. As a result, the influence of the shock on the material and the response of the material to the shock are poorly understood.

To gain fundamental insights into cavitation-induced damage to both soft objects and rigid materials, we develop a novel Eulerian approach for numerical simulations of wave propagation in heterogeneous viscoelastic media. We extend the five-equations multiphase, interface-capturing model, based on the idea that all the materials (gases, liquids, solids) obey the same equation of state with spatially varying properties, to incorporate the desired constitutive relation. We consider problems in which the deformations are small, such that the substances can be described by linear viscoelastic constitutive relations. One difficulty is the calculation of strains in an Eulerian framework, which we address by using a hypoelastic model in which an objective time derivative (Lie derivative) of the constitutive relation is taken to evolve strain rates. The resulting numerical framework is a solution-adaptive, high-order interface-capturing approach for compressible, multiphase flows involving linear viscoelasticity at all speeds.

We then utilize this numerical framework to gain fundamental insights into cavitation damage

(i) in a confined geometry, (ii) in shock wave lithotripsy, and (iii) to rigid objects covered by an elastomeric coating. We examine the maximum stresses, pressures, and temperatures along/in rigid/compliant objects. We quantify the effect of confinement on an inertially collapsing bubble and determine the appropriate scaling governing the maximum pressures can predicted on the surfaces. We investigate the stresses produced to a model kidney stone due to a shock wave by examining the amplification of tensile stresses in the stone when a gas bubble is present. The impact loads on a polymeric coating relevant to naval engineering applications by shock-induced bubble collapse indicate how pitting and coating material ejection may take place by repeated cavitation events near the surface.

CHAPTER 1

Introduction

This chapter provides an introduction to cavitation bubble dynamics and its applications, in the context of cavitation erosion. Knowledge gaps on the mechanisms of cavitation erosion in confined geometries, biomedical ultrasound, and in naval engineering are discussed. The requirements for numerically solving multi-component, multiphase flows to gain fundamental insights on cavitation damage are briefly detailed. The chapter concludes by stating the research objectives and main contributions to the field.

1.1 Cavitation in Science and Engineering

Cavitation, the process primarily described by the formation and dynamics of vapor bubbles in a liquid flow, appears in a wide range of hydraulic applications, such as turbomachinery, naval structures, biomedical ultrasound, and combustion. Cavitation occurs due to local pressure reductions in a flow exceeding the tensional threshold in the surrounding liquid. As a result, nanometer-scale gas nuclei in the liquid grow via phase change to vapor bubbles (Brennen, 2013). This mechanically driven phenomenon contrasts with boiling, a thermally driven process, in which the temperature increase vaporizes the liquid. When the local pressure reduction in the flow is sufficient to lead to cavitation, multiple bubbles are formed and behave as a bubble cloud. Bubbles respond to the transient pressure variations (e.g. ultrasound waves, turbulent flow) by oscillating in volume. The oscillations eventually dampen due to dissipative mechanisms and, eventually, the bubbles achieve

equilibrium with their surroundings. In extreme cases, however, the inertia imparted from the surroundings dominates such that the bubbles collapse violently. Upon collapse, strong shock waves are emitted and interacting with the neighboring surface. After repeated and continuous impact loading, the surface is damaged by deforming or erosion.

Depending on the surroundings, individual cavitation bubbles can collapse symmetrically or asymmetrically. Under the idealization of a single bubble in an infinite sea of liquid, the vapor bubble collapse is spherical. This collapse causes the vapor inside the bubble to condense and concentrates energy into a volume several orders of magnitude smaller than its maximum volume. Eventually, the pressure build up is so great that the collapse is arrested and the bubble rebounds, i.e., grows again. As a result, a shock wave is generated and propagates into the surroundings (Rayleigh, 1917; Lauterborn & Kurz, 2010). Depending on the bubble size, this shock wave can impart high impact loads to the neighboring materials. For ductile materials, such as metals, the impact load may lead to material deformation (e.g., pitting) and loss (Kim *et al.*, 2014). Material failure occurs in brittle materials from internal reflections of this shock forming a tensile wave and lead to spallation (Lubock, 1989). Moreover, experimental studies demonstrate that spherical collapses are significantly stronger than asymmetrical ones due to the high-volume concentration and compression (De Chizelle *et al.*, 1995). However, cavitation vapor bubbles form and collapse in finite environments with elements that may break the symmetry, e.g., neighboring surfaces, adjacent bubbles in a bubble cloud, gravity, ultrasound waves, under which the collapse becomes asymmetric (Benjamin & Ellis, 1966). A re-entrant jet forms (see Fig. 1.1, (Crum, 1988)), which eventually impinges onto the distal side of the bubble thus producing a water-hammer shock.

The mechanisms of cavitation erosion are not fully understood. When approaching this problem from the single-bubble perspective, two important factors are known to play a role in erosion (Parsons & Cook, 1919; Kornfeld & Suvorov, 1944): (i) the radially propagating water-hammer shock and, (ii) direct impingement of the re-entrant jet onto the surface. Both mechanisms give rise to localized high-impact loads on the material surface. Although both phenomena have been investigated over the past few decades (Kornfeld & Suvorov, 1944; Benjamin & Ellis, 1966;

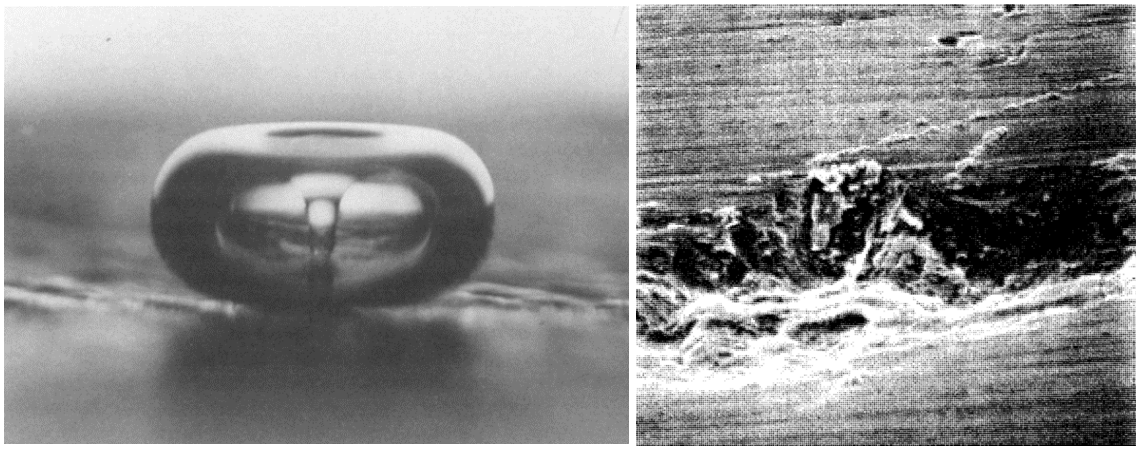

(a) Liquid jet.

(b) Erosion on brass plate.

Figure 1.1: Liquid jet produced collapsing cavitation bubble near a brass plate Crum (1988) and the resulting cavitation erosion. The bubble is approximately 1 mm across and plate is 2 mm thick.

Blake *et al.*, 1986; Brujan *et al.*, 2002; Lindau & Lauterborn, 2003), the extent to which one or the other mechanism is dominant remains unclear. Numerical efforts by Beig *et al.* (2018) have demonstrated with appropriate scalings the data can collapse and be predictable for certain kinds of problems.

The non-linear, fully-coupled behavior of the fluid motion during the bubble collapse, turbulence, and material undergoing finite and permanent deformations presents serious modeling challenges. In this thesis, three distinct thematic areas are considered in the context of cavitation erosion: cavitation under confinement, ultrasound-induced cavitation, and cavitation in naval hydrodynamic applications.

1.1.1 Confined Cavitation

Cavitation damage occurs in various applications in which the confined flow geometry and operating conditions play a critical role on the bubble dynamics. In these applications, the cavitation bubble diameter is on the order of the channel width such that confinement can affect the dynamics. Cavitation also plays an important role in the atomization process in sprays that typically involve jet with cross-sectional areas of a few millimeters square (Wang *et al.*, 2014; Bergeles *et al.*, 2015; Biçer & Sou, 2016). Ferns sporangia utilize cavitation to eject its spores akin to man-made cat-

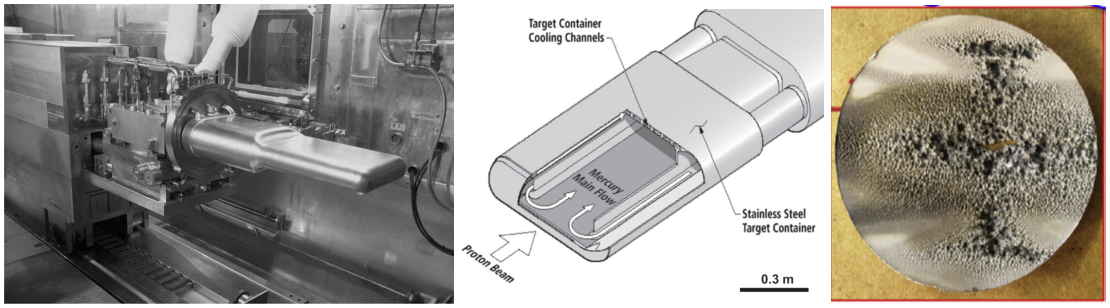

(a) Target module set-up. (b) Mercury flow target vessel. (c) Cavitation erosion.

Figure 1.2: Spallation Neutron Source (SNS) target module set-up and mercury target vessel Haines *et al.* (2014) resulting confined cavitation erosion in the target vessel Riemer *et al.* (2014).

apults (Noblin *et al.*, 2012) and snapping-shrimp produce cavitating bubbles by rapidly closing their claws to kill their prey (Versluis *et al.*, 2010). Cavitation is is the lifetime-limiting factor for the target used in the operation of the Spallation Neutron Source (SNS) at Oak Ridge National Laboratory (Haines *et al.*, 2014; Riemer *et al.*, 2014; Naoe *et al.*, 2016). In the SNS, a proton beam is fired into a mercury target vessel leading to a spallation process that produces an intense neutron beam. This process produces a shock wave that propagates through the mercury and interacts with the vessel walls. In addition, cavitation is generated and gives rise to erosion of the target, which limits the radiation power range and experiment duration (see Fig. 1.2).

Confined cavitation is challenging to study experimentally and has received limited attention in the literature. Confinement may affect the hydrodynamics of bubble collapse, particularly the re-entrant jet formation. For a single bubble inertially collapsing near a perfectly rigid wall, a jet forms on the distal side of the bubble relative to the wall (Naude & Ellis, 1961; Plesset & Chapman, 1971; Brujan *et al.*, 2002). Fluid from the surroundings is entrained into the bubble as the re-entrant jet forms. However, in a confined geometry (e.g., a channel) it is not clear what effect, if any, the boundaries could have on the re-entrant jet formation and cavitation damage. Additionally, a collapsing bubble generates outward propagating rarefaction waves, which subsequently interact with the bubble and affect the dynamics. The extent to which the rarefaction dynamics differ under confinement and affect the bubble collapse violence has not been previously explored. Quantitative understanding of the confinement bubble collapse dynamics is necessary to gaining insights into

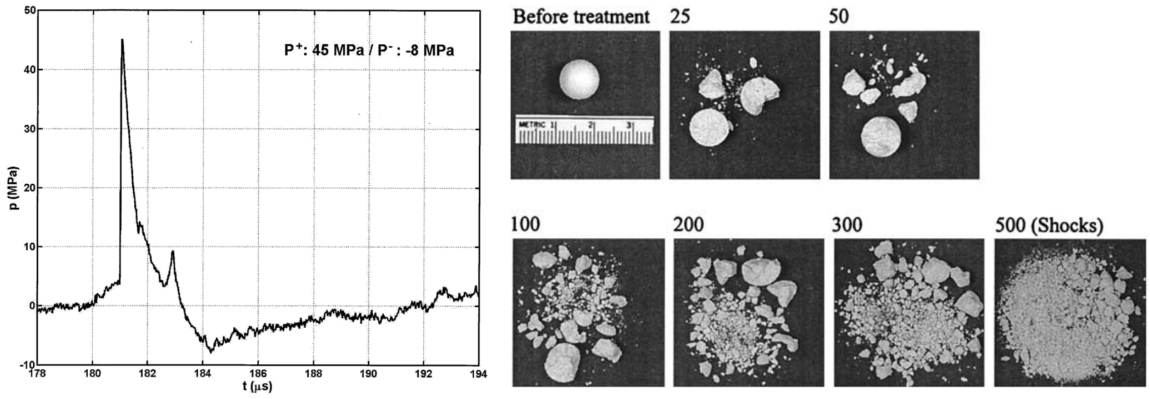

(a) ESWL wave form.

(b) Comminution of stone phantom.

Figure 1.3: Extracorporeal shock wave lithotripsy (ESWL) waveform and photographs of the comminution of a plaster-of-Paris stone phantom from 25-500 ESWL shocks in water (Zhu *et al.*, 2002).

cavitation damage in confined geometries.

1.1.2 Ultrasound-induced cavitation

Extracorporeal shock wave lithotripsy (ESWL) is a non-invasive ultrasound therapy tool used to fractionate kidney stones (Lubock, 1989). The ultrasound is generated extracorporeally and focused to fragment kidney stones to the extent that they can then be passed by the renal system (Coleman *et al.*, 1987; Sass *et al.*, 1991). An ultrasound wave generated by a hydrophone is focused the body, near the kidney stone. A common ESWL waveform consists of a positive pressure peak (a shock) followed by a rarefaction which reaches ~10 MPa in tension (see Fig. 1.3). Peak pressures used in practice are ~40 MPa (Coleman *et al.*, 1987; Zhu *et al.*, 2002). The tensile region generates cavitation bubbles along the kidney stone surface. Two primary stone comminution mechanisms have been proposed based on experimental observation: (i) the tensile stresses generated from the reflected shock within the stone leading to spallation, and (ii) cavitation erosion from the bubbles at the surface leading to material failure (Lubock, 1989; Crum, 1988; Zhong *et al.*, 1993; Brujan, 2004; Weinberg & Ortiz, 2009). Moreover, experiments by Zhu *et al.* (2002) in water and castor oil demonstrated that the combined effect of the tensile stress wave and the cavitation are needed for effective comminution (see Fig. 1.3). However, the interplay between

these two mechanisms and how it leads to more effective kidney stone comminution are not yet well understood.

1.1.3 Naval Hydrodynamics

Cavitation erosion is undesired in the context of naval engineering. Flows in naval engineering involve low-Mach number regions in the liquid, while local Mach numbers can be supersonic in gas/liquid mixture regions where the sound speed can be as low as tens of meters per second (Reisman *et al.*, 1998; Gnanaskandan & Mahesh, 2015; Ganesh *et al.*, 2016). Shocks waves emitted from implosions are one of the important consequences of cavitation and lead to structural damage to neighboring surfaces (Kornfeld & Suvorov, 1944; Benjamin & Ellis, 1966; Tomita & Shima, 1986; Philipp & Lauterborn, 1998; Lindau & Lauterborn, 2003; Franc *et al.*, 2012). The structural damage on these surfaces or objects degrades the performance and need for require or replacement of critical components. The modern description of cavitation erosion to hard, metallic structures is well documented in Kim *et al.* (2014). However, it is unclear whether conclusions made for metallic surfaces apply to softer materials proposed for blast mitigation (Samiee *et al.*, 2013; Rijensky & Rittel, 2016), and other polymer-based materials. Studies have shown that these polymeric materials have a viscoelastic response (Qiao *et al.*, 2011). Understanding the behavior of these compliant, polymeric materials under the high mechanical and thermal loads from cavitation and their influence on the bubble dynamics will provide valuable knowledge towards developing cavitation mitigation strategies.

1.2 Computational Approaches

Due to the wide spatial and temporal scales involved in cavitation damage there are experimental limitations to analyzing cavitation damage in the thematic areas described above. Additionally, the non-intuitive nature of the dynamics and non-linear equations of motion presents an opportunity for numerical simulations to complement analytical and experimental efforts. One challenge lies in

the non-trivial implementation of constitutive models describing the material that include effects such as (nonlinear) elasticity, history and viscosity. We briefly summarize the latest numerical methodologies for computing multi-component flows and bubble dynamics.

1.2.1 Bubble-Cloud and Spherical-Bubble Models

In most applications, cavitation erosion is produced by a cloud of bubbles. While efforts have been made to numerical compute bubble clouds (Zhang & Prosperetti, 1994; Wang & Brennen, 1999; Seo *et al.*, 2010; Fuster & Colonius, 2011; Ando *et al.*, 2013), these approaches are based on models for spherical bubble dynamics. It is well known that non-spherical bubble collapse play an important role in cavitation erosion (Kornfeld & Suvorov, 1944; Knapp, 1955; Benjamin & Ellis, 1966; Tomita & Shima, 1986; Blake & Gibson, 1987; Kim *et al.*, 2014). Moreover, if the neighboring material is soft, accounting for the flow-structure interaction is challenging. As a first step, researchers have considered the dynamics and collapse of a single bubble near a solid. Early models (Fogler & Goddard, 1970; Tanasawa & Yang, 1970) developed to study bubble dynamics in viscoelastic media were based on the Rayleigh-Plesset equation, a nonlinear ordinary differential equation to describe spherical bubble dynamics, with Maxwell constitutive models. Further extensions to include elasticity (Yang & Church, 2005; Hua & Johnsen, 2013; Gaudron *et al.*, 2015) as well as other nonlinearities (Allen & Roy, 2000; Warnez & Johnsen, 2015) have been pursued. However, such approaches, are limited by the assumptions that the dynamics are spherically symmetric and that the near-field flow is incompressible. Neither assumption is strictly valid in problems involving inertia-dominated bubble collapse near a solid object, during which the collapse is often non-spherical and shock waves propagate in the surrounding medium.

1.2.2 Direct Simulations

To gain insights into the asymmetric and compressible nature of bubble collapses, the non-linear governing equations of motion must be solved. Two main numerical methodologies have been pursued: coupling the flow solver to a solid mechanics solver (e.g., arbitrary Lagrangian-Eulerian

or ALE approaches), or computing the fluid and solid mechanics in a single framework.

ALE methodologies have been used for multi-component fluid-structure interaction (FSI) problems such as shock-bubble interaction near a solid object (Young *et al.*, 2009) and for flows with shocks using the Ghost Fluid method (Arienti *et al.*, 2003; Sambasivan & UdayKumar, 2009; Grétarsson & Fedkiw, 2013). The approach has been combined with the incompressible boundary element method (BEM) to capture the bubble implosion and re-entrant jet formation (Hsiao *et al.*, 2014). However, extreme fluid distortions and vorticity generated in problems of interest (e.g., bubble collapsing near an elastically rigid object) can pose challenges to such approaches. Additionally, these approaches increase the algorithmic complexity as they typically involve two solvers—one for the fluid and one for the solid. Furthermore, the coupling generally involves an iterative process to communicate the stresses produced by the fluid to the solid, and the corresponding solid deformations to the fluid (Kalateh & Koosheh, 2018). Another approach within ALE is the extended Finite Element Method (xFEM), which has been used to study implosions and crack growth (Moës & Belytschko, 2002; Šuštarič *et al.*, 2014). These approaches are advantageous in eliminating the need to re-mesh the computational domain. However, these methods are typically limited in considering the fluid to be incompressible (Liu & Marsden, 2018; Wang *et al.*, 2018) or at most weakly compressible. One of the most sophisticated of these approaches is that of Wang *et al.* (2015), which is an embedded boundary method (EBM), utilizing xFEM and the element deletion (ED) method, is used to compute high-speed compressible flows in FSI applications. However, this method is at most second-order accurate and its algorithmic complexity is significant as it combines several numerical approaches. Lagrangian framework using the Finite-Element Method (FEM) have also been considered to solve the compressible Navier-Stokes equations for problems involving discontinuities (e.g., shocks), but are most second-order accurate (Radovitzky & Ortiz, 1999).

On the other hand, Eulerian approaches present a viable alternative to simulate flow-structure interactions. This numerical methodology can naturally handle compressible flows, enforce conservation, and resolve high-frequency contents. High-order accurate shock-capturing schemes

have emerged as viable approaches to simulate bubbles collapsing non-spherically in water and the shock waves thereby produced (Johnsen & Colonius, 2006; Shukla *et al.*, 2010; Tiwari *et al.*, 2013; Coralic & Colonius, 2014).

Two distinct challenges arise in a fully Eulerian, high-order accurate, fluid-solid framework: (i) preventing spurious interfacial errors when simulating resolving multiphase/multi-component flows, and (ii) representing the material deformations and viscoelastic behavior naturally represented in a Lagrangian framework. The representation of interfaces in multiphase flows generally falls under one of two approaches: interface tracking and interface capturing. For the former, these methods are attractive as they can represent sharp interfaces but may suffer conservation losses, which are most crucial in precisely the problems under consideration (shock interacting with an interface). The algorithm typically involves using two solvers, which increases algorithmic complexity. For the latter, interface-capturing approaches regularize the interface over $4-5$ computational cells. This approach is particularly attractive as it naturally enforces conservation and one algorithm computes the flow. However, interface-capturing algorithms bring about their own numerical difficulties, such as the generation of pressure and temperature oscillations across the material discontinuities for interfacial flows (Abgrall, 1996; Shyue, 1998; Johnsen, 2012). Such issues can be addressed for the three-dimensional compressible Navier-Stokes equations for a binary gas-liquid system (Alahyari Beig & Johnsen, 2015).

In the context of cavitation erosion, the chief difficulty in extending such methods to incorporate viscoelasticity lies in the representation of strains (or deformations), which are naturally described in a Lagrangian fashion, in the Eulerian formulation. While Eulerian approaches have historically been limited in modeling the material deformations, two approaches have been pursued (Gavrilyuk *et al.*, 2008): Godunov-based approaches (Godunov & Romenskii, 2003; Gavrilyuk *et al.*, 2008; Favrie *et al.*, 2009; Ndanou *et al.*, 2015) and hypoelastic approaches (Eringen, 1962; Kapahi *et al.*, 2011; Udaykumar *et al.*, 2003; Despres, 2007; Kapahi *et al.*, 2013a; Altmeyer *et al.*, 2015). In the Godunov-based approach, the deformation tensor is directly evolved, such that the equations of motion form a hyperbolic, conservative, and thermodynamically consistent set of

equations (Godunov & Romenskii, 1972; Trangenstein & Colella, 1991; Plohr & Sharp, 1988; Godunov & Romenskii, 2003). Hyperelastic constitutive models, which depend on the deformation tensor, can thus be represented using this approach. However, these approaches are in their infancy towards using high-order accurate methods and are at most second-order accurate.

On the other hand, hypoelastic constitutive models are designed for small strains (Eringen, 1962), the elastic components of the stress tensor obey evolution equations. Both approaches have their advantages and limitations in describing visco(elastic) materials and their implementation in an Eulerian numerical framework is non-trivial. Further discussion on how the hypoelastic approach is particularly attractive when using high-order accurate interface-capturing methods is detailed in Chapter 2.

1.3 Thesis Overview

The objective of this work is to better understand the dynamics of gas bubbles and the emitted shock wave mechanics in elastic and viscoelastic media, by leveraging high-order accurate numerical simulations. Along with the numerical modeling advances, the contributions of this thesis to three areas relevant to cavitation damage are presented below:

Part I: Numerical modeling advances

1. A novel high-order, solution-adaptive Eulerian approach for numerical simulations of wave propagation in viscoelastic media, with application to shocks interacting with interfaces between fluids and viscoelastic media, is developed (Chapter 2). The main challenge lies in representing the combination of viscoelastic, multiphase and compressible flow. A particular difficulty is the calculation of strains in an Eulerian framework, which we address by using a conventional hypoelastic model in which an objective time derivative (Lie derivative) of the constitutive relation is taken to evolve strain rates instead. The numerical method is verified in a comprehensive fashion using a series of smooth and discontinuous (shocks and interfaces), one- and two-dimensional test problems.

2. We extend our approach to all-speed flows, including viscoelasticity, using the Advection Upstream Splitting Method (AUSM) (Chapter 3). We generalize the AUSM flux-vector splitting (FVS) to account for the Cauchy stress tensor. An additional novelty is the extension of the AUSM scheme to the five-equation model for simulations of interfaces between gases, liquids, and solids. We determine an appropriate discretization of non-conservative equations that appear in the five-equation multiphase model with AUSM schemes to prevent spurious oscillations at material interfaces. The framework is used to simulate 1D and 2D problems that demonstrate the ability to maintain equilibrium interfacial conditions and solve challenging multi-dimensional and multi-material problems.

Part II: Bubble dynamics investigations

4. We leverage our numerical approach to conduct a series of investigations on the dynamics of bubbles inertially collapsing in a channel (Chapter 3). The quantities of interest are the maximum pressures along the perfectly rigid channels walls, bubble collapse distance migration and minimum bubble volume. We qualitatively study the wave dynamics of the collapse and gain novel insights into the mechanisms of asymmetric collapse and multiple re-entrant jet formation. Moreover, we determine the smallest channel width, relative to the initial bubble radius, for which the presence of a second wall has a non-negligible effect on the collapse dynamics.

5. We conduct a fundamental study to examine the effectiveness of the ESWL ultrasound shock wave in the presence of a cavitation (Chapter 5). We consider a shock-induced bubble collapse adjacent to a model kidney stone. We examine the effect of different model kidney stone sizes and initial bubble stand-off distances on the maximum principal stress in the stone. An augmentation of the potential for material failure when the cavitation bubble is present is achieved relative to the case without the bubble. Three distinct events at which the tensile stress in the model kidney stone in the presence of the bubble exhibits a local maximum are identified.

6. Relevant to naval engineering applications, we conduct a study to determine the cavitation damage and material failure mechanisms in shock-induced bubble collapse near a polymeric coating (Chapter 6). Single and multiple bubble collapse problems are presented for various configurations. This study considers the nearby object to be compliant such that the deformations are infinitesimally small. We quantify the maximum pressures in the polymeric layer from the bubble collapse. The polymeric coating's deformation is also investigated, particularly after the bubble collapse when a convecting vortex ring is generated, which can further deform the material. These results are of importance because the object's viscoelasticity can dampen the wave propagation and bubble interaction hypothesized to deform and damage nearby objects.

Part I:

Numerical Approaches for Multi-component, Compressible Flows with Linear Viscoelasticity

CHAPTER 2

A high-order accurate, five-equations compressible multiphase approach for viscoelastic fluids and solids with relaxation and elasticity

This chapter is adapted from Rodriguez & Johnsen (2018).

2.1 Abstract

A novel Eulerian approach is proposed for numerical simulations of wave propagation in viscoelastic media, for application to shocks interacting with interfaces between fluids and viscoelastic media. In this chapter, we extend the five-equations multiphase, interface-capturing model, based on the idea that all the materials (gases, liquids, solids) obey the same equation of state with spatially varying properties, to incorporate the desired constitutive relation; in this context, interfaces are represented by discontinuities in material properties. We consider problems in which the deformations are small, such that the substances can be described by linear constitutive relations, specifically, Maxwell, Kelvin-Voigt or generalized Zener models. The main challenge lies in representing the combination of viscoelastic, multiphase and compressible flow. One particular difficulty is the calculation of strains in an Eulerian framework, which we address by using a conventional hypoelastic model in which an objective time derivative (Lie derivative) of the constitutive relation is taken to evolve strain rates instead. The resulting eigensystem is analyzed to identify approach

wave speeds and characteristic variables. The spatial scheme is based on a solution-adaptive formulation, in which a discontinuity sensor discriminates between smooth and discontinuous regions. To compute the convective fluxes, explicit high-order central differences are applied in smooth regions, while a high-order finite-difference Weighted Essentially Non-Oscillatory scheme is used at discontinuities (shocks, material interfaces and contacts). The numerical method is verified in a comprehensive fashion using a series of smooth and discontinuous (shocks and interfaces), one- and two-dimensional test problems.

2.2 Introduction

Recent years have seen the emergence of the need for simulating shock and other high-frequency-content waves (e.g., blasts, therapeutic ultrasound pulses, shocks emitted by collapsing bubbles) interacting with solid objects whose stiffnesses can range from soft (e.g., human tissue) (Vlaisavljevich *et al.*, 2015) to moderate (e.g., elastomeric coatings in naval propulsors) (Rijensky & Rittel, 2016; Bahei-El-Din *et al.*, 2006) to hard (metals or concrete) (de Brauer *et al.*, 2016; Ndanou *et al.*, 2015; López Ortega *et al.*, 2011). An example of interest is the impingement of a shock propagating in a liquid upon a solid object and its subsequent propagation in the solid, which presents the computational challenge of accurately and robustly representing compressible, multi-material flows with shocks, shear waves, and viscoelastic deformations of the solid. High-order accurate shock- and interface-capturing schemes have emerged as viable approaches for shocks in multi-material flows, for instance, to simulate gas bubbles collapsing in water near solid objects and the shock waves thereby produced (Johnsen & Colonius, 2006; Shukla *et al.*, 2010; Tiwari *et al.*, 2013; Coralic & Colonius, 2014). Given their high order of accuracy, these approaches accurately represent high-frequency-content waves emitted by bubble collapse. However, an accurate description of the solid mechanics is challenging. Two main strategies have been pursued: coupling the flow solver with a solid mechanics solver (e.g., arbitrary Lagrangian-Eulerian or ALE approaches), or solving the fluid and solid mechanics in a single framework. The former has been used for multi-

component fluid-structure interaction problems such as shock-bubble interaction near a solid object (Young *et al.*, 2009) and for flows with shocks using the Ghost Fluid method (Arienti *et al.*, 2003; Sambasivan & UdayKumar, 2009; Grétarsson & Fedkiw, 2013). However, the extreme fluid distortions and vorticity generated in problems of interest (e.g., bubble collapsing near an elastically rigid object) can pose challenges to such approaches. Additionally, these approaches increase in algorithmic complexity as they typically involve two solvers—one for the fluid and one for the solid—whose complexity increases even more so when incorporating viscoelasticity. Additionally, the Lagrangian portion of the numerical approach of the solver is typically limited in its ability to capture high-frequency contents of relevant waves relative to the Eulerian counterpart. Thus, our present focus resides in the latter—a single framework for fluids and solids, which can represent fully coupled fluid-solid mechanics. Given our interest in leveraging the advantages of high-order shock- and interface-capturing approaches, the chief difficulty lies in representing strains (or deformations), naturally described in a Lagrangian fashion, in the Eulerian formulation of predilection for discontinuity capturing. This difficulty has been addressed primarily by following either Godunov-based or "conventional" approaches (Gavrilyuk *et al.*, 2008).

In the Godunov-based approach, the deformation tensor is directly evolved, such that the equations of motion form a hyperbolic, conservative, and thermodynamically consistent set of equations (Godunov & Romenskii, 1972; Trangenstein & Colella, 1991; Plohr & Sharp, 1988; Godunov & Romenskii, 2003). Hyperelastic constitutive models, which depend on the deformation tensor, can thus be represented using this approach. Computational studies of shocks in a single elastic medium were performed with second-order shock-capturing schemes (Le Floch & Olsson, 1990; Miller & Colella, 2001, 2002; Miller, 2004; Gavrilyuk *et al.*, 2008). High-order Weighted Essentially Non-Oscillatory (WENO) (Jiang & Shu, 1996), Arbitrary DERivative in space and time (ADER) (Titarev & Toro, 2002) and Discontinuous Galerkin approaches have been implemented for single-phase problems involving fluids and solids (Dumbser *et al.*, 2015). These methods can represent interfaces via interface tracking and capturing, as well as immersed boundary methods (Barton & Drikakis, 2010; Barton *et al.*, 2011, 2013; Schoch *et al.*, 2013; López Ortega *et al.*,

2011, 2014; Gorsse *et al.*, 2014). However, these interface-tracking techniques may suffer conservation losses. Although interface capturing, e.g., using the seven- or five-equations multiphase models (Baer & Nunziato, 1986; Kapila *et al.*, 2001; Saurel & Abgrall, 1999a; Saurel & Lemetayer, 2001), has been used for ballistic and detonation problems (Favrie *et al.*, 2009; Favrie & Gavriliyuk, 2011; Ndanou *et al.*, 2013, 2015) with second-order accurate schemes, the implementation of Riemann solvers appropriately capturing all the waves of the nonlinear hyperbolic systems for arbitrary constitutive models is challenging. Moreover, it is not clear how to incorporate stress relaxation in such a formulation.

For these reasons, we consider conventional approaches, in which an objective temporal derivative of the constitutive relation is performed to obtain an evolution equation for the stress tensor. This process effectively transforms strains into strain rates, which can naturally be represented in an Eulerian formulation in terms of the velocity gradient (Kulikovskii *et al.*, 2002; Despres, 2007). Moreover, this process is suited to hypoelastic constitutive models for small strains (Eringen, 1962) in which the elastic components of the stress tensor obey evolution equations. Appropriate objective derivatives must be used, e.g., Lie derivative (Altmeyer *et al.*, 2015); if not, thermodynamically inconsistent equations and results may be obtained (Trangenstein & Colella, 1991; Morro, 2017). The resulting system of equations is attractive given the relatively straightforward numerical implementation of viscoelasticity, including generalized Zener models (Robertsson *et al.*, 1994). This conventional approach has been used in the geophysical community to simulate nonlinear wave propagation in viscoelastic media (Carcione, 1993). For multi-material problems, the ADER scheme was implemented to investigate wave propagation in incompressible viscoelastic media using an immersed interface method, with a specific focus on stress relaxation (Lombard & Piraux, 2011). The Sharp-Interface approach, a mixed Eulerian-Lagrangian method (Udaykumar *et al.*, 2003), and the particle level-set method (Tran & Udaykumar, 2004) have been used to study high-speed solid impact, penetration and void collapse problems (Tran & Udaykumar, 2006a,b). The Ghost Fluid method has also been employed to simulate elastic-plastic deformations (Kapahi *et al.*, 2013b,a; Kapahi & Udaykumar, 2015, 2013). However, interface capturing (e.g., five-equations

model) has yet to be used in conjunction with this conventional approach. Interface capturing can be designed to be fully conservative, by contrast to the tracking methods described above. However, one of the expected challenges when using interface capturing in conjunction with this conventional approach, which we address, lies in maintaining the appropriate interfacial conditions and preventing spurious pressure and temperature errors (Abgrall, 1996; Saurel & Abgrall, 1999b; Johnsen, 2011; Alahyari Beig & Johnsen, 2015).

Our goal is to develop a numerical method capable of accurately representing wave propagation (including shocks and other high-frequency-content waves) in heterogeneous and compressible viscoelastic media with interfaces and heat diffusion processes. Given our interest in problems in which solid deformations are sufficiently small and exhibit elastic, viscous and memory effects (stress relaxation), the key contribution in this article is to extend the five-equations interface-capturing method for compressible multiphase flows to the generalized Zener linear viscoelastic model (i.e., with elasticity and relaxation) based on the Lie derivative. In this fully coupled fluid-solid approach, all materials (gases, liquids, solids) obey the same equation of state and constitutive model with spatially varying properties. Such an approach is attractive since the same numerical scheme can be applied throughout the computational domain; furthermore, we can leverage high-order accurate discontinuity-capturing schemes commonly used in Eulerian calculations. The article is organized as follows. We first present our physical model, with an emphasis on the constitutive relations. We then describe our numerical model and analyze the properties of the system of equations. Next, the numerical method is discussed. A stringent suite of one- and two-dimensional, single- and multi-phase test problems with various viscoelastic models, shocks and interfaces, is presented for verification purposes.

2.3 Physical Model

2.3.1 Equations of Motion

The equations governing the phenomena of interest are the mass conservation, momentum balance and energy balance equations:

$$\frac{\partial \rho}{\partial t} + \frac{\partial}{\partial x_j}(\rho u_j) = 0, \tag{2.1a}$$

$$\frac{\partial}{\partial t}(\rho u_i) + \frac{\partial}{\partial x_j}(\rho u_i u_j - \sigma_{ij}) = 0, \tag{2.1b}$$

$$\frac{\partial E}{\partial t} + \frac{\partial}{\partial x_j}(E u_j - \sigma_{ij} u_i) = -\frac{\partial Q_k}{\partial x_k}, \tag{2.1c}$$

$$\frac{\partial}{\partial t}(\rho^{(k)} \alpha^{(k)}) + \frac{\partial}{\partial x_j}(\rho^{(k)} \alpha^{(k)} u_j) = 0, \qquad k = 1, ..., K-1, \tag{2.1d}$$

where ρ is the total density, u_i the velocity vector, σ_{ij} the Cauchy stress tensor, Q_k the heat flux, $\alpha^{(k)}$ the volume fraction of material k, K the total number of materials, and indices $i, j = 1, 2$, and 3. Repeated indices imply summation. Eqs. (4.6a) are mass conservation equations for $K - 1$ materials. The total energy (per unit volume) E comprises internal, kinetic and elastic contributions:

$$E = \rho e + \frac{1}{2}\rho u_i^2 + \rho e^{(e)}. \tag{2.2}$$

The internal energy (per unit volume) ρe is related to the relevant thermodynamic quantities through the equation of state described in the next section, and the elastic energy $\rho e^{(e)}$ is described in more detail in §3.3.3. Material k has volume fraction $\alpha^{(k)}$ and density $\rho^{(k)}$, with

$$\sum_k \rho^{(k)} \alpha^{(k)} = \rho, \qquad \sum_k \alpha^{(k)} = 1. \tag{2.3}$$

As described in §3.4.2, $K - 1$ mass balance equations, corresponding to the K materials, must be evolved.

2.3.2 Equation of State

The Noble-Abel Stiffened-Gas equation of state (Le Métayer & Saurel, 2016) is used to relate the internal energy to pressure and temperature in all materials:

$$\rho e = \frac{p(1-\rho b)}{n-1} + \frac{nB(1-\rho b)}{n-1} + \rho q \tag{2.4a}$$

$$= \rho c T + B(1-\rho b) + \rho q, \tag{2.4b}$$

where T is the temperature and q, n, B, b and c are material properties prescribed to produce the correct propagation speeds in liquids and solids (Harlow & Amsden, 1971; Le Métayer *et al.*, 2005; Le Métayer & Saurel, 2016). This equation reduces to the stiffened gas equation of state (Le Métayer *et al.*, 2005) with $b = 0$ and by setting the other properties to appropriate values. In the limit of ideal gases, $B = 0$, $b = 0$, $q = 0$, c is the specific heat at constant volume and $n = \gamma$ is the ratio of specific heats. Table 6.1 lists the values of the material properties corresponding to materials of interest. The model viscoelastic medium has properties very similar to those of water, with a slightly greater acoustic impedance. The calculation of ρe when multiple materials are present is discussed in §3.4.2.

Table 2.1: Material properties corresponding to different media described by the Noble-Abel Stiffened-Gas equation of state.

Material	n	b[m^3/kg$\times 10^{-4}$]	B[Pa$\times 10^6$]	q [kJ/kg]	c [kJ/kg·K]
Air	1.40	0	0	0	0.718
Water & viscoelastic medium	1.19	6.61	702.8	-1.167	4.167

2.3.3 Constitutive Relations

Closure relationships for the heat flux and Cauchy stress tensor are required to close the system of equations. Fourier conduction describes the heat diffusion process:

$$Q_k = -\kappa \frac{\partial T}{\partial x_k}, \tag{2.5}$$

where κ is the thermal conductivity.

Before discussing the stresses, we define the strain-rate tensor and its deviatoric part,

$$\dot{\epsilon}_{ij} = \frac{1}{2}\left(\frac{\partial u_i}{\partial x_j} + \frac{\partial u_j}{\partial x_i}\right), \qquad \dot{\epsilon}^{(d)}_{ij} = \dot{\epsilon}_{ij} - \frac{1}{3}\dot{\epsilon}_{kk}\delta_{ij}, \tag{2.6}$$

where the dot denotes an objective temporal derivative, here the Lie derivative. The Cauchy stress tensor can be written in terms of isotropic and deviatoric contributions,

$$\sigma_{ij} = \sigma^{(i)}_{ij} + \tau^{(d)}_{ij}. \tag{2.7}$$

The isotropic term consists of mechanical pressure and bulk (dilatational) viscous contributions:

$$\sigma^{(i)}_{ij} = -p\delta_{ij} + \mu_b \dot{\epsilon}_{kk}\delta_{ij}, \tag{2.8}$$

where μ_b is the bulk viscosity. The isotropic elastic contributions to the Cauchy stress tensor, which are associated with density changes in the material, are captured via the mechanical pressure, which itself is determined through the equation of state.

The deviatoric stress can further be written in terms of viscous, $\tau^{(v)}_{ij}$, and elastic, $\tau^{(e)}_{ij}$, contributions,

$$\tau^{(d)}_{ij} = \tau^{(v)}_{ij} + \tau^{(e)}_{ij}, \tag{2.9}$$

where $\tau^{(v)}_{ij} = 2\mu_s \dot{\epsilon}^{(d)}_{ij}$. The elastic stress is modeled as a hypoelastic material where the stress tensor

rate linearly depends on the spatial velocity gradient (Eringen, 1962),

$$\dot{\tau}_{ij}^{(e)} = \mathcal{D}_{ijkl}\frac{\partial u_k}{\partial x_l}, \tag{2.10}$$

where $\mathcal{D}_{ijkl}$ is a rank-4 tensor with the objective stress tensor rate terms. Since we consider isotropic media, $\tau_{ij}^{(e)} = 2G\epsilon_{ij}^{(d)}$. Our focus lies in materials that may exhibit stress relaxation, elasticity and viscosity, and undergo infinitesimally small deformations (i.e., linear viscoelasticity in which the stress and its rate depend linearly on the strain and its rate). The simplest constitutive model accounting for these effects is the Zener model (Zener, 1947), used to represent, among other things, biomaterials (Fung, 1993):

$$\lambda_r\dot{\tau}_{ij}^{(d)} + \tau_{ij}^{(d)} = 2\mu_s\dot{\epsilon}_{ij}^{(d)} + 2G\epsilon_{ij}^{(d)}, \tag{2.11}$$

where λ_r is the relaxation time, μ_s the shear viscosity, G the shear modulus. The elastic energy is then defined as

$$\rho e^{(e)} = \frac{\tau_{ij}^{(e)}\tau_{ij}^{(e)}}{4G}. \tag{2.12}$$

The Zener model has the advantage of reducing to other simple linear constitutive relations (Carcione, 2014; Fung, 1993; Wineman, 2000). For $\lambda_r = 0$, the model reduces to that representing a Kelvin-Voigt solid,

$$\tau_{ij}^{(d)} = 2\mu_s\dot{\epsilon}_{ij}^{(d)} + 2G\epsilon_{ij}^{(d)}. \tag{2.13}$$

If $\mu_s = 0$ and $\lambda_r = 0$, the model further reduces to that representing a linear Hookean solid,

$$\tau_{ij}^{(d)} = 2G\epsilon_{ij}^{(d)}. \tag{2.14}$$

In Eq. (3.8), the model represents a Maxwell fluid if $G = 0$,

$$\lambda_r\dot{\tau}_{ij}^{(d)} + \tau_{ij}^{(d)} = 2\mu_s\dot{\epsilon}_{ij}^{(d)}. \tag{2.15}$$

Additionally, if $\lambda_r = 0$, the model further reduces to that representing a viscous, Newtonian fluid,

$$\tau_{ij}^{(d)} = 2\mu_s \dot{\epsilon}_{ij}^{(d)}. \tag{2.16}$$

The Zener model can further be generalized to account for materials exhibiting frequency-dependent viscoelastic properties, e.g., soft tissue (Klatt *et al.*, 2007; Palacio-Torralba *et al.*, 2015). The shear relaxation function is defined as (Carcione, 2014),

$$\psi = G_r \left(1 + \sum_{l=1}^{N_r} \varsigma^{(l)} \exp(-\theta^{(l)} t) \right) H(t), \tag{2.17}$$

where G_r is the relaxed shear modulus, $\varsigma^{(l)}$ the strictly positive relaxation shear coefficient corresponding to relaxation frequency $\theta^{(l)}$, N_r the total number of frequencies and $H(t)$ the Heaviside function. The elastic stress can be written as a time convolution of the shear relaxation function and (deviatoric) strain rate,

$$\tau_{ij}^{(d)} = 2\psi(t) * \epsilon_{ij}^{(d)}. \tag{2.18}$$

2.4 Numerical Model

2.4.1 Numerical Implementation of Viscoelastic Models

2.4.1.1 Kelvin-Voigt

We first consider the Kelvin-Voigt model, perhaps the simplest viscoelastic model in which an elastic contribution is simply added to the viscous stress to form the total deviatoric stress. Drawing from (Kulikovskii *et al.*, 2002; Altmeyer *et al.*, 2015, 2016), the Lie objective temporal derivative of the elastic stress is taken to transform strains into strain rates,

$$\dot{\tau}_{ij}^{(e)} = \frac{\partial \tau_{ij}^{(e)}}{\partial t} + u_k \frac{\partial \tau_{ij}^{(e)}}{\partial x_k} - \tau_{kj}^{(e)} \frac{\partial u_i}{\partial x_k} - \tau_{ik}^{(e)} \frac{\partial u_j}{\partial x_k} + \tau_{ij}^{(e)} \frac{\partial u_k}{\partial x_k}, \tag{2.19}$$

where the first two terms are the material derivative of the stress tensor and the rest of the terms contribute to preserving objectivity. The material derivative is incorporated in the Lie derivative to transport elastic stress tensor discontinuities. We note that the Lie derivative is equivalent to the Truesdell derivative (Altmeyer *et al.*, 2015) in a rectangular Cartesian coordinate system. We follow the restrictions for the thermodynamic consistency of the Truesdell derivative (Morro, 2017). The Oldroyd derivative is obtained if the last term in Eq. (3.12), which accounts for the compressible effects, is set to zero. These stress rates, among others, and their behavior under small and finite deformations have been characterized in the literature (Surana *et al.*, 2010).

Another useful property of the Lie derivative is that its acoustic tensor is symmetric. The acoustic tensor is defined as,

$$\mathcal{A}_{jk} = \frac{1}{\rho} n_i \left(\mathcal{B}_{ijkl} + C_{ijkl} \right) n_l, \tag{2.20}$$

where n_i is an arbitrary unit vector, $\mathcal{B}_{ijkl}$ the tensor of objective stress rates, and C_{ijkl} the stiffness tensor,

$$\dot{\tau}_{ij}^{(e)} = C_{ijkl} \frac{\partial u_k}{\partial x_l} = 2G \left(\mathcal{I}_{ijkl} - \frac{1}{3} \delta_{ij} \delta_{kl} \right) \frac{\partial u_k}{\partial x_l} = 2G \dot{\epsilon}_{ij}^{(d)}, \tag{2.21}$$

where $\mathcal{I}_{ijkl}$ is the rank-4 identity tensor and the final equality holds for an isotropic medium. The acoustic tensor for the Lie derivative can thus be written,

$$\mathcal{A}_{jk} = \frac{1}{\rho} n_i \left(\mathcal{B}_{ijkl} + C_{ijkl} \right) n_l = \frac{1}{\rho} \left[n_i \tau_{il}^{(e)} n_l \delta_{jk} + G \left(\delta_{jk} + \frac{n_j n_k}{3} \right) \right], \tag{2.22}$$

which is symmetric, by contrast to the Jaumann derivative (Trangenstein & Colella, 1991).

Combining mass conservation and Eqs. (3.12) and (2.21), the evolution equation using the Lie derivative for the elastic stress tensor becomes,

$$\frac{\partial}{\partial t} (\rho \tau_{ij}^{(e)}) + \frac{\partial}{\partial x_k} (\rho \tau_{ij}^{(e)} u_k) = \rho \left(\tau_{kj}^{(e)} \frac{\partial u_i}{\partial x_k} + \tau_{ik}^{(e)} \frac{\partial u_j}{\partial x_k} - \tau_{ij}^{(e)} \frac{\partial u_k}{\partial x_k} + 2G \dot{\epsilon}_{ij}^{(d)} \right). \tag{2.23}$$

In two dimensions, three equations must be solved for the elastic contribution of the stress, namely for $\tau_{11}^{(e)}$, $\tau_{22}^{(e)}$ and $\tau_{12}^{(e)}$ (or $\tau_{21}^{(e)}$, since the Cauchy stress tensor is symmetric). In the absence of elastic

effects (i.e., $G = 0$), the compressible Navier-Stokes equations are recovered. In the absence of viscous effects (i.e., $\mu_s = \mu_b = 0$), the Euler equations with elastic stresses are recovered (Kulikovskii *et al.*, 2002; Gavrilyuk *et al.*, 2008; Kapahi *et al.*, 2013a; Kapahi & Udaykumar, 2015). Eq. (2.23) complements the mass, momentum and energy Eqs. (4.1). The momentum and energy equations are solved as follows:

$$\frac{\partial}{\partial t}(\rho u_i) + \frac{\partial}{\partial x_j}(\rho u_i u_j + p\delta_{ij} - \tau_{ij}^{(e)}) = \frac{\partial}{\partial x_j}\left(\tau_{ij}^{(v)} + \mu_b \dot{\epsilon}_{kk}\delta_{ij}\right), \tag{2.24a}$$

$$\frac{\partial E}{\partial t} + \frac{\partial}{\partial x_j}[(E+p)u_j - \tau_{ij}^{(e)}u_i] = \frac{\partial}{\partial x_j}\left[u_i\left(\tau_{ij}^{(v)} + \mu_b \dot{\epsilon}_{kk}\delta_{ij}\right)\right] + \frac{\partial}{\partial x_j}\left(\kappa\frac{\partial T}{\partial x_j}\right). \tag{2.24b}$$

The model equations for Kelvin-Voigt using the Lie derivative implementation for stress evolution are Eqs. (4.1a), (4.6a), (2.23) and (3.16).

2.4.1.2 Zener and Generalized Zener Model

For the Zener and generalized Zener models, we extend the differential viscoelastic model in Robertsson *et al.* (1994); Bécache *et al.* (2005); Lombard & Piraux (2011) to incorporate the constitutive model, Eq. (3.11). We follow the thermodynamic restrictions for the Zener model (Ván *et al.*, 2014). Following the same procedure as that described in the previous section, a Lie derivative of the constitutive relation is taken to transform the strains into strain rates, thus yielding the following equations for the stress and memory variables:

$$\frac{\partial}{\partial t}\left(\rho\tau_{ij}^{(e)}\right) + \frac{\partial}{\partial x_j}(\rho\tau_{ij}^{(e)}u_j) = \rho\left[\tau_{kj}^{(e)}\frac{\partial u_i}{\partial x_k} + \tau_{ik}^{(e)}\frac{\partial u_j}{\partial x_k} - \tau_{ij}^{(e)}\frac{\partial u_k}{\partial x_k} + 2G\dot{\epsilon}_{ij}^{(d)} + \sum_{l}^{N_r}\xi_{ij}^{(l)}\right], \tag{2.25a}$$

$$\frac{\partial}{\partial t}(\rho\xi_{ij}^{(l)}) + \frac{\partial}{\partial x_j}(\rho\xi_{ij}^{(l)}u_j) = \rho\left[\xi_{kj}^{(l)}\frac{\partial u_i}{\partial x_k} + \xi_{ik}^{(l)}\frac{\partial u_j}{\partial x_k} - \xi_{ij}^{(l)}\frac{\partial u_k}{\partial x_k} - \theta^{(l)}\left(2\varsigma^{(l)}G_r\dot{\epsilon}_{ij}^{(d)} + \xi_{ij}^{(l)}\right)\right], \quad l = 1, ..., N_r, \tag{2.25b}$$

where $\xi_{ij}^{(l)}$ is the lth memory variable,

$$\xi_{ij}^{(l)} = -\theta^{(l)}G_r\varsigma^{(l)}\exp(-\theta^{(l)}t)H(t) \star \dot{\epsilon}_{ij}^{(d)}, \tag{2.26}$$

G_r is the relaxed shear modulus,

$$G = G_r \left(1 + \sum_{l=1}^{N_r} \varsigma^{(l)} \right), \tag{2.27}$$

and $\varsigma^{(l)}$ are the strictly positive relaxation coefficients for the given material which can be obtained by material characterization (Lombard & Piraux, 2011). Using the mechanical analog of the generalized Zener model (Carcione, 2014), the relaxation coefficients can be evaluated using material properties,

$$\varsigma^{(l)} = \lambda_\epsilon^{(l)} \theta^{(l)} - 1, \tag{2.28}$$

where $\lambda_\epsilon^{(l)}$ are the retardation times, or creep times. There are N_r relaxation frequencies corresponding to N_r memory variables and evolution equations. The additional evolution equations close the system without having to perform a convolution in time, i.e., Eq. (3.14) need not be solved. The model equations for the generalized Zener model using the Lie derivative implementation for stress transport are Eqs. (4.1a), (4.6a), (3.16), and (3.13). These equations close the momentum and energy balance equations, Eqs. (3.16). We note that Eq. (3.13) incorporates the shear viscous contributions and that both the retardation and relaxation times are functions of the shear viscosity. Thus, the $\tau_{ij}^{(v)}$ term solved in the conservation of linear momentum and energy equations, i.e., Eqs. (3.16), should not be included when solving for the Zener, generalized Zener, and Maxwell models. However, the bulk viscosity contributions in Eq. (2.8) must be retained in this formulation. If there is only one relaxation time (i.e., $N_r = 1$), we recover the Zener model. For a single relaxation frequency, the Maxwell model is recovered by setting $G = G_r = \mu_s \theta^{(1)}$. In the absence of elasticity and relaxation, the model reverts to the Newtonian model in Eqs. (3.16), in which case Eqs. (3.13) need not be solved, $\tau_{ij}^{(e)}$ terms are neglected, and $\tau_{ij}^{(v)}$ must be included in Eqs. (3.16).

2.4.1.3 Eigensystem of the Euler equations with hypoelastic stresses using the Lie derivative

The eigensystem of the Euler equations are well known. For a hypoelastic medium with a Lie derivative implementation, additional terms are present. Here, we determine how elasticity and the

additional terms introduced by the Lie derivative affect the eigensystem. We neglect viscous and thermal effects, and consider the one-dimensional equations for a single material,

$$
\begin{aligned}
&\frac{\partial \rho}{\partial t} + \frac{\partial}{\partial x}(\rho u) = 0, \\
&\frac{\partial}{\partial t}(\rho u) + \frac{\partial}{\partial x}(\rho u^2 + p - \tau_{11}^{(e)}) = 0, \\
&\frac{\partial}{\partial t}(\rho v) + \frac{\partial}{\partial x}(\rho v u - \tau_{12}^{(e)}) = 0, \\
&\frac{\partial E}{\partial t} + \frac{\partial}{\partial x}\left[u(E + p - \tau_{11}^{(e)}) - v\tau_{12}^{(e)}\right] = 0, \\
&\frac{\partial}{\partial t}(\rho \tau_{11}^{(e)}) + \frac{\partial}{\partial x}(\rho u \tau_{11}^{(e)}) = \rho\left(\frac{4G}{3} + \tau_{11}^{(e)}\right)\frac{\partial u}{\partial x}, \\
&\frac{\partial}{\partial t}(\rho \tau_{22}^{(e)}) + \frac{\partial}{\partial x}(\rho u \tau_{22}^{(e)}) = \rho\left(-\frac{2G}{3} - \tau_{22}^{(e)}\right)\frac{\partial u}{\partial x} + 2\rho\tau_{12}^{(e)}\frac{\partial v}{\partial x}, \\
&\frac{\partial}{\partial t}(\rho \tau_{12}^{(e)}) + \frac{\partial}{\partial x}(\rho u \tau_{12}^{(e)}) = \rho\left(G + \tau_{11}^{(e)}\right)\frac{\partial v}{\partial x},
\end{aligned}
\tag{2.29}
$$

which can be written in quasi-linear form,

$$
\frac{\partial W}{\partial t} + A(W)\frac{\partial W}{\partial x} = 0, \tag{2.30}
$$

where W is the vector of primitive variables and A is the Jacobian matrix,

$$
W = \begin{bmatrix} \rho \\ u \\ v \\ p \\ \tau_{11}^{(e)} \\ \tau_{22}^{(e)} \\ \tau_{12}^{(e)} \end{bmatrix}, \qquad A(W) = \begin{bmatrix} u & \rho & 0 & 0 & 0 & 0 & 0 \\ 0 & u & 0 & \frac{1}{\rho} & -\frac{1}{\rho} & 0 & 0 \\ 0 & 0 & u & 0 & 0 & 0 & -\frac{1}{\rho} \\ 0 & \rho a^2 & 0 & u & 0 & 0 & 0 \\ 0 & -\frac{4G}{3} - \tau_{11}^{(e)} & 0 & 0 & u & 0 & 0 \\ 0 & \frac{2G}{3} + \tau_{22}^{(e)} & -2\tau_{12}^{(e)} & 0 & 0 & u & 0 \\ 0 & 0 & -G - \tau_{11}^{(e)} & 0 & 0 & 0 & u \end{bmatrix}, \tag{2.31}
$$

where $a = \sqrt{\frac{n(p+B)}{\rho(1-\rho b)}}$ is the speed of sound corresponding to the Noble-Abel Stiffened-Gas equation of state. The eigenvalues (i.e., wave speeds) of the Jacobian matrix are:

$$\zeta_{1,2,3} = u, \quad \zeta_{4,5} = u \pm \sqrt{\frac{G + \tau_{11}^{(e)}}{\rho}}, \quad \zeta_{6,7} = u \pm \sqrt{a^2 + \frac{4G/3 + \tau_{11}^{(e)}}{\rho}}. \tag{2.32}$$

For the analysis in the y-direction, u and $\tau_{11}^{(e)}$ in the eigenvalues in Eq. (2.32) are replaced with v and $\tau_{22}^{(e)}$, respectively. As expected, the presence of elasticity manifests in the characteristic wave speeds by two important modifications: it introduces three additional waves (a linearly degenerate wave ζ_5 and two shear waves $\zeta_{4,5}$) and it increases the propagation speed of the (longitudinal) pressure waves. If the analysis is extended to the Zener model, there are three additional linearly degenerate waves; for the generalized Zener model, each additional relaxation frequency introduces three additional such waves. When considering multi-material problems, each additional material introduces a linearly degenerate wave. In the absence of elasticity, the speed of sound reduces to that expected for a fluid obeying the Noble-Abel Stiffened-Gas equation of state.

The corresponding right eigenvector matrix of the Jacobian matrix,

$$R = \begin{bmatrix} 0 & 0 & 1 & 0 & 0 & \rho & \rho \\ 0 & 0 & 0 & 0 & 0 & \sqrt{a^2 + \frac{4G/3+\tau_{11}^{(e)}}{\rho}} & -\sqrt{a^2 + \frac{4G/3+\tau_{11}^{(e)}}{\rho}} \\ 0 & 0 & 0 & -\sqrt{\frac{G+\tau_{11}^{(e)}}{\rho}} & \sqrt{\frac{G+\tau_{11}^{(e)}}{\rho}} & 0 & 0 \\ 0 & 1 & 0 & 0 & 0 & \rho a^2 & \rho a^2 \\ 0 & 1 & 0 & 0 & 0 & -(4G/3 + \tau_{11}^{(e)}) & -(4G/3 + \tau_{11}^{(e)}) \\ 1 & 0 & 0 & 2\tau_{12}^{(e)} & 2\tau_{12}^{(e)} & 2G/3 + \tau_{22}^{(e)} & 2G/3 + \tau_{22}^{(e)} \\ 0 & 0 & 0 & G + \tau_{11}^{(e)} & G + \tau_{11}^{(e)} & 0 & 0 \end{bmatrix}, \tag{2.33}$$

where the j-th column corresponds to the j-th wave speed ζ_j. We recognize the three linearly degenerate waves in the first three columns, with the first and third corresponding to the $\tau_{22}^{(e)}$ and density jump across the contact, respectively, and the second to $\sigma_{11} = (-p + \tau_{11}^{(e)})$, which is contin-

uous across the contact. Then come the s-waves (shear) in the fourth and fifth columns, followed by the p-waves (pressure) in the sixth and seventh columns. We further note that the i-th primitive variable is discontinuous across the j-th wave if the entry in the i-th row and j-th column is non-zero. This observation is particularly important for the shear waves, where this analysis indicates that v, $\tau_{22}^{(e)}$ and $\tau_{12}^{(e)}$ are discontinuous when using the Lie derivative.

2.4.2 Multi-Material Framework

We extend the five-equations compressible multiphase model (Allaire *et al.*, 2002; Murrone & Guillard, 2005; Alahyari Beig & Johnsen, 2015) used to capture gas/liquid material interfaces to solids. In this framework, all the materials (gases, liquids, solids) obey the same equation of state and constitutive relations, with spatially varying material properties; numerical dissipation at interfaces gives rise to a (numerical) mixture region in which appropriate rules must be specified to prevent spurious errors at interfaces. In addition to the total mass conservation equation (4.1a), $K-1$ species conservation equations are solved in both conservative form as in Eq. (4.6a) and in non-conservative form to maintain interfacial equilibrium conditions for velocity, pressure and temperature (Alahyari Beig & Johnsen, 2015),

$$\frac{\partial \alpha^{(k)}}{\partial t} + u_j \frac{\partial \alpha^{(k)}}{\partial x_j} = \Gamma^{(k)} \frac{\partial u_j}{\partial x_j}, \tag{2.34}$$

where $k = 1, ..., K-1$ and

$$\Gamma^{(k)} = \frac{\alpha^{(k)}}{K_s^{(k)}} \left(\frac{1}{\sum_l \frac{\alpha^{(l)}}{K_s^{(l)}}} - K_s^{(k)} \right), \qquad K_s^{(k)} = \rho^{(k)} (a^{(k)})^2 = \frac{n^{(k)}(p + B^{(k)})}{(1 - \rho^{(k)} b^{(k)})}. \tag{2.35}$$

The right-hand-side of this equation is sometimes set to zero (Allaire *et al.*, 2002; Massoni *et al.*, 2002; Murrone & Guillard, 2005; Perigaud & Saurel, 2005; Shukla *et al.*, 2010); however, this term is necessary to accurately represent compressible multiphase problems.

The pressure and temperature are computed based on the internal energy as follows:

$$p = \frac{E - \rho\frac{u_i^2}{2} - \rho e^{(e)} - \sum_k \rho^{(k)}\alpha^{(k)}q^{(k)} - \sum_k \alpha^{(k)}\frac{n^{(k)}B^{(k)}(1-\rho^{(k)}b^{(k)})}{n^{(k)}-1}}{\sum_k \alpha^{(k)}\frac{1}{n^{(k)}-1}}, \tag{2.36a}$$

$$T = \frac{E - \rho\frac{u_i^2}{2} - \rho e^{(e)} - \sum_k \rho^{(k)}\alpha^{(k)}q^{(k)} - \sum_k \alpha^{(k)}(1-\rho^{(k)}b^{(k)})B^{(k)}}{\sum_k \rho^{(k)}\alpha^{(k)}c^{(k)}}, \tag{2.36b}$$

where terms with $\rho^{(k)}\alpha^{(k)}$ are calculated using Eq. (4.6a), terms with $\alpha^{(k)}$ only are calculated using Eq. (4.6b), as described in Alahyari Beig & Johnsen (2015). Thus, the internal energy equation is calculated as follows,

$$\rho e = p\sum_k \alpha^{(k)}\frac{(1-\rho^{(k)}b^{(k)})}{n^{(k)}-1} + \sum_k \alpha^{(k)}\frac{n^{(k)}B^{(k)}(1-\rho^{(k)}b^{(k)})}{n^{(k)}-1} + \rho^{(k)}\alpha^{(k)}q^{(k)}, \text{(pressure}-\text{wise)}, \tag{2.37}$$

$$= T\sum_k \rho^{(k)}\alpha^{(k)}c^{(k)} + \sum_k \alpha^{(k)}B^{(k)}(1-\rho^{(k)}b^{(k)}) + \rho^{(k)}\alpha^{(k)}q^{(k)}, \qquad \text{(temperature}-\text{wise)}. \tag{2.38}$$

For simplicity and without loss of generality, mixture material properties ϕ (e.g., moduli, viscosities, thermal conductivity, etc.) are weighted by the volume fraction:

$$\phi = \sum_k \alpha^{(k)}\phi^{(k)}. \tag{2.39}$$

2.5 Numerical Method

Without loss of generality, we consider the one-dimensional form of the equations,

$$\left.\frac{dU}{dt}\right|_i = -\frac{F_{i+1/2} - F_{i-1/2}}{\Delta x} + D_i(U) + S_i(U), \tag{2.40}$$

where U denotes the conservative variables, F the convective flux, the D diffusion operator and S source terms. Our overall approach is based on explicit finite differences in space and explicit time-marching.

2.5.1 Temporal Discretization

For time marching, we use the standard explicit fourth-order Runge-Kutta scheme. The time-step constraint is calculated by accounting for advection and diffusion,

$$\Delta t = \min\left(\nu\frac{\Delta x}{\zeta_{max}}, \nu_\mu\frac{\Delta x^2}{(\mu_s/\rho)}, \nu_\kappa\frac{\Delta x^2}{(\kappa/\rho c)}\right), \tag{2.41}$$

where Δx is the mesh size, ζ_{max} the maximum wave speed in the system (and computational domain), ν is the Courant number, ν_μ and ν_r are the Von Neumann numbers for viscous and thermal diffusion. We set $\nu = 0.85$, $\nu_\mu = \nu_\kappa = 0.125$.

Since $G \geq 0$, the maximum wave speed is calculated, as shown from the analysis in §2.4.1.3, as follows:

$$\zeta_{max} = \max_j\left(|u| \pm \sqrt{\frac{n(p+B)}{\rho(1-\rho b)} + \frac{4G/3 + \tau^{(e)}_{jj}}{\rho}}\right)_j. \tag{2.42}$$

2.5.2 Spatial Discretization

The spatial discretization is based on a solution-adaptive approach that introduces numerical dissipation only where necessary. The discontinuity sensor of Henry de Frahan *et al.* (2015); Alahyari Beig & Johnsen (2015) detects shocks, contact discontinuities and material interfaces, such that the convective fluxes are computed as follows:

$$F_{i\pm1/2} = bF_{i\pm1/2}|_{central} + (1-b)F_{i\pm1/2}|_{HLL}, \tag{2.43}$$

where the subscripts "central" and "HLL" are explained below, $b = 1$ is smooth regions and $b = 0$ at discontinuities. The function

$$\Phi_A = \frac{4\phi_A}{(1+\phi_A)^2}, \qquad \phi_A = \frac{|A_R - A_L|}{A_R + A_L}, \tag{2.44}$$

where A is p, ρ or n, and L and R denote the left and right edge of a computational cell, is evaluated. If $\Phi_A > 0.0001\ \forall A$ in a given cell, the solution therein is considered discontinuous and the WENO approach of Johnsen & Colonius (2006) is used for all the primitive variables along with the HLL Riemann solver (Harten *et al.*, 1983) with appropriate correction for equations in non-conservative form (Saurel & Abgrall, 1999b); in a finite difference framework, this scheme is formally second-order accurate, but since it is applied at discontinuities only it does not affect the overall convergence rate. Otherwise, standard fourth-order explicit central differences are applied. In the diffusion and source terms, the derivatives are computed using explicit fourth-order central differences; if material properties are variable, their derivatives are calculated in non-conservative form. When solving Eq. (4.6b) with the source term, the numerical method's stiffness is significantly increased and, thus, the criterion $\Phi_A > 0.0001$ was set to solve the problems of interest. In the absence of the source term, the criterion is less restrictive (Alahyari Beig & Johnsen, 2015). In summary, the overall approach is globally fourth-order accurate in time and space in smooth problems. For problems with discontinuities, the convergence rate reduces to first-order accuracy, as expected. We note however that the fifth-order shock-capturing scheme significantly reduces the amount of dissipation in discontinuous regions.

2.6 Results

2.6.1 Wave Propagation Problem

Without loss of generality, we consider the Kelvin-Voigt model for a single material, i.e., the model viscoelastic medium with properties in Table 6.1. We non-dimensionalize the problem using a length scale of $L = 1$ mm and the relevant material properties. The thermal conductivity is $\kappa = 0.615$ W/(K m).

2.6.1.1 Convergence and Wave Speeds

We use a one-dimensional $p-$wave (acoustic) problem to verify the convergence rate of the overall scheme and that correct wave speeds are obtained. The initial conditions are

$$(\rho, u, v, p) = (1 + \Delta, 0, \Delta, (1 + nB)/n + \Delta), \tag{2.45}$$

with $\tau_{11}^{(e)} = \tau_{22}^{(e)} = \tau_{12}^{(e)} = 0$, and where $\Delta = \epsilon \sin^8(\pi x)$, on the periodic domain $x \in [0, 1]$. Values of $\epsilon = 10^{-4}$ and 10^{-1} are used to discriminate between different convergence behaviors. The initial density, pressure and $y-$velocity split into left- and right-moving waves propagating at speeds $\pm\sqrt{\frac{n(p+B)}{\rho(1-\rho b)} + \frac{4G/3+\tau_{11}^{(e)}}{\rho}}$. For this amplitude, the solution remains smooth throughout such that central differences are always used. The number of grid points is $N = 10, 20, 40, 80$, and 160. The L_2 error, evaluated after one period using the solution on $N = 1024$ as the reference for both Δs, is shown in Fig. 2.1 in gas ($\mu_b = \mu_s = 0$ and $G = 0$), Newtonian liquid ($\mu_b = \mu_s = 1$ Pa s and $G = 0$), elastic solid ($\mu_b = \mu_s = 0$ and $G = 1$ GPa), and viscoelastic solid ($\mu_b = \mu_s = 1$ Pa s and $G = 1$ GPa). The viscosity and shear modulus are set to these values to demonstrate their effect, if any, on the order of accuracy. For this problem, the Reynolds number is $Re = \rho a L/\mu_s = 1.57 \times 10^3$ and Cauchy number is $Ca = \rho a^2/G = 2.47$. For $\epsilon = 10^{-4}$, the problem remains sufficiently smooth that the sensor never gets activated, such that a fourth-order convergence rate is achieved. For $\epsilon = 10^{-1}$, the amplitude of the perturbation is sufficiently large that the wave steepens such that capturing is activated. As a result, the convergence rate reduces to first-order accuracy. Although not included here, similar results are obtained in a Zener medium (i.e., with relaxation) for both cases.

To verify that the correct wave speeds are obtained as shear modulus is varied, the same problem is considered with $N = 400$, $x \in [0, 2]$, $G = 10^{-6}$, 10^{-3}, 1, 10, 35 and 100 GPa. The viscosities are set to zero. Fig. 2.2 compares the numerically measured sounds speeds and their theoretical values, $\zeta_{1,2}$. The wave speeds, constant for a given modulus, are obtained by tracking the x-location and time of the peak density, and are scaled by the reference sound speed in the viscoelastic medium with $G = 0$, a_0. As the shear modulus is increased, the wave speed increases

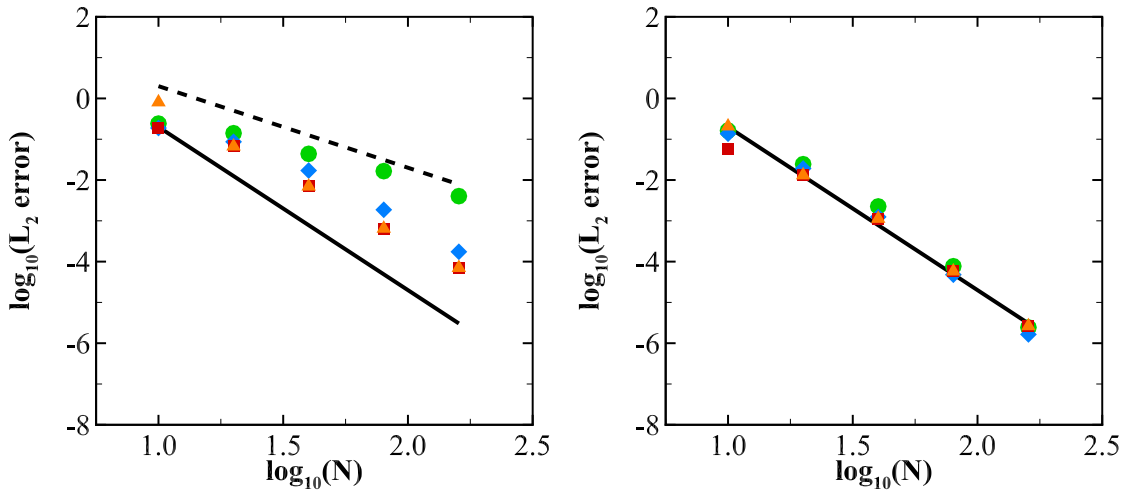

(a) $\Delta_1 = 10^{-1}\sin^8(\pi x)$. (b) $\Delta_2 = 10^{-4}\sin^8(\pi x)$.

Figure 2.1: L_2 error in pressure for the 1D wave-propagation problem. Green circles: gas ($\mu_b = \mu_s = 0$, $G = 0$); blue diamonds: Newtonian liquid ($\mu_b = \mu_s = 1$ Pa s, $G = 0$); red squares: elastic solid ($\mu_b = \mu_s = 0$, $G = 1$ GPa); orangle triangles: viscoelastic solid ($\mu_b = \mu_s = 1$ Pa s, $G = 1$ GPa); dashed black line: -2 slope; solid black line: -4.

accordingly. The agreement is excellent for all values of G under consideration.

2.6.1.2 Effects of Relaxation on $p-$ and $s-$Wave Propagation

We verify the implementation of relaxation effects and frequency dependence using the generalized Zener model. Without loss of generality, we consider a single relaxation time and compute the same problem, with $N = 600$, $x \in [-1.5, 1.5]$ to obtain both the $p-$ and $s-$waves. The initial single memory variable is set $\xi_{11}^{(1)} = \xi_{22}^{(1)} = \xi_{12}^{(1)} = 0$. The viscosities are also set to zero. The relaxation frequency is varied such that $\theta^{(1)} \in [1, 100]$ MHz, with a relaxation coefficient of $\varsigma^{(1)} = 1$ and $G = 2$ GPa, $G_r = 1$ GPa, all consistent with Eq. (3.15). The dependence of the $p-$ and $s-$waves on relaxation is shown in Fig. 2.3, with the waves calculated as described above using a least-squares fit by tracking the corresponding wave amplitude, and scaled by a_0. The results are as expected. At the lowest relaxation frequencies, the wave speeds agree with those corresponding to an unrelaxed shear modulus of $G = 2$ GPa. As the frequency is increased, the wave speeds decrease to reach the limit of the relaxed shear modulus at infinite frequency.

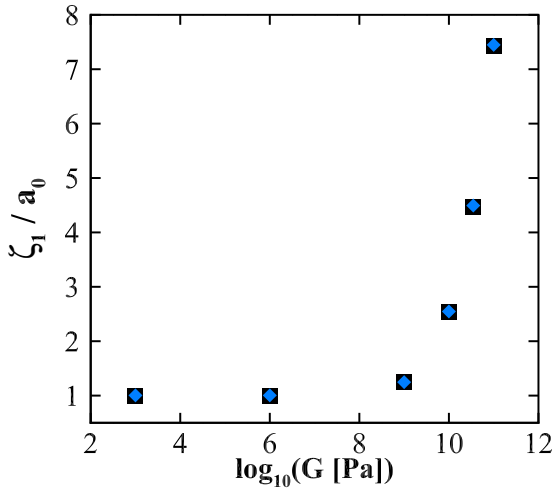

Figure 2.2: Comparison of the propagation speed of the $p-$waves in the 1D wave-propagation problem in a viscoelastic solid between theory (black squares) and simulations (blue diamonds).

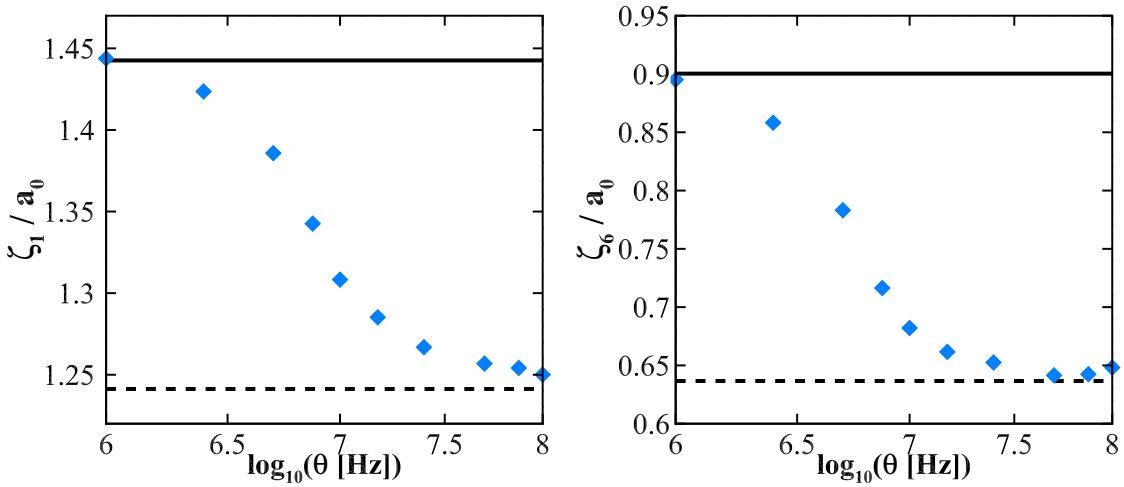

(a) $p-$wave.

(b) $s-$wave.

Figure 2.3: Dependence of the propagation speed of the $p-$ and $s-$waves on relaxation frequency for the 1D wave-propagation problem. Black solid line: theoretical wave speed for $G = 2$ GPa; black dotted line: theoretical wave speed for $G_r = 1$ GPa; blue diamonds: Simulation results.

2.6.2 Material Interface Advection Problem – Interfacial Conditions

We demonstrate that an extension of the five-equations multiphase model to (visco)elasticity can be performed while preserving the appropriate interfacial conditions (Abgrall, 1996; Shyue, 1998; Johnsen, 2011; Alahyari Beig & Johnsen, 2015). We adapt the 1D gas-liquid interface problem in Alahyari Beig & Johnsen (2015), replacing the liquid by a viscoelastic solid described by a

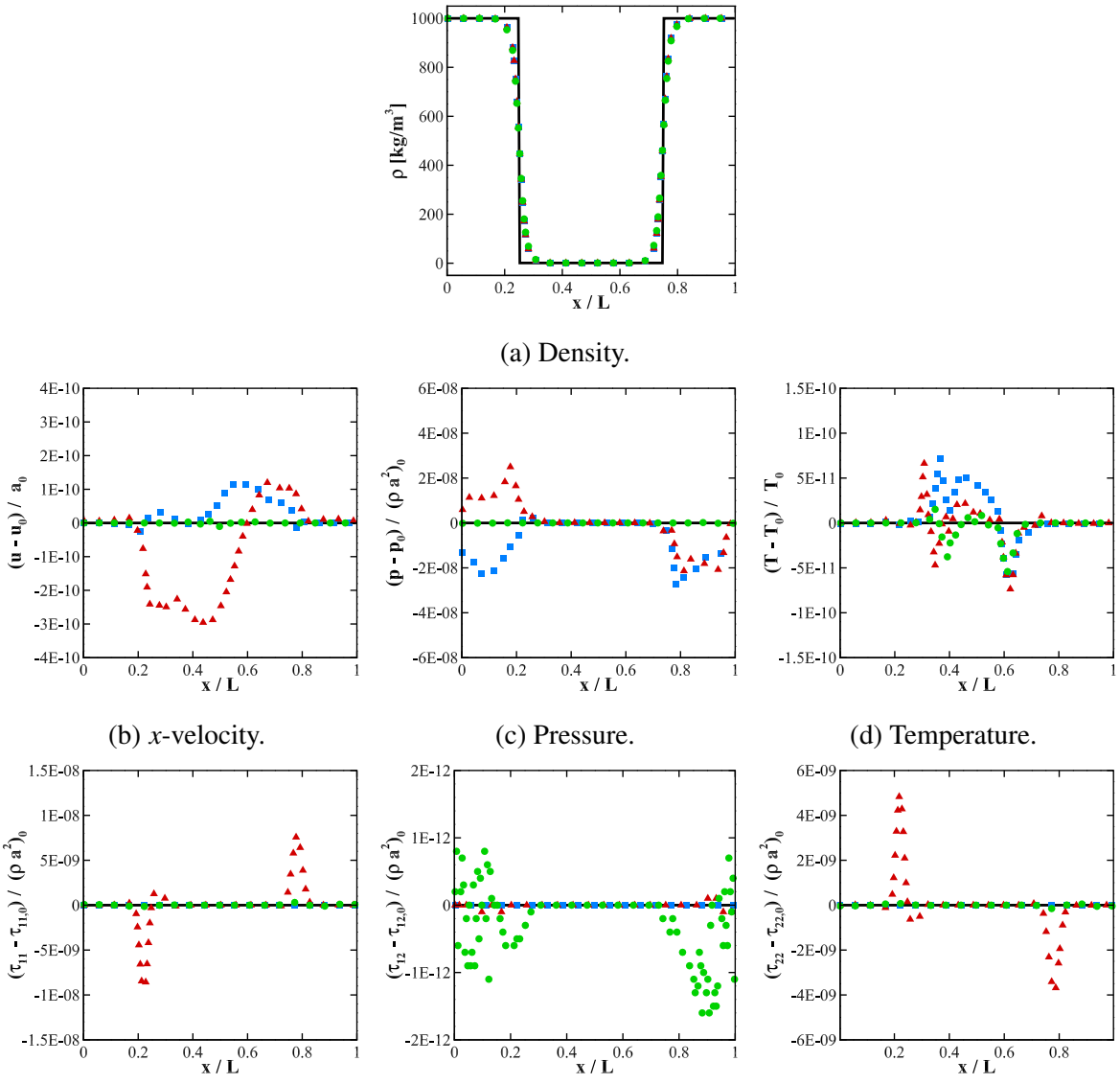

(a) Density.

(b) x-velocity. (c) Pressure. (d) Temperature.

(e) Elastic stress $\tau_{11}^{(e)}$. (f) Elastic stress $\tau_{12}^{(e)}$. (g) Elastic stress $\tau_{22}^{(e)}$.

Figure 2.4: Relative error in the interface advection problem after one period. Blue squares: Newtonian liquid ($G = 0$); red triangles: $G = 1$ MPa; green circles: $G = 1$ GPa; black line: exact solution.

Kelvin-Voigt model with the material properties of the model viscoelastic medium in Table 6.1.

The initial conditions are

$$(\rho, u, v, p) = \begin{cases} (1, 0.5, 0.5, 1/\gamma), & \text{if} \quad x/L \in [0.25, 0.75] \\ (1000, 0.5, 0.5, 1/\gamma), & \text{otherwise,} \end{cases} \tag{2.46}$$

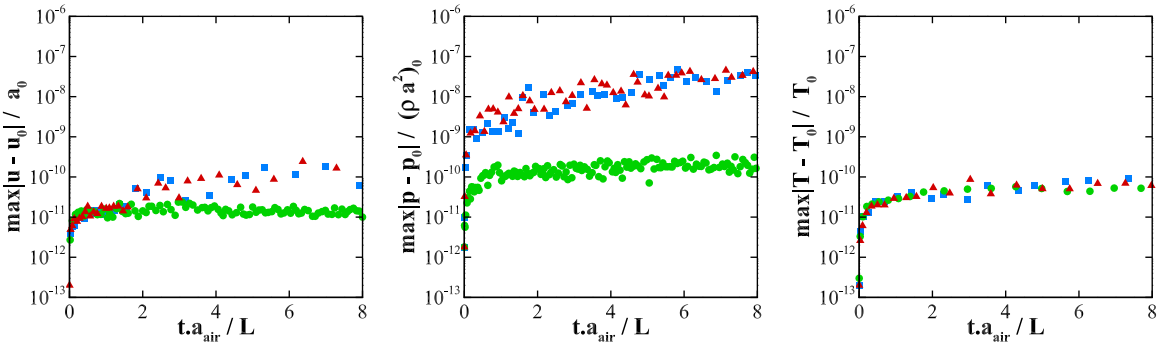

(a) x-velocity. (b) Pressure. (c) Temperature.

Figure 2.5: Time histories of normalized L_∞ errors for the interface advection problem through two periods. Blue squares: Newtonian medium; red triangles: viscoelastic medium ($\mu_b = \mu_s = 5$ mPa s, $G = 1$ MPa); green circles: viscoelastic medium ($\mu_b = \mu_s = 5$ mPa s, $G = 1$ GPa).

with $\tau_{11}^{(e)} = \tau_{22}^{(e)} = \tau_{12}^{(e)} = 0$ and γ is the n value for air from Table 6.1, and $L = 1$ mm. A constant, non-zero normal velocity is introduced to magnify any shear errors. The domain, $x \in [0, 1]$, is periodic with $N = 200$. For the model viscoelastic material, $\mu_b = \mu_s = 5$ mPa s, and $G = 1$ MPa and 1 GPa. For air, $\kappa = 0.026$ W/(K m), and for the model viscoelastic material, $\kappa = 0.615$ W/(K m). The density solution, normalized errors in velocities, pressure, temperature and stresses after the solution has traveled four domain lengths are plotted in Fig. 3.1, and the time histories of the errors are included in Fig. 3.2. Due to fixed precision arithmetic with quantities that differ by several orders of magnitude, the errors are not exactly at the round-off level, but are nevertheless of the similar order as those observed for water in Alahyari Beig & Johnsen (2015). The largest relative errors (observed in pressure) are on the order of 10^{-7} and remain bounded over time. Much smaller errors are observed for temperature, velocity and stresses. We conclude that our approach preserves the appropriate interface conditions for interface advection problems.

2.6.3 Elastic Medium Riemann Problem

We consider three one-dimensional Riemann problems in elastic media taken from Gavrilyuk *et al.* (2008) to verify the capability of our approach to represent discontinuities: five-wave shock tube, impact, and expansion problems, all for a single material. We evaluate the solution using the Lie derivative implementation. The domain is $x \in [0, 1]$, $L = 1$ mm, and $N = 200$. For comparison's

sake, the stiffened gas equation of state is used with $\rho = 1000$ kg/m^3, $n = 4.4$ and $B = 600$ MPa. The elastic medium is modeled using the Kelvin-Voigt approach with $G = 10$ GPa and zero viscosities. We compare our results to the analytical solution to elastic Riemann problems of Gavrilyuk *et al.* (2008); it is important to note that this "exact" analytical solution strictly applies to problems in which ρG is a constant. For problems in this section, the initial elastic stresses are $\tau_{11}^{(e)} = \tau_{22}^{(e)} = \tau_{12}^{(e)} = 0$.

2.6.3.1 Five-Wave Shock Tube Problem

An initial discontinuity in the tangential velocity (y-component) is superposed onto a pressure jump (1000:1) with initial conditions:

$$(\rho, u, v, p) = \begin{cases} (1000, 0, 100, 10^8) & \text{if} \quad x/L \in [0, 0.5], \\ (1000, 0, -100, 10^5) & \text{otherwise.} \end{cases} \tag{2.47}$$

The solution at $t = 64\ \mu s$ is shown in Fig. 2.6.

Five waves are observed: a right-moving shock, a stationary contact and a left-moving rarefaction (all visible in the density plot), as well as left- and right-propagating shear waves propagating more slowly than the shock and rarefaction, as expected from Eq. (2.32). At the contact discontinuity, the appropriate interface condition is that the normal stress, $-p + \tau_{11}^{(e)}$, be constant; pressure itself is discontinuous due to the presence of an elastic stress. Overall, our results with the Lie derivative match the analytical solution owing to the relatively small changes in density, i.e., ρG is approximately constant. Based on the eigenanalysis, the correct waves speeds and states are achieved.

Since capabilities to handle large pressure ratios are of interest, we consider the same problem

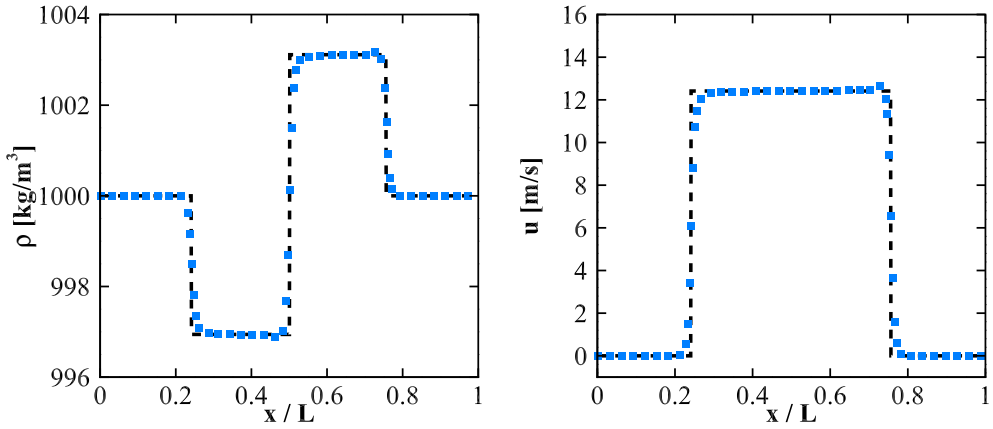

(a) Density.

(b) $x-$velocity.

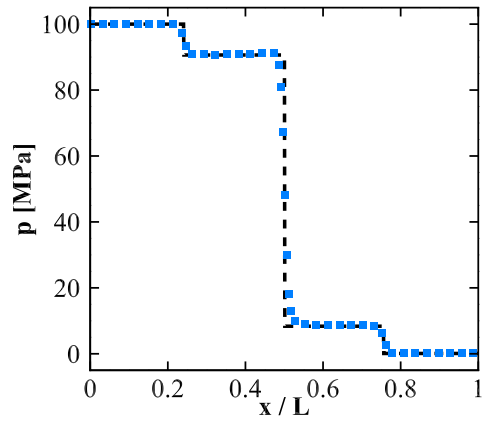

(c) Pressure.

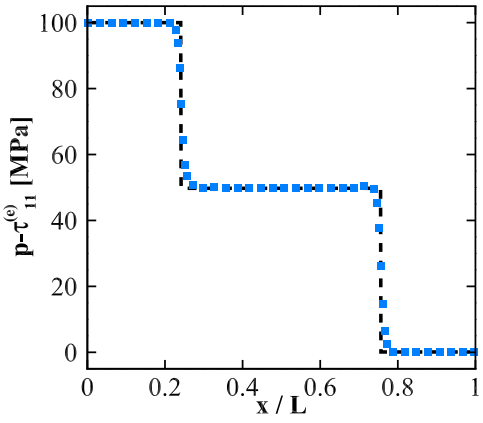

(d) Normal stress p - $\tau^{(e)}_{11}$.

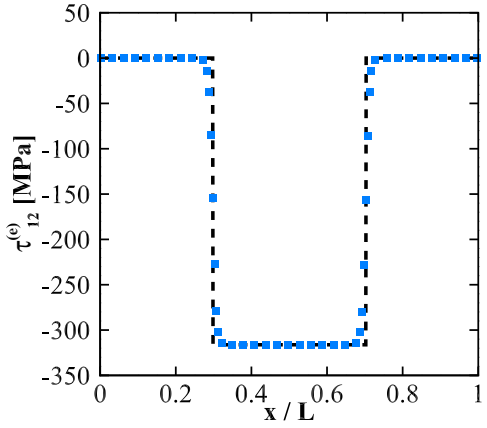

(e) Shear stress $\tau^{(e)}_{12}$.

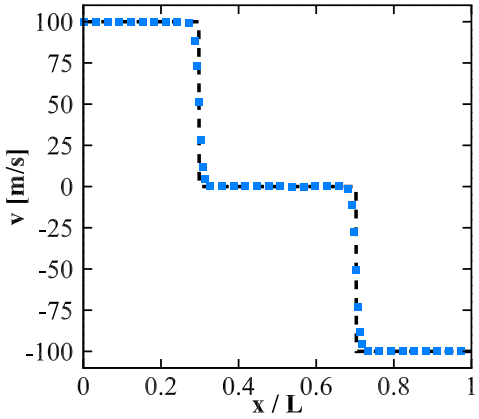

(f) $y-$velocity.

Figure 2.6: Shock tube problem in an elastic medium for pressure ratio 1000:1 at $t = 64\mu$s for the Lie derivative implementation (blue squares) along with the analytical solution (black dotted line).

with a higher pressure ratio of $10^5 : 1$, with initial conditions:

$$(\rho, u, v, p) = \begin{cases} (1000, 0, 100, 10^{10}) & \text{if} \quad x/L \in [0, 0.5], \\ (1000, 0, -100, 10^5) & \text{otherwise.} \end{cases} \tag{2.48}$$

For this problem, $G = 1$ GPa to represent a less stiff material. The solution is plotted at $t = 64\ \mu s$ in Fig. 2.7. The analytical solution assuming constant ρG (Gavrilyuk *et al.*, 2008) and the corresponding numerical solution with the Lie derivative exhibit several small differences: the shear wave speeds are slightly different and the values of y-velocity and $\tau_{12}^{(e)}$ are slightly larger between the shear waves. The small overshoots in the x-velocity and pressure just downstream of the shock are attributed to start-up errors (Johnsen, 2013) and are magnified for this stronger shock represented by the high-order accuracy.

2.6.3.2 Impact Problem

We consider weak ($U = 10$ m/s) and strong ($U = 1000$ m/s) impacts, with initial conditions

$$(\rho, u, v, p) = \begin{cases} (1000, U, 0, 10^5) & \text{if} \quad x/L \in [0, 0.5], \\ (1000, -U, 0, 10^5) & \text{otherwise.} \end{cases} \tag{2.49}$$

The solution is plotted at $t = 64\ \mu s$ (weak impact) and $t = 41\ \mu s$ (strong impact) in Figs. 2.8 and 2.9. Solution with the Lie implementation agrees with the analytical solution assuming constant ρG for the weak impact since density variations are small. For the strong impact, noticeable differences are observed: the analytical solution assuming constant ρG underpredicts pressure and the (negative) normal stress, $p - \tau_{11}^{(e)}$, results and overpredicts density between the shocks, compared to the numerical solutions. Again, the discrepancy is due to the invalidity of the constant ρG assumption necessary to obtain the analytical solution. The spike at the origin, also observed in Gavrilyuk *et al.* (2008), is attributed to overheating (Noh, 1987; Barton *et al.*, 2009); fixes have been proposed to address this issue (Fedkiw *et al.*, 1999). For both impact velocities, the effect of

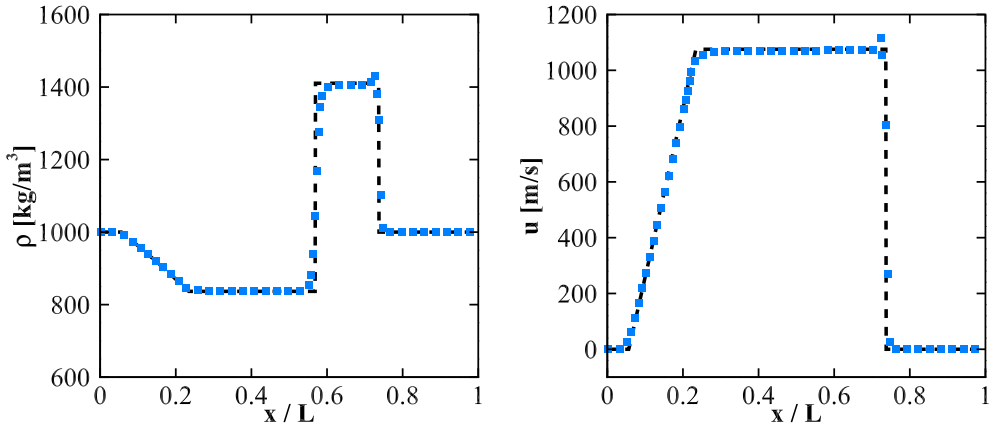

(a) Density.

(b) $x-$velocity.

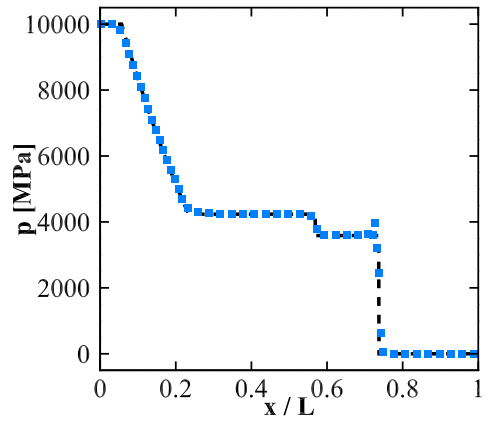

(c) Pressure.

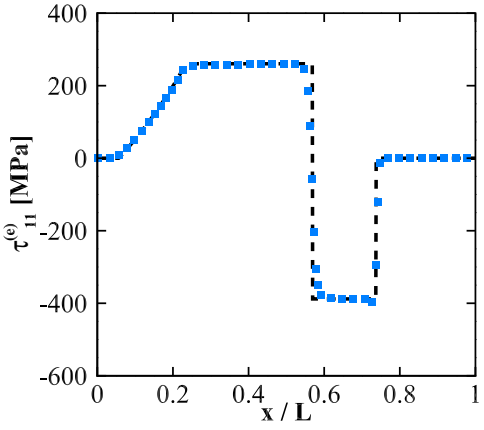

(d) Elastic stress $\tau^{(e)}_{11}$.

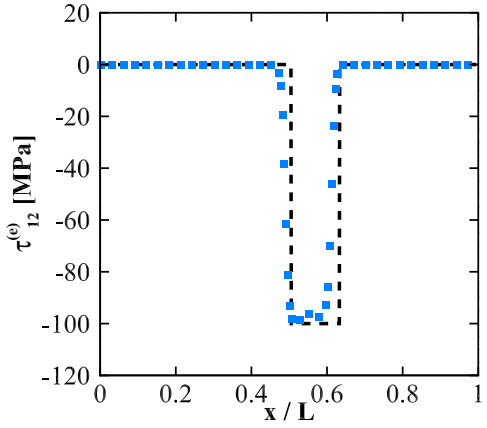

(e) Shear stress $\tau^{(e)}_{12}$.

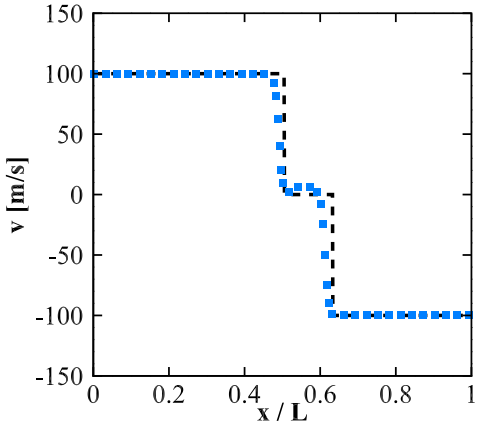

(f) $y-$velocity.

Figure 2.7: Shock tube problem in an elastic medium with pressure ratio 10^5 : 1 at $t = 64$ μs for the Lie derivative implementation (blue squares) along with the analytical solution (black dotted line).

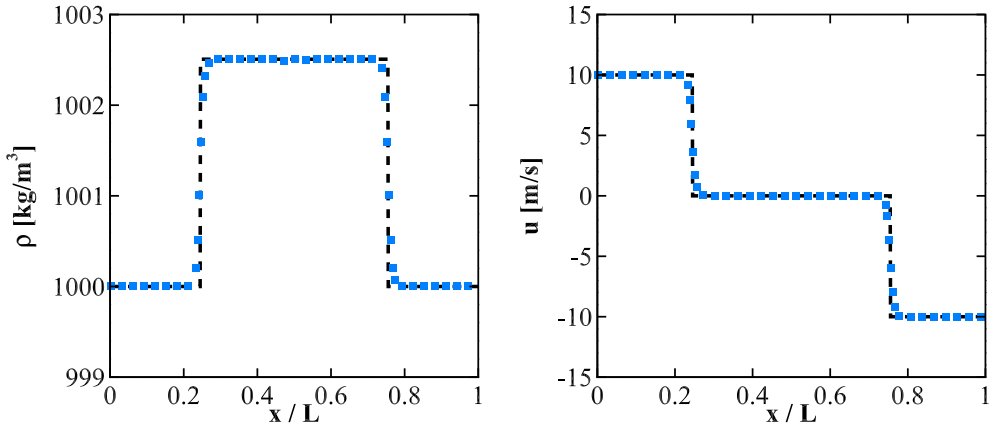

(a) Density.

(b) $x-$velocity.

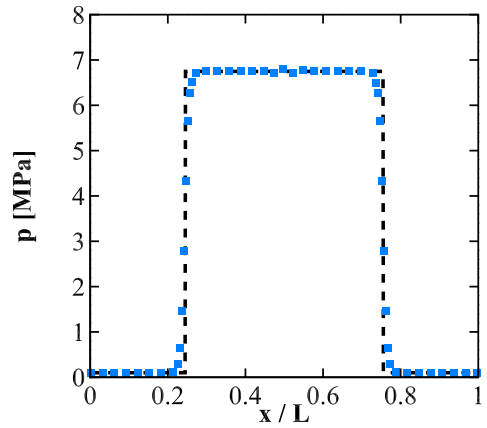

(c) Pressure.

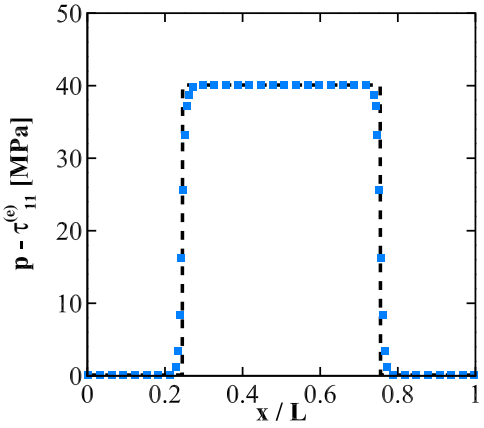

(d) Normal stress $p - \tau_{11}^{(e)}$.

Figure 2.8: Weak impact problem (20 m/s velocity difference) in an elastic medium at $t = 64$ μs for the Lie derivative implementation (blue squares) along with analytical solution (black dotted line).

the objective stress rates is negligible since the y-velocity is zero. Similar results are obtained at higher resolutions.

2.6.3.3 Expansion-Wave Problem

We consider weak ($U = 50$ m/s) and strong ($U = 800$ m/s) expansions, with initial conditions

$$(\rho, u, v, p) = \begin{cases} (1000, -U, 0, 10^5) & \text{if} \quad x/L \in [0, 0.5], \\ (1000, U, 0, 10^5) & \text{otherwise.} \end{cases} \tag{2.50}$$

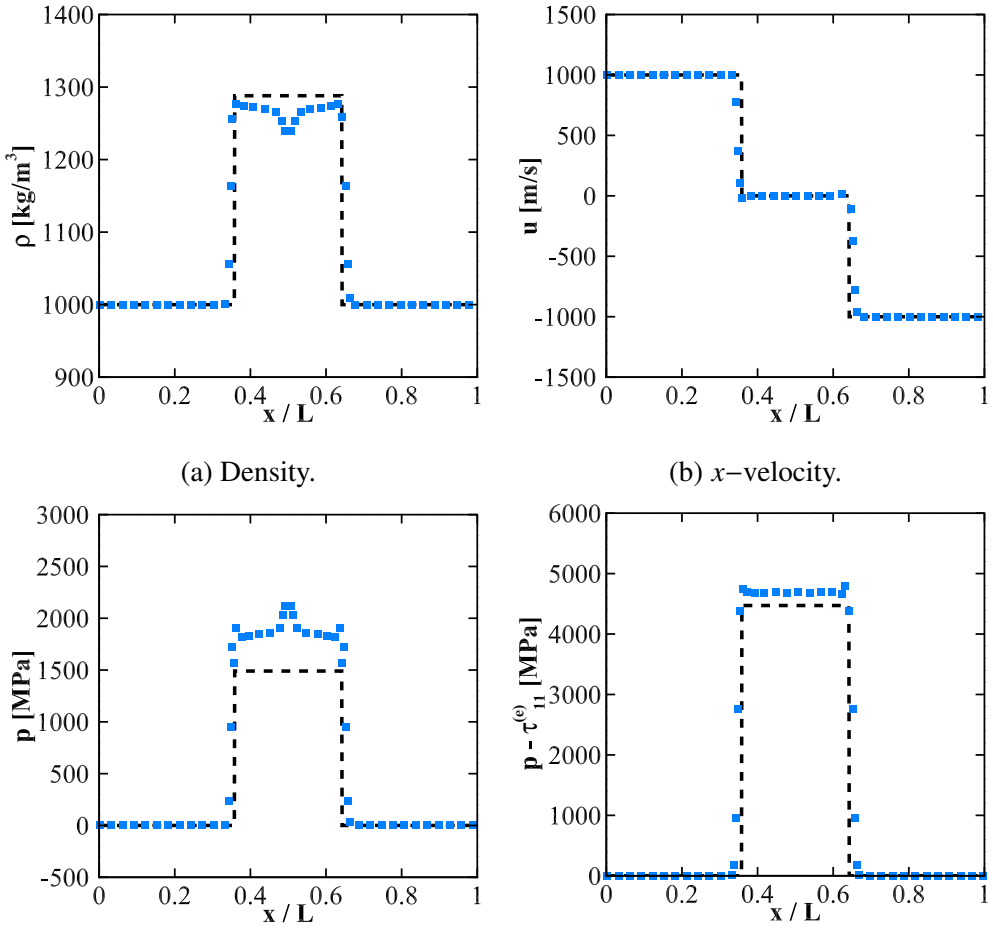

(a) Density.

(b) $x-$velocity.

(c) Pressure.

(d) Normal stress $p - \tau_{11}^{(e)}$.

Figure 2.9: Strong impact problem (2000 m/s velocity difference) in an elastic medium at $t = 41$ μs for the Lie derivative implementation (blue squares) along with the analytical solution (black dotted line).

The solution is plotted at $t = 64$ μs (weak expansion) and $t = 40$ μs (strong expansion) in Figs. 2.10 and 2.11. Here again, the numerical solution with Lie derivative implementation agree with the analytical solution for the weak expansion since density variations are small; overheating is discernible in the pressure at the origin. For the strong expansion, noticeable differences are observed: the analytical solution with constant ρG overpredicts both pressure and density. The effect of the objective stress rate is negligible since the y-velocity is zero. Again, the discrepancy is due to the invalidity of the constant ρG assumption necessary to compute the analytical solution.

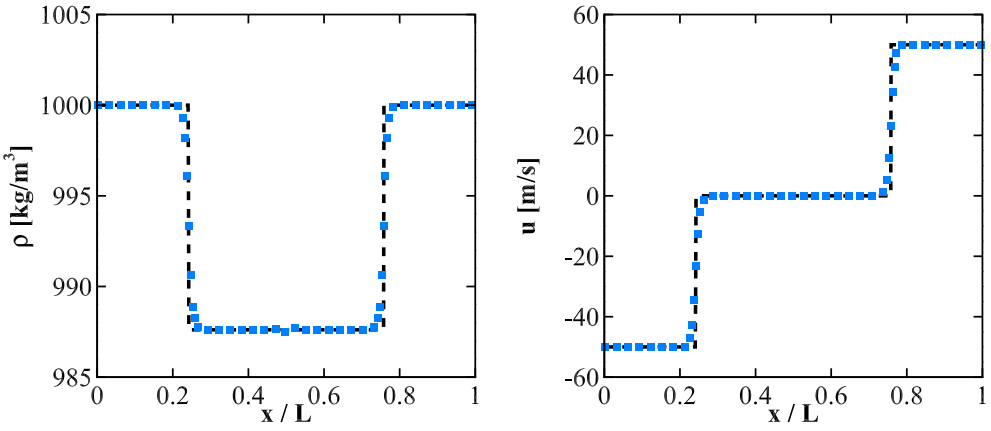

(a) Density.

(b) $x-$velocity.

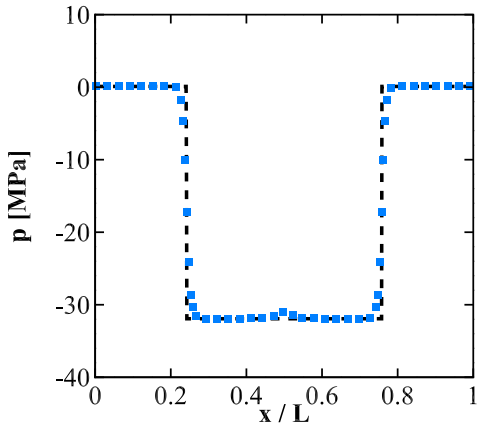

(c) Pressure.

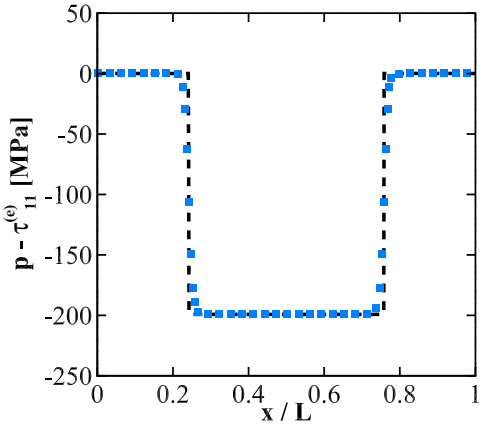

(d) Normal stress $p - \tau_{11}^{(e)}$.

Figure 2.10: Weak expansion problem (100 m/s velocity difference) in an elastic medium at $t = 64$ μs for the Lie derivative implementation (blue squares) along with the analytical solution (black dotted line).

2.6.4 Multi-material Riemann Problem

To verify the extension of the five-equations multiphase model to viscoelastic media with shocks, we extend the multi-material Riemann problem in Alahyari Beig & Johnsen (2015); Murrone & Guillard (2005); Allaire *et al.* (2002) to include viscoelasticity,

$$(\rho, u, v, p, \alpha^{(1)}) = \begin{cases} (1000, 0, 0, 10^9, 1) & \text{if} \quad x/L \in [0, 0.7], \\ (50, 0, 0, 10^5, 0) & \text{otherwise.} \end{cases} \tag{2.51}$$

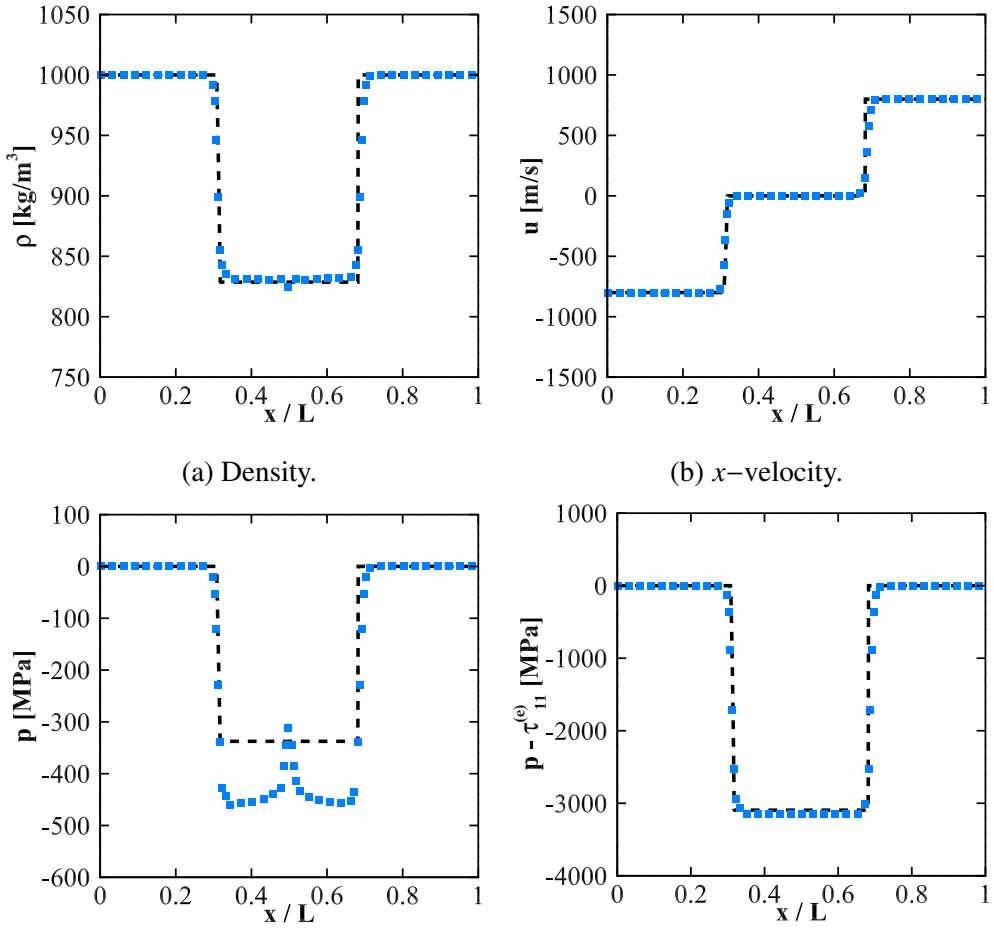

(a) Density.

(b) $x-$velocity.

(c) Pressure.

(d) Normal stress $p - \tau_{11}^{(e)}$.

Figure 2.11: Strong expansion problem (1600 m/s velocity difference) in an elastic medium at $t = 40$ μs for the Lie derivative implementation (blue squares) along with the analytical solution (black dotted line).

For comparison with the previous work, the right-hand-side term in Eq. (4.6b) is set to zero and the stiffened gas equation of state is used for the viscoelastic material and gas. The initial elastic stresses are $\tau_{11}^{(e)} = \tau_{22}^{(e)} = \tau_{12}^{(e)} = 0$. For the model viscoelastic material, $\kappa = 0.615$ W/(K m) and for the gas, $\kappa = 0.026$ W/(K m). The viscous ($\mu_b = \mu_s = 50$ mPa s) and Kelvin-Voigt ($\mu = 50$ mPa s and $G = 1$ GPa) solutions are plotted at $t = 240$ μs in Fig. 2.12, along with their respective analytical solutions. The analytical solutions were generated using the Riemann solver of Gavrilyuk *et al.* (2008), in which ρG is assumed constant. Our numerical results show good agreement with the analytical solution since the density ratio is large; all the relevant waves are captured, and no

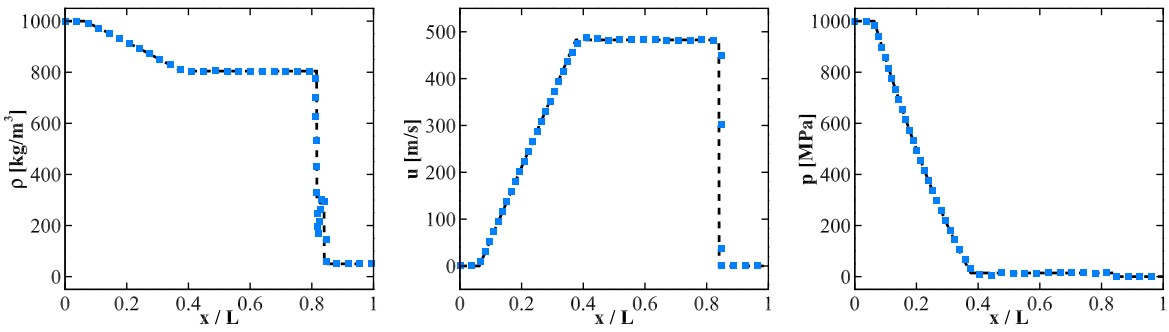

(a) Density. (b) $x-$velocity. (c) Pressure.

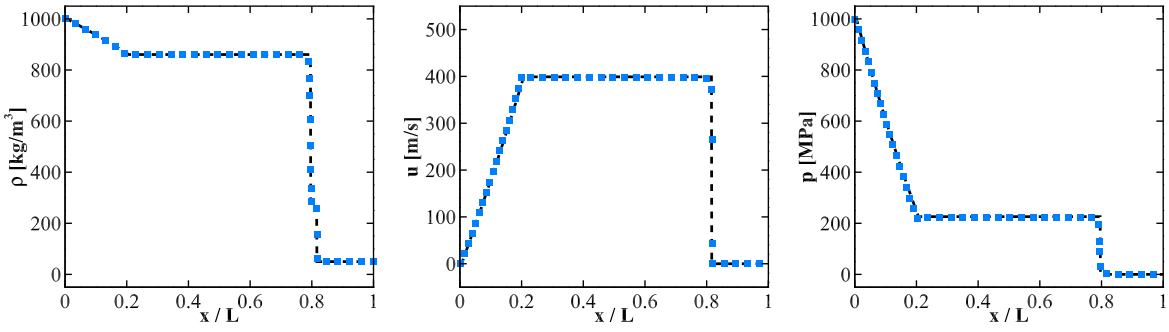

(d) Density. (e) $x-$velocity. (f) Pressure.

Figure 2.12: Multi-material Riemann problem at $t = 240\ \mu$s with analytical (black dashed line) and numerical (blue square) solutions for the viscous liquid-air shock wave (top row) and Kelvin-Voigt viscoelastic material-air shock wave (bottom row).

spurious oscillations are observed at any of the discontinuities for the Kelvin-Voigt solution. The solution with no elasticity exhibits an undershoot at the material interface, originating from the right-hand-side term in Eq. (4.6b) in the volume fraction equation, which can be addressed by implementing the equivalent six-equation multiphase model (Saurel *et al.*, 2009; Pelanti & Shyue, 2014).

2.6.5 Shock Wave-Viscoelastic Cylinder Interaction

Inspired by Lombard & Piraux (2004), we consider the two-dimensional interaction of a shock in water with a viscoelastic cylinder to assess the capabilities to represent multi-dimensional wave propagation in viscoelastic media. The problem set-up is shown in Fig. 3.8; half of the domain is simulated given the symmetry. The domain extends three initial bubble radii in each direction

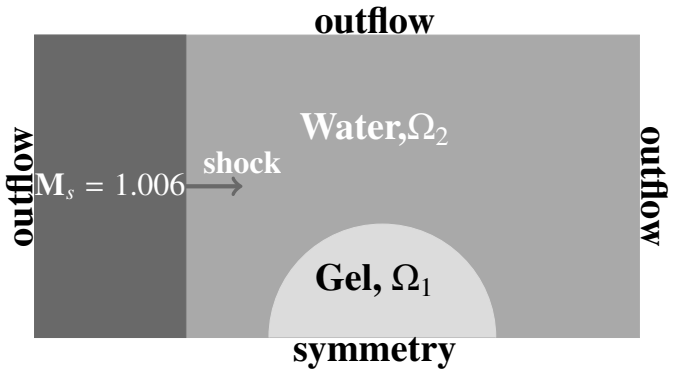

Figure 2.13: Shock-viscoelastic cylinder interaction setup, analogous to the problem considered by Lombard & Piraux (2004).

from the bubble center: $x \in$[-3 mm, 3 mm] and $y \in$[0 mm, 3 mm]. The initial cylinder radius is defined with a diffuse interface, similar to other multiphase studies (Shukla *et al.*, 2010), where the volume fraction is defined, $\alpha = \frac{1-\tanh(\psi)}{2}$, where $\psi = (R - R_o)/\Delta x$, $R = \sqrt{x^2 + y^2}$ and $R_o = 1$ mm is the initial cylinder radius. Given the volume fraction and for constant velocity and pressure, the conservative variables ϕ are computed using the mixture relation, $\phi = \alpha\phi_1 + (1 - \alpha)\phi_2$.

We use the generalized Zener model to represent the viscoelastic cylinder. The surrounding medium is water. For the viscoelastic cylinder, one relaxation time is considered with $\rho = 1000$ kg/m^3, $\mu_b = 50$ mPa s, $G = 1$ GPa, $G_r = 0.5$ GPa, $\varsigma^{(1)} = 1$, and $\theta^{(1)} = 15$ MHz. The remaining material properties for water and the model viscoelastic medium are in Table 6.1. The shear modulus values were selected to be two orders of magnitude higher than the incident shock wave pressure (i.e., $p = 10.1$ MPa) to highlight the effect of the elastic component of the stress inside the viscoelastic cylinder in the simulation. The shock wave is initialized at $x = -1.1 \times R_0$, using appropriate Rankine-Hugoniot conditions. The elastic contributions of the Cauchy stresses and the memory variables are initialized to zero. Four resolutions are considered: 32, 64, 128, 192, and 256 points per initial cylinder radius on a uniform mesh. Contours of the pressure and elastic component of the elastic stress tensor, $\tau_{12}^{(e)}$, are shown in Fig. 2.14, with 256 points per initial cylinder radius.

Upon interaction with the cylinder, the shock is partly reflected, partly transmitted, and diffracts around the cylinder (frame a). Due to the higher speed of sound in the viscoelastic material, the

transmitted shock travels faster than the diffracting shock. As expected from one-dimensional results, the shear wave travels more slowly than the p-wave. As the transmitted shock reaches the distal side of the viscoelastic cylinder, it is partially transmitted and reflected back into the cylinder (frame b). The reflected internal rarefaction then interacts with the shear wave as the diffracted shock leaves the domain (frames c and d). The resulting transmitted shock propagates radially outward (frames d, e, and f). The trapped shock in the viscoelastic cylinder gives rise to a distorted shear wave structure with alternating concentrated regions of negative and positive shear throughout the cylinder (frames d, e, and f). The shock wave minimally distorts the cylinder (in tension and shear).

The time evolution of two quantities of interest are the maximum pressure and elastic stress in the viscoelastic cylinder. For the elastic stress, we consider the von Mises stress,

$$\sigma_v = \sqrt{(\sigma_{11})^2 - \sigma_{11}\sigma_{22} + (\sigma_{22})^2 + 3(\sigma_{12})^2}, \tag{2.52}$$

which only incorporates the effects of pressure and all three components of the elastic stress. The time evolution of the maximum pressure and the von Mises stress is shown in Fig. 2.15 for the five spatial resolutions in the viscoelastic cylinder. The final time for the simulations is $t = 6\ \mu$s when the incoming shock has left the domain, at which point the trapped shock waves in the viscoelastic cylinder have a negligible effect. The average maximum pressure experienced by the viscoelastic cylinder during the simulation is approximately 12 MPa, which is expected as most of the incoming shock wave is transmitted into the cylinder since the acoustic impedance mismatch between the water and the viscoelastic gel is minimal. Using the von Mises stress, the maximum elastic strains, i.e., the von Mises strain, can be computed (applying Hooke's Law) and correspond to approximately 1.5% von Mises strain, thus justifying the small-strain approximation. The trapped transmitted shock (p-wave) is reflected back into the viscoelastic cylinder, generating the largest elastic stresses from $t = 2$ to $3\ \mu$s. The elastic stresses subsequently diminish substantially after the first internal reflection at $t = 3\ \mu$s, as expected as the shock is transmitted mostly out of the cylin-

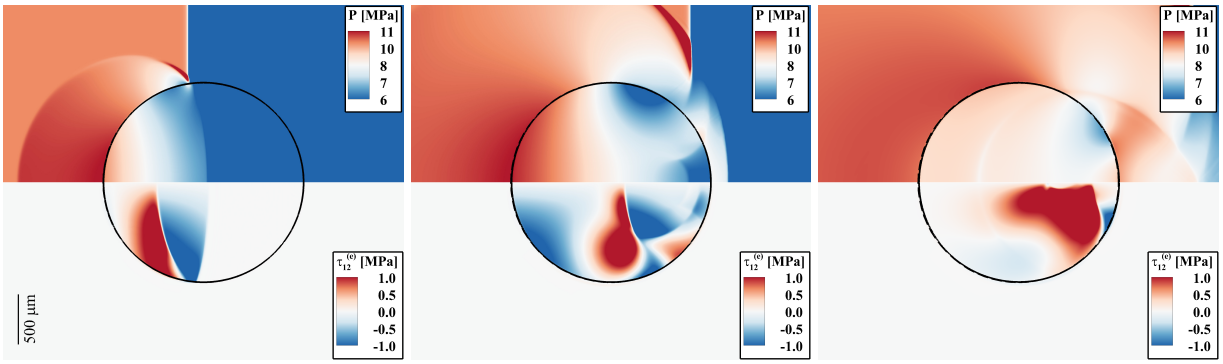

(a) time = 600 ns. (b) time = 1.2 μs. (c) time = 1.8 μs.

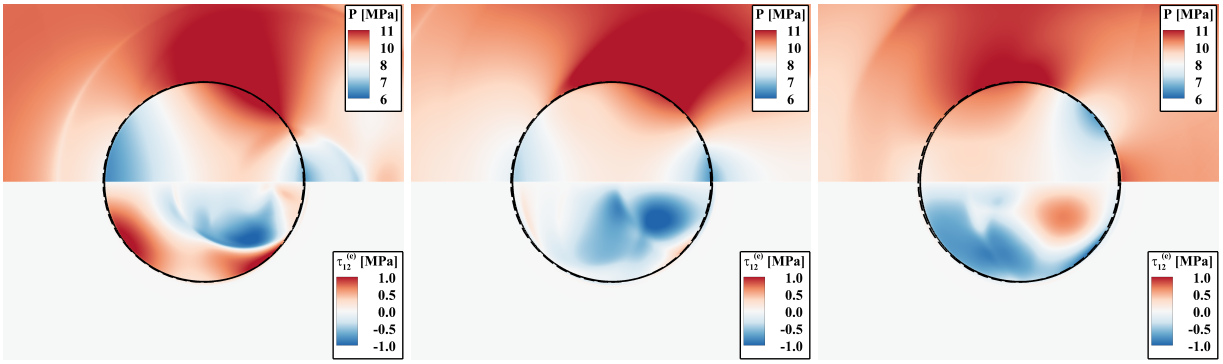

(d) time = 2.4 μs. (e) time = 3 μs. (f) time = 3.6 μs.

Figure 2.14: Pressure (top) and elastic component of the stress tensor, $\tau_{12}^{(e)}$, (bottom) contours for the 2D interaction of a Mach 1.006 shock in water with a Zener-like viscoelastic medium with $G = 1$ GPa and $G_r = 0.5$ GPa. Dashed black: the initial cylinder location; solid black line: instantaneous interface location.

der; the remaining contributions are due to subsequent interactions with the slower shear wave. The pressure and stresses are not yet converged at the highest resolution presented here. Higher resolution would be needed to achieve convergence. Such interactions, where a shock, e.g., produced by a collapsing bubble, leads to $p-$ and $s-$waves in the viscoelastic medium, are of interest when studying damage caused by the internal wave reflections in solids and the subject of future work discussed in Chapter 7.

2.7 Numerical Framework Validation

We validate our numerical framework detailed for shock-induced bubble collapse problems. Based on the experiments of Bourne & Field (1992), we consider the interaction of a shock wave with

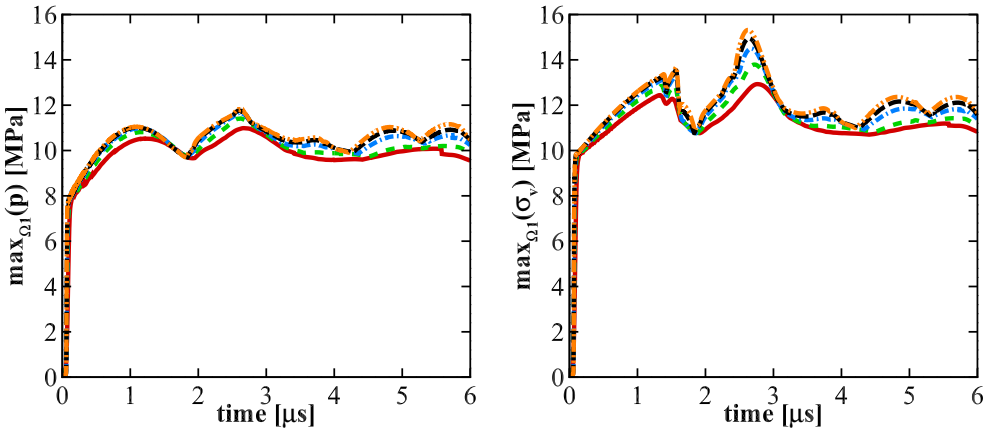

(a) Maximum pressure.

(b) Maximum von Mises stress, σ_v.

Figure 2.15: Time evolution of quantities of interest in the 2D shock-viscoelastic cylinder interaction in the cylinder with 32 (solid red), 64 (green dash), 128 (blue dash-dot), 192 (black long dash), and 256 (orange dash-dot-dot) points per initial bubble radius.

a 2D (cylindrical) bubble in a gel. This problem has motivated computational studies (Ball *et al.*, 2000), though generally the gel is replaced by water in simulations. The problem set-up is shown in Fig. 3.8; half of the domain is simulated given the symmetry. The domain size extends three bubble radii in each direction from the bubble center. The initial bubble radius and post-shock pressure are initialized to match the experimental values. The ambient temperature $300K$ and the shock is initialized using the Rankine-Hugoniot conditions. The source term in the multi-material framework is neglected and the Kelvin-Voigt model is used to represent the gel. Based on the experiments, the gel has a density $\rho = 970$ kg/m^3 and shear modulus $G = 8.35$ kPa. The stiffened-gas equation of state is used for the gel with $n = 2.35$ and $B = 1$ GPa and the air properties are provided in Table 6.1. A resolution of 256 points per initial bubble radius is used, such that $N_x = 1536$ and $N_y = 768$.

To qualitatively illustrate the dynamics, a time series of numerical Schlieren,

$$f_{ij} = 1 - \exp\left[-(0.1 + 0.9\alpha_{ij})\frac{|\nabla\rho|_{ij}}{|\nabla\rho|_{max}}\right], \tag{2.53}$$

and pressure contours are shown in Fig. 2.17. The domain in the plots is $x \in$[-6 μm, 6 μm] and $y \in$[0μm, 5.3 μm]. Upon interaction of the shock wave with the bubble, a rarefaction wave is

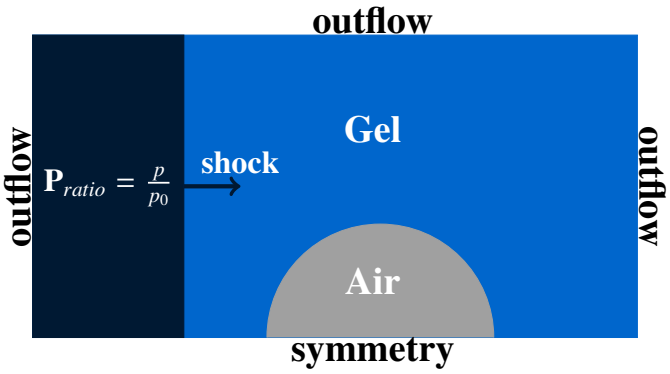

Figure 2.16: Bubble collapse setup, analogous to the experiments by Bourne & Field (1992).

reflected into the surroundings and a shock wave is transmitted into the bubble, while the incoming shock wave diffracts around the bubble (frame a). As the bubble collapses, the transmitted shock wave is trapped in the bubble (frame b). A right-moving re-entrant jet forms on the proximal side (frame c) and subsequently impacts the distal side (frame d) at collapse, thus generating an outward-propagating water-hammer shock wave (frame e). Thereafter, the bubble takes the form of vortex lines and convects downstream (frame f). For a quantitative assessment, we compare the re-entrant jet velocity and bubble collapse time achieved for selected initial bubble sizes and shock pressures with the experiments in Table 2.2. For selected sets of parameters, reasonable agreement is achieved, especially for cases with high shock pressures (greater than 0.5 GPa) and 6 mm cavity diameter. We note that the viscoelasticity of the gel has negligible effects on the dynamics; nevertheless, this problem illustrates the robustness of our approach.

2.8 Conclusions

We introduce a novel Eulerian approach for numerical simulations of wave propagation in heterogeneous viscoelastic media, with application to compressible materials described by linear constitutive relations, specifically Maxwell, Kelvin-Voigt or generalized Zener models. We extend the five-equations multiphase, interface-capturing model, based on the idea that all the materials (gases, liquids, solids) obey the same equation of state with spatially varying properties, to incorporate the constitutive relation; interfaces are thus represented by discontinuities in material

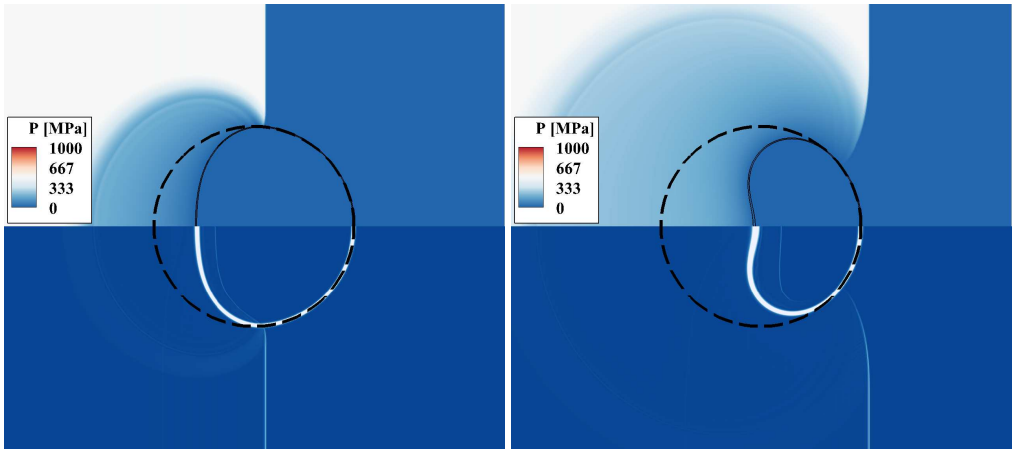

(a) time = 2.0 μs. (b) time = 3.6 μs.

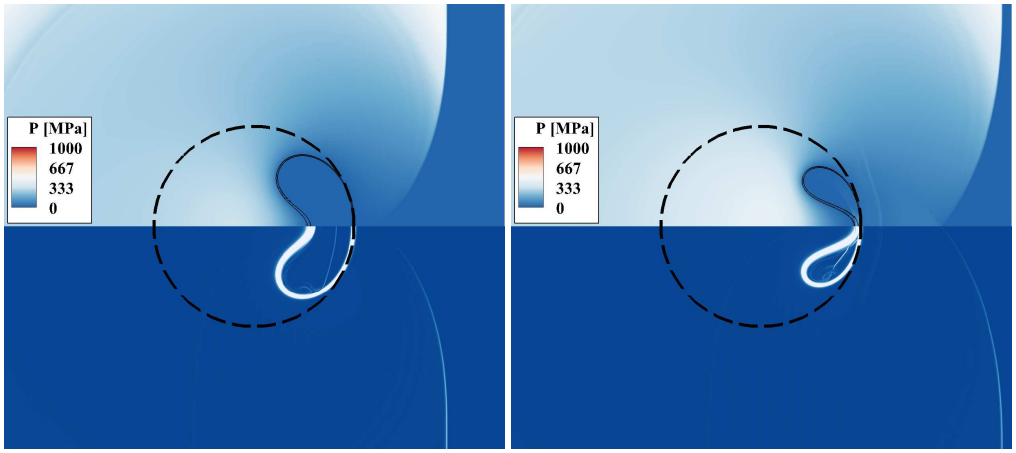

(c) time = 5.0 μs. (d) time = 5.8 μs.

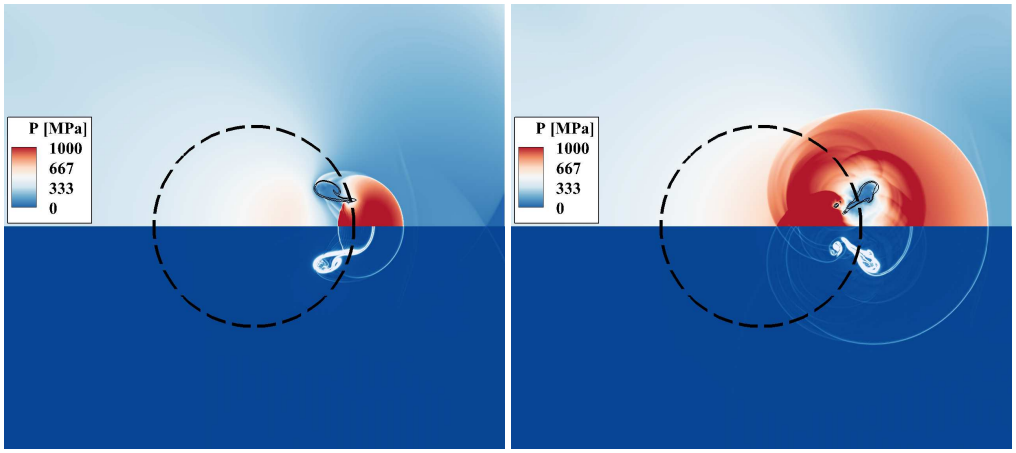

(e) time = 6.6 μs. (f) time = 7.8 μs.

Figure 2.17: Pressure (top) with density line contours and numerical Schlieren (bottom) contours for the 2D shock-bubble interaction in a viscoelastic medium with $G = 8.35$ kPa. Shock pressure: 0.5 GPa; bubble diameter: 6 mm.

properties. To represent strains in an Eulerian framework, we utilize a hypoelastic model and implement the Lie objective derivative of the constitutive relations to evolve the strain rates instead of strains. As a result, additional evolution equations must be solved for the components of the elastic stress tensor and stress relaxation terms. Our numerical framework is explicit in time and space, and high-order accurate. The spatial scheme is based on a solution-adaptive approach, where central differences are used in smooth regions and high-order shock capturing at discontinuities (material interfaces, contacts and shocks). The method is verified using a stringent suite of test problems involving smooth wave, shock, shear and contact waves problems in viscoelastic media. At least fourth-order accuracy is achieved in smooth problems, and the correct wave speeds are obtained. Eigenanalysis confirms that our Lie derivative implementation yields correct results. Spurious pressure and temperature errors at interfaces are shown to be prevented, and all wave families are accurately represented. We consider a two-dimensional problem to further demonstrate the robustness of the method (shock-viscoelastic solid interaction). Overall, this work advances our capabilities to compute fully coupled fluid-solid problems. Further investigations into the inclusion of more complex constitutive relations, particularly those involving finite deformations, will be pursued in the future.

Table 2.2: Comparisons of various quantities of interest between the simulations (sim.) of shock-bubble interaction with experimental (exp.) results Bourne & Field (1992).

Shock Pressure (GPa)	Cavity diameter (mm)	Jet velocity (m/s)		Collapse time (μs)	
		Exp.	Present sim.	Exp.	Present sim.
1.9	3	4000±2000	2860	1.0±0.5	1.4
0.5	6	1500±400	1530	5±1	5.8
1.9	6	3300±300	2861	1.8±0.2	2.7
3.5	6	8000±4000	3817	1±0.5	2
1.9	12	1500±200	2861	8±1	5.7

CHAPTER 3

A high-order accurate AUSM$^+$-up approach for simulations of compressible multiphase flows with linear viscoelasticity

This chapter is adapted from Rodriguez *et al.* (2018).

3.1 Abstract

An Eulerian approach for simulations of wave propagation in multiphase, viscoelastic media is developed in the context of the Advection Upstream Splitting Method (AUSM). We extend the AUSM scheme to the five-equation model for simulations of interfaces between gases, liquids, and solids with constitutive relations appropriately transported. In this framework, the solid's deformations are assumed to be infinitesimally small such that they can be modeled using linear viscoelastic models, e.g., generalized Zener. The Eulerian framework addresses the challenge of calculating strains, more naturally expressed in a Lagrangian framework, by using a hypoelastic model that takes an objective Lie derivative of the constitutive relation to transform strains into velocity gradients. Our approach introduces elastic stresses in the convective fluxes that are treated by generalizing AUSM flux-vector splitting (FVS) to account for the Cauchy stress tensor. We determine an appropriate discretization of non-conservative equations that appear in the five-equation multiphase model with AUSM schemes to prevent spurious oscillations at material interfaces. The

framework's spatial scheme is solution-adaptive with a discontinuity sensor discriminating between smooth and discontinuous regions. The smooth regions are computed using explicit high-order central differences. At discontinuities regions (i.e., shocks, material interfaces and contacts), the convective fluxes are treated using a high-order Weighted Essentially Non-Oscillatory (WENO) scheme with AUSM$^+$-up for upwinding. The framework is used to simulate 1D and 2D problems that demonstrate the ability to maintain equilibrium interfacial conditions and solve challenging multi-dimensional and multi-material problems.

3.2 Introduction

The increased sophistication of numerical techniques for compressible multiphase flows has enabled studies of implosions, explosions, and ballistics, and with them the growing need to accurately resolve features with high-frequency contents (e.g., shock waves) propagating into heterogeneous media. These flows involve regions of low Mach number flows in homogeneous solids or liquids, while Mach numbers can be supersonic in gas/liquid mixture regions where the sound speed can be as low as tens of meters per second. Shocks emitted from implosions propagate into surrounding media, causing permanent deformations and possibly material loss. An example of interest is cavitating bubble clouds collapsing over a hydrofoil's surface (Reisman *et al.*, 1998; Gnanaskandan & Mahesh, 2015; Ganesh *et al.*, 2016). Computing such flows requires high-order accuracy to resolve broadband motions, robustness to be applicable across a range of Mach numbers (including nearly incompressible flow), and computational efficiency to represent a wide range of scales (e.g., bubble clouds, cavitation sheets, turbulence). Flux-difference splitting (FDS) or flux-vector splitting (FVS) are common approaches to address these issues. FDS schemes are popular given their relatively simple implementation. However, representation of flows across a wide range of Mach numbers is not straightforward. On the other hand, FVS schemes, in particular the AUSM schemes first developed by Liou and Steffen (Liou & Steffen, 1993), are capable of computing all-speed flows (Liou, 2006; Shima & Kitamura, 2011) and multiphase flows (Paillère

et al., 2003; Evje & Fjelde, 2003; Chang & Liou, 2003, 2007; Liou *et al.*, 2008; Kitamura *et al.*, 2014).

AUSM schemes have been used to study multiphase implosions, shock-wave propagation, and shock-droplet problems involving gases and liquids (Liou *et al.*, 2008). Here, the motivation is to develop a coupled fluid-solid approach to study problems such as cavitation bubbles collapsing near rigid materials. The extension of an Eulerian framework to represent deformations, more adequately expressed in a Lagrangian framework, is non-trivial. Two major approaches have been pursued in the literature (Gavrilyuk *et al.*, 2008): Godunov-based (hyperelastic models) and conventional (hypoelastic models). The former accounts for finite deformations and ensures thermodynamic consistency in an Eulerian framework. This approach has been used in conjunction with FDS schemes to study ballistics (Barton *et al.*, 2011, 2013), and implosions (López Ortega *et al.*, 2015) with interface-tracking approaches and ballistics with interface-capturing approaches (Ndanou *et al.*, 2015). However, it is not clear how to implement FVS schemes with the Godunov approach, specifically, the fluxes involving the deformation tensor. Leveraging our previous work (Rodriguez & Johnsen, 2018), we follow the hypoelastic approach as it is possible to formulate an Eulerian framework for simple linear viscoelastic models for materials under the small-strain assumption. This limitation is acceptable for problems with small deformations, e.g., for materials with large Young's modulus relative to the pressure loads. An objective Lie temporal derivative of the elastic contribution of the Cauchy stress tensor is taken, thus transforming Lagrangian strains in the constitutive relation into velocity gradients (Eringen, 1962). As a result, the convective fluxes are modified by additional elastic components, such that the implementation of FVS schemes as developed for the Euler equations where the Cauchy stress tensor involved only pressure is not trivial. We address this issue here for the AUSM scheme by generalizing flux vectors to Cauchy stress tensors describing linear viscoelastic constitutive relations.

The representation of material interfaces typically falls into one of two approaches: tracking or capturing. The former, while being able to resolve the interface exactly, involves solving non-conservative equations that may lead to conservation issues. AUSM schemes have been

used in interface-tracking approaches, e.g., the Ghost Fluid Method, in conjunction with arbitrary Lagrangian-Eulerian frameworks (Luo *et al.*, 2004; McGurn *et al.*, 2013). While conservation issues can be mitigated, the overall solver can become complicated and involves two different solvers, one for the flow and one for the solid dynamics, to be appropriately coupled. Moreover, comparisons of AUSM schemes and FDS schemes demonstrated AUSM schemes to be numerically stiffer (Luo *et al.*, 2004). In the latter approach, the interface is regularized over a few cells in a fashion that ensures conservation using a single-solver framework. Although the six-equation multiphase model has been used with AUSM schemes (Liou *et al.*, 2008), the five-equation model is appealing for the simplicity of its implementation and because it does not require the calculation of the complicated source terms present in the six-equation model. The five-equation multiphase model has been implemented successfully for FDS schemes that eliminate spurious errors due to the inconsistent treatment of primitive variables and maintain equilibrium conditions (Alahyari Beig & Johnsen, 2015). However, the five-equation model has yet to be extended to FVS-type schemes.

By following the analysis of Saurel & Abgrall (1999b); Johnsen & Colonius (2006) and using the AUSM$^+$-up scheme, we obtain the appropriate discretization for the non-conservative equations in the five-equation model, which prevent spurious errors at material interfaces. In an extensive study of AUSM schemes with high-order approaches, Scandaliato and Liou (Scandaliato & Liou, 2012) suggests utilizing characteristic variable reconstruction WENO with AUSM schemes to avoid the oscillations present in other reconstructions that would lead to a stiff scheme. We utilize primitive variable reconstruction WENO scheme of Johnsen & Colonius (2006) due to its straightforward implementation and ability to eliminate spurious errors. Our objective is to extend AUSM schemes to interface-capturing approaches for gas-liquid-solid flows in which the solid behaves in a linear viscoelastic fashion. Furthermore, we focus on high-order-accurate spatial discretizations that result in a single, solution-adaptive framework to compute compressible multiphase flows with viscoelasticity. The chapter is organized as follows. The physical model is first presented, followed by a description of the numerical model. Thereafter, the AUSM implementa-

tion for interface capturing and viscoelastic media is outlined. The approach is then tested using a series of one- and two-dimensional problems. Finally, the chapter is summarized, and future directions are outlined.

3.3 Physical Model

3.3.1 Equations of Motion

The equations governing the phenomena of interest are mass conservation, momentum and energy balance:

$$\frac{\partial \rho}{\partial t} + \frac{\partial}{\partial x_j}(\rho u_j) = 0, \tag{3.1a}$$

$$\frac{\partial}{\partial t}(\rho u_i) + \frac{\partial}{\partial x_j}(\rho u_i u_j - \sigma_{ij}) = 0, \tag{3.1b}$$

$$\frac{\partial E}{\partial t} + \frac{\partial}{\partial x_j}(E u_j - \sigma_{ij} u_i) = -\frac{\partial Q_k}{\partial x_k}, \tag{3.1c}$$

$$\frac{\partial}{\partial t}(\rho^{(k)} \alpha^{(k)}) + \frac{\partial}{\partial x_j}(\rho^{(k)} \alpha^{(k)} u_j) = 0, \tag{3.1d}$$

where ρ is the total density, u_i the velocity vector, σ_{ij} the Cauchy stress tensor, Q_k the heat flux, $\alpha^{(k)}$ the volume fraction of material k, $k = 1, ..., K-1$, K the total number of materials, and indices $i, j = 1, 2$, and 3. Eqs. (4.6a) are mass conservation equations for $K-1$ materials. Material k has volume fraction $\alpha^{(k)}$ and density $\rho^{(k)}$, with the following relations

$$\sum_k \rho^{(k)} \alpha^{(k)} = \rho, \qquad \sum_k \alpha^{(k)} = 1. \tag{3.2}$$

As described in §3.4.2, $K-1$ additional mass balance equations along with the total density balance equation, corresponding to the K materials, must be evolved. The total energy per unit volume, E,

is comprised of the internal, kinetic and elastic contributions:

$$E = \rho e + \frac{1}{2}\rho u_i^2 + \rho e^{(e)}. \tag{3.3}$$

The internal energy (per unit volume) ρe is determined through the equation of state described in the next section, and the elastic energy $\rho e^{(e)}$ is described in §3.3.3.

3.3.2 Equation of State

The Noble-Abel Stiffened-Gas (NASG) equation of state (EOS) (Le Métayer & Saurel, 2016) is used to relate the internal energy to pressure and temperature in gases, liquids and solids:

$$\rho e = \frac{p(1-\rho b)}{n-1} + \frac{nB(1-\rho b)}{n-1} + \rho q \tag{3.4a}$$

$$= \rho c T + B(1-\rho b) + \rho q, \tag{3.4b}$$

where T is the temperature and q, n, B, b and c are material properties empirically for liquids and solids (Harlow & Amsden, 1971; Le Métayer *et al.*, 2005; Le Métayer & Saurel, 2016). The equation reduces to the stiffened gas equation of state (Le Métayer *et al.*, 2005) with $b = 0$ and and modifying the other material properties appropriately. In the limit of ideal gases, $B = 0$, $b = 0$, $q = 0$, c is the specific heat at constant volume and $n = \gamma$ is the ratio of specific heats. Table 6.1 provides the values of the material properties used in this chapter.

Table 3.1: Material properties corresponding to different media described by the Noble-Abel Stiffened-Gas equation of state.

Property	Air	Water & Model Zener solid
n	1.4	1.19
b[m^3/kg$\times 10^{-4}$]	0	6.61
B[Pa$\times 10^6$]	0	702.8
q [kJ/kg]	0	-1.167
c [kJ/kg·K]	0.718	4.167

3.3.3 Constitutive Relations

Constitutive relations for the heat flux and Cauchy stress tensor are required. For the former, Fourier conduction describes the heat diffusion process:

$$Q_k = -\kappa \frac{\partial T}{\partial x_k}, \tag{3.5}$$

where κ is the thermal conductivity.

For the latter, we first define the strain-rate tensor and its deviatoric component,

$$\dot{\epsilon}_{ij} = \frac{1}{2}\left(\frac{\partial u_i}{\partial x_j} + \frac{\partial u_j}{\partial x_i}\right), \qquad \dot{\epsilon}^{(d)}_{ij} = \dot{\epsilon}_{ij} - \frac{1}{3}\dot{\epsilon}_{kk}\delta_{ij}, \tag{3.6}$$

where the dot denotes the Lie objective temporal derivative. The Cauchy stress tensor can be written in terms of isotropic (bulk) and deviatoric contributions,

$$\sigma_{ij} = -p\delta_{ij} + \mu_b \dot{\epsilon}_{kk}\delta_{ij} + \tau^{(d)}_{ij}, \tag{3.7}$$

where the first two terms are the mechanical pressure and bulk (dilatational) viscous isotropic contributions, the third term the deviatoric stress, and μ_b the bulk viscosity. We consider the Zener constitutive model that is suited for materials exhibiting elasticity, viscosity, and stress relaxation. We consider elasticity in the infinitesimally small-strain limit such that the stress and its rate depend linearly on the strain and its rate, (Zener, 1947):

$$\lambda_r \dot{\tau}^{(d)}_{ij} + \tau^{(d)}_{ij} = 2\mu_s \dot{\epsilon}^{(d)}_{ij} + 2G\epsilon^{(d)}_{ij}, \tag{3.8}$$

where the viscous contribution is $\tau^{(v)}_{ij} = 2\mu_s \dot{\epsilon}^{(d)}_{ij}$, the elastic contribution $\tau^{(e)}_{ij} = 2G\epsilon^{(d)}_{ij}$, λ_r the relaxation time, μ_s the shear viscosity, and G the shear modulus. The elastic energy is defined as

$$\rho e^{(e)} = \frac{\tau^{(e)}_{ij}\tau^{(e)}_{ij}}{4G}. \tag{3.9}$$

Moreover, the Zener model has the advantage of reducing to other simple linear constitutive relations (Carcione, 2014; Fung, 1993; Wineman, 2000). We can generalize the Zener model to account for multiple relaxation frequencies. To do so, a shear relaxation function is defined as Carcione (2014)

$$\psi = G_r \left(1 + \sum_{l=1}^{N_r} \varsigma^{(l)} \exp(-\theta^{(l)} t) \right) H(t), \tag{3.10}$$

where G_r is the relaxed shear modulus, $\varsigma^{(l)}$ the relaxation shear coefficient corresponding to relaxation frequency $\theta^{(l)}$, N_r the total number of relaxation frequencies and $H(t)$ the Heaviside function. The elastic stress is a convolution of the shear relaxation function and (deviatoric) strain rate,

$$\tau_{ij}^{(d)} = 2\psi(t) * \epsilon_{ij}^{(d)}. \tag{3.11}$$

Taking an objective Lie temporal derivative and introducing evolution equations of the memory variables close the system.

3.4 Numerical Model

3.4.1 Zener Model in an Eulerian Framework

The main challenge with incorporating elasticity into a shock-capturing framework lies in the representation of deformations, or strains. An objective temporal derivative of the elastic contribution of the deviatoric stress is taken to transform strains into strain rates. The Lie derivative is used to make this transformation (Altmeyer *et al.*, 2015; Rodriguez & Johnsen, 2018),

$$\dot{\tau}_{ij}^{(e)} = \frac{\partial \tau_{ij}^{(e)}}{\partial t} + u_k \frac{\partial \tau_{ij}^{(e)}}{\partial x_k} - \tau_{kj}^{(e)} \frac{\partial u_i}{\partial x_k} - \tau_{ik}^{(e)} \frac{\partial u_j}{\partial x_k} + \tau_{ij}^{(e)} \frac{\partial u_k}{\partial x_k}, \tag{3.12}$$

where the first two terms are the material derivative of the stress tensor and the rest of the terms contribute to preserving objectivity. Here, we incorporate the material derivative and Eq. (4.1a) into the Lie derivative to transport elastic stress tensor and memory variable discontinuities, which

yields (Rodriguez & Johnsen, 2018):

$$\frac{\partial}{\partial t}\left(\rho\tau_{ij}^{(e)}\right)+\frac{\partial}{\partial x_j}\left(\rho\tau_{ij}^{(e)}u_j\right)=\rho\left[2G\dot{\epsilon}_{ij}^{(d)}+\sum_{l}^{N_r}\xi_{ij}^{(l)}\right]+\rho\left[\tau_{kj}^{(e)}\frac{\partial u_i}{\partial x_k}+\tau_{ik}^{(e)}\frac{\partial u_j}{\partial x_k}-\tau_{ij}^{(e)}\frac{\partial u_k}{\partial x_k}\right], \tag{3.13a}$$

$$\frac{\partial}{\partial t}\left(\rho\xi_{ij}^{(l)}\right)+\frac{\partial}{\partial x_j}\left(\rho\xi_{ij}^{(l)}u_j\right)=\rho\left[\xi_{kj}^{(l)}\frac{\partial u_i}{\partial x_k}+\xi_{ik}^{(l)}\frac{\partial u_j}{\partial x_k}-\xi_{ij}^{(l)}\frac{\partial u_k}{\partial x_k}\right]-\rho\left[\theta^{(l)}\left(2\varsigma^{(l)}G_r\dot{\epsilon}_{ij}^{(d)}+\xi_{ij}^{(l)}\right)\right], \tag{3.13b}$$

where $l=1,...,N_r$, $\xi_{ij}^{(l)}$ is the lth memory variable,

$$\xi_{ij}^{(l)}=-\theta^{(l)}G_r\varsigma^{(l)}\exp(-\theta^{(l)}t)H(t)\star\dot{\epsilon}_{ij}^{(d)}, \tag{3.14}$$

N_r the total number of relaxation frequencies corresponding to N_r memory variables and evolution equations, and G_r the relaxed shear modulus,

$$G=G_r\left(1+\sum_{l=1}^{N_r}\varsigma^{(l)}\right), \tag{3.15}$$

where $\varsigma^{(l)}$ are the relaxation coefficients for the given material, which can be obtained by material characterization (Lombard & Piraux, 2011). The memory variable evolution equations close the system without having to perform the temporal convolution in Eq. (3.14).

Using the Lie derivative, the generalized Zener model equations are Eqs. (4.1a), (4.6a), (3.13) and the momentum and energy balance equations,

$$\frac{\partial}{\partial t}(\rho u_i)+\frac{\partial}{\partial x_j}(\rho u_i u_j+p\delta_{ij}-\tau_{ij}^{(e)})=\frac{\partial}{\partial x_j}\left(\tau_{ij}^{(v)}+\mu_b\dot{\epsilon}_{kk}\delta_{ij}\right), \tag{3.16a}$$

$$\frac{\partial E}{\partial t}+\frac{\partial}{\partial x_j}[(E+p)u_j-\tau_{ij}^{(e)}u_i]=\frac{\partial}{\partial x_j}\left[u_i\left(\tau_{ij}^{(v)}+\mu_b\dot{\epsilon}_{kk}\delta_{ij}\right)\right]+\frac{\partial}{\partial x_j}\left(\kappa\frac{\partial T}{\partial x_j}\right). \tag{3.16b}$$

3.4.2 Multi-Material Framework

To represent different materials, we use the five-equation compressible multiphase model (Allaire *et al.*, 2002; Murrone & Guillard, 2005; Alahyari Beig & Johnsen, 2015) for gases, liquids, and solids (Rodriguez & Johnsen, 2018). All materials are assumed to obey the same equation of state and constitutive relation, but with different properties. The numerical dissipation at interfaces gives rise to a (numerical) mixture region of ~4-5 computational cells in which appropriate rules must be specified to prevent spurious errors. In addition to the total mass conservation equation (4.1a), $K-1$ species conservation equations are solved in both conservative form as in Eq. (4.6a) and in non-conservative form to maintain interfacial equilibrium conditions for velocity, pressure and temperature (Alahyari Beig & Johnsen, 2015),

$$\frac{\partial \alpha^{(k)}}{\partial t} + u_j \frac{\partial \alpha^{(k)}}{\partial x_j} = \Gamma^{(k)} \frac{\partial u_j}{\partial x_j}, \tag{3.17}$$

where $k = 1, ..., K-1$ and

$$\Gamma^{(k)} = \frac{\alpha^{(k)}}{K_s^{(k)}} \left(\frac{1}{\sum_l \frac{\alpha^{(l)}}{K_s^{(l)}}} - K_s^{(k)} \right), \tag{3.18}$$

$$K_s^{(k)} = \rho^{(k)} (a^{(k)})^2 = \frac{n^{(k)} (p + B^{(k)})}{(1 - \rho^{(k)} b^{(k)})}. \tag{3.19}$$

Though necessary to represent compressible multiphase problems with significant dilatational effects, the right-hand-side of this equation is sometimes set to zero (Allaire *et al.*, 2002; Perigaud & Saurel, 2005; Shukla *et al.*, 2010). In this chapter, we assume dilatational effects are such that the right-hand-side is negligible and thus neglect these terms. When using AUSM$^+$-up with the source terms, the system became considerably stiffer; future studies will investigate how to incorporate this term in this framework.

The pressure and temperature are computed based on the internal energy as follows:

$$p = \frac{E - \rho\frac{u_i^2}{2} - \rho e^{(e)} - \sum_k \rho^{(k)}\alpha^{(k)}q^{(k)} - \sum_k \alpha^{(k)}\frac{n^{(k)}B^{(k)}(1-\rho^{(k)}b^{(k)})}{n^{(k)}-1}}{\sum_k \alpha^{(k)}\frac{1}{n^{(k)}-1}}, \tag{3.20a}$$

$$T = \frac{E - \rho\frac{u_i^2}{2} - \rho e^{(e)} - \sum_k \rho^{(k)}\alpha^{(k)}q^{(k)} - \sum_k \alpha^{(k)}(1-\rho^{(k)}b^{(k)})B^{(k)}}{\sum_k \rho^{(k)}\alpha^{(k)}c^{(k)}}, \tag{3.20b}$$

where terms with $\rho^{(k)}\alpha^{(k)}$ are calculated using Eq. (4.6a), terms with $\alpha^{(k)}$ only are calculated using Eq. (4.6b), as described in Alahyari Beig & Johnsen (2015). The internal energy can be calculated by rearranging Eq. (3.20). Mixture material properties ϕ (e.g., elastic moduli, viscosities, thermal conductivity, etc.) are weighted by the volume fraction:

$$\phi = \sum_k \alpha^{(k)}\phi^{(k)}. \tag{3.21}$$

The spatial gradients of $\alpha^{(k)}$ are computed to obtain the spatial gradients of ϕ.

3.5 Numerical Method

3.5.1 Baseline Temporal and Spatial Schemes

We use the standard explicit fourth-order Runge-Kutta scheme for time marching. Accounting for advection and diffusion, the minimum time step is computed:

$$\Delta t = \min\left(\nu\frac{\Delta x}{\zeta_{max}}, \nu_\mu\frac{\Delta x^2}{(\mu_s/\rho)}, \nu_\kappa\frac{\Delta x^2}{(\kappa/\rho c)}\right), \tag{3.22}$$

where Δx is the mesh size, ζ_{max} the maximum global wave speed, ν is the Courant number, ν_μ and ν_r are the Von Neumann numbers for viscous and thermal diffusion. Unless stated otherwise, we set $\nu = 0.75$ and $\nu_\mu = \nu_\kappa = 0.125$. The maximum wave speed is calculated using the maximum

eigenspeed and incorporating the effect of linear viscoelasticity (Rodriguez & Johnsen, 2018):

$$\zeta_{max} = \max_j \left(|u| \pm \sqrt{\frac{n(p+B)}{\rho(1-\rho b)} + \frac{4G/3 + \tau_{jj}^{(e)}}{\rho}} \right)_j .$$

The spatial discretization is based on a solution-adaptive approach that introduces numerical dissipation only where necessary. The discontinuity sensor of Henry de Frahan *et al.* (2015); Alahyari Beig & Johnsen (2015); Rodriguez & Johnsen (2018) detects shocks, contact discontinuities and material interfaces, such that the convective fluxes are computed as follows:

$$F_{i\pm1/2} = \begin{cases} F_{i\pm1/2}|_{AUSM^+-up}, & \text{if } \Phi_A > 10^{-4} \forall A \\ F_{i\pm1/2}|_{central}, & \text{otherwise,} \end{cases} \tag{3.23}$$

where the subscripts "central" and "AUSM$^+$-up" are explained below, and

$$\Phi_A = \frac{4\phi_A}{(1+\phi_A)^2}, \qquad \phi_A = \frac{|A_R - A_L|}{A_R + A_L}, \tag{3.24}$$

where A is p, ρ or n, and L and R denote the left and right edge of a computational cell. If $\Phi_A > 10^{-4}$ $\forall A$ in a given cell, the solution is considered discontinuous and the WENO approach of Johnsen & Colonius (2006) is used for all the primitive variables along with AUSM$^+$-up (Chang & Liou, 2007) generalized to viscoelasticity in the context of the five-equation multiphase model. The sensor is not activated for smooth problems, i.e., central differences are used exclusively in such problems. If discontinuities are detected, shock/interface capturing is applied. Though the capturing scheme is second-order, it does not affect the overall convergence rate, since problems with discontinuities exhibit first-order convergence only. Derivatives in the diffusion and source terms and material properties are computed using explicit fourth-order central differences.

3.5.2 Implementation of the AUSM$^+$-up Scheme for the Compressible, Zener Model

AUSM schemes were extended to solve the compressible Navier-Stokes equations for multiphase flows (Chang & Liou, 2003; Paillère *et al.*, 2003; Chang & Liou, 2007; Liou *et al.*, 2008). The constitutive relation for Cauchy stress tensor is $\sigma_{ij} = -p\delta_{ij} + \mu_b \dot{\epsilon}_{kk}\delta_{ij} + \tau_{ij}^{(v)}$, for Newtonian fluids. AUSM schemes split the flux into *convective* and *pressure* flux contributions (Liou, 1996), with the viscous terms computed separately. We first generalize the AUSM$^+$-up flux-vector splitting to solve the numerical model with a general Cauchy stress tensor; we then extend this procedure to the generalized Zener model. For brevity, the extension of AUSM$^+$-up for all-speeds is not presented, but can be obtained in a straightforward fashion following (Liou, 2006). We start by formulating the AUSM flux-vector splitting to Eqs. (4.1) using the U-splitting form (Liou, 1992) for a Cauchy stress tensor described by linear viscoelasticity,

$$F_{k,i+1/2} = \max(u_{k,i+1/2}, 0)\varphi_L + \min(u_{k,i+1/2}, 0)\varphi_R + \max(u_{l,i+1/2}, 0)\psi_L + \min(u_{l,i+1/2}, 0)\psi_R + \eta_{i+1/2}, \tag{3.25}$$

where $k \neq l$, the first subscript denotes the flux vector direction, and the second the discretization index. The subscripts $L,\ R$ indicate the left and right edge of the computational cell, respectively, whose values are calculated using WENO reconstruction on the primitive variables (Johnsen & Colonius, 2006). To account for the second term in the convective flux in Eq. (3.16b), an additional convective flux vector, ψ, is needed alongside the conventional convective flux vector in AUSM$^+$-up, and the pressure flux is generalized to the Cauchy stress tensor flux,

$$\varphi = \begin{bmatrix} \rho \\ \rho u_l \\ E - \sigma_{kk} \\ \rho^{(k)}\alpha^{(k)} \end{bmatrix}, \quad \psi = \begin{bmatrix} 0 \\ 0 \\ \sigma_{kl} \\ 0 \end{bmatrix}, \quad \eta = \begin{bmatrix} 0 \\ -\sigma_{kl} \\ 0 \\ 0 \end{bmatrix}, \tag{3.26}$$

where $k \neq l$. The velocities $u_{k,i+1/2}$ and $u_{l,i+1/2}$ are computed using the AUSM$^+$-up Mach number splitting (Chang & Liou, 2007),

$$u_{k,i+1/2} = a_{1/2}(\mathcal{M}^+_{(4)}(M_L) + \mathcal{M}^-_{(4)}(M_R)) + \kappa_p \max(1 - \bar{M}^2, 0)\frac{(\sigma_L - \sigma_R)}{\rho_{1/2} a_{1/2}}, \tag{3.27a}$$

$$u_{l,i+1/2} = a_{1/2}(\mathcal{M}^+_{(4)}(N_L) + \mathcal{M}^-_{(4)}(N_R)), \tag{3.27b}$$

where the subscripts of $\mathcal{M}$ are the order of the polynomial used, the left and right Mach numbers

$$M_{L/R} = \frac{u_{k,L/R}}{a_{1/2}}, \qquad N_{L/R} = \frac{u_{l,L/R}}{a_{1/2}},$$

the interface values arithmetic averages, e.g., $a_{1/2} = (a_L + a_R)/2$, $\bar{M}^2 = (M_L^2 + M_R^2)/2$, and the coefficient $\kappa_p = 0.4$ unless stated otherwise. The third terms of Eqs. (3.27) and (3.28), are the "up" velocity-stress coupling terms that add the necessary dissipation to handle flows with large density ratios (Chang & Liou, 2003, 2007). The tangent velocity $u_{l,i+1/2}$ and Cauchy stress tensor flux $\eta_{kk,i+1/2}$ in Eqs. (3.27) and (3.28), respectively, are attributed to the elastic shear wave. Since the shear wave is not significantly affected by the large density gradients relative to their normal stress wave counterparts, these terms are computed without the "up"-dissipation terms. The split Mach number functions are defined,

$$\mathcal{M}^\pm_{(4)} = \begin{cases} \mathcal{M}^\pm_{(1)}, & \text{if} \quad |M| \geq 1, \\ \mathcal{M}^\pm_{(2)}\left[1 \mp 2\mathcal{M}^\mp_{(2)}\right], & \text{otherwise}, \end{cases}$$

$$\mathcal{M}^\pm_{(1)} = \frac{M \pm |M|}{2}, \quad \mathcal{M}^\pm_{(2)} = \pm\frac{(M \pm 1)^2}{4}.$$

The Cauchy stress tensor flux, $\eta_{i+1/2}$, is defined using the same approach as the AUSM$^+$-up pressure flux,

$$\eta_{kk,i+1/2} = \mathcal{P}^+_{(5)}(M_L)\sigma_{kk,L} + \mathcal{P}^-_{(5)}(M_R)\sigma_{kk,R} + \kappa_u \mathcal{P}^+_{(5)}(M_L)\mathcal{P}^-_{(5)}(M_R)\rho_{1/2}a_{1/2}(u_L - u_R), \tag{3.28a}$$

$$\eta_{kl,i+1/2} = \mathcal{P}^+_{(5)}(M_L)\sigma_{kl,L} + \mathcal{P}^-_{(5)}(M_R)\sigma_{kl,R}, \tag{3.28b}$$

where $k \neq l$,

$$\mathcal{P}^{\pm}_{(5)} = \begin{cases} \mathcal{M}^{\pm}_{(1)}/M, & \text{if} \quad |M| \geq 1, \\ \mathcal{M}^{\pm}_{(2)}\left[\pm 2 - M \mp 3M\mathcal{M}^{\mp}_{(2)}\right], & \text{otherwise,} \end{cases}$$

$\bar{M} = (M_L + M_R)/2$, and the coefficient $\kappa_u = 0.2$ unless stated otherwise. We follow (Chang & Liou, 2003, 2007) when specifying the AUSM$^+$ scheme's tunable parameters for multiphase problems and set $\alpha = 3/16$ and $\beta = 1/8$, see Liou (2006) for further details on these parameters. In other AUSM schemes (Chang & Liou, 2003, 2007; Liou *et al.*, 2008; Kitamura *et al.*, 2014), the κ_u and κ_p coefficients are set to unity to increase the scheme's dissipation and decrease the numerical stiffness. Additionally, when $\sigma_{kl} = -p\delta_{kl}$, the numerical method reverts to AUSM$^+$-up for the Euler equations and the additional convective flux vector, ψ, is not computed. Using this formulation, the x-direction AUSM$^+$-up flux vectors for the 2D generalized Zener numerical model are:

$$\phi = \begin{bmatrix} \rho \\ \rho u \\ \rho v \\ E - \sigma_{11} \\ \rho\alpha^{(k)} \\ \rho\tau^{(e)}_{ij} \\ \rho\xi^{(l)}_{ij} \end{bmatrix}, \quad \psi = \begin{bmatrix} 0 \\ 0 \\ 0 \\ -\tau^{(e)}_{12} \\ 0 \\ 0 \\ 0 \end{bmatrix}, \quad \eta = \begin{bmatrix} 0 \\ -\sigma_{11} \\ -\tau^{(e)}_{12} \\ 0 \\ 0 \\ 0 \\ 0 \end{bmatrix},$$

where $\sigma_{11} = -p + \tau^{(e)}_{11}$ and indices $i, j = 1$ and 2. Following appropriate simplifications, the flux vectors for the generalized Zener numerical model reduces to simpler models (e.g., Kelvin-Voigt,

Maxwell, Newtonian).

3.5.3 Verification of the Proposed AUSM$^+$-up Approach to the Advection of a Material Interface

The non-conservative equation for the volume fraction in the multi-material framework must be carefully discretized using AUSM$^+$-up to prevent spurious errors and maintain equilibrium conditions for initially uniform flows. Following Saurel & Abgrall (1999b); Johnsen & Colonius (2006); Alahyari Beig & Johnsen (2015), we aim to consistently solve the numerical model using AUSM$^+$-up with minimal modifications to the overall method. We begin by prescribing that interfacial conditions must be maintained for a flow initialized in equilibrium, i.e.,

$$u^{n+1} = u^n = u, \quad p^{n+1} = p^n = p, \quad T^{n+1} = T^n = T,$$

where the superscripts denote the time step. Since the source terms, elastic stresses and memory variables depend on velocity spatial gradients, which are zero in equilibrium, those relevant terms cancel out. Only the spatial gradients in the volume fraction and density remain. As part of the analysis, the AUSM$^+$-up operator under equilibrium conditions is first identified to determine the necessary evolution equation for the non-conservative volume fraction equation to maintain interfacial equilibrium conditions.

Applying Eq. (3.25) to the mass conservation equation, Eq. (4.1a), and considering a simple time discretization yields the AUSM$^+$-up discretization operator $\mathcal{A}(\cdot)$ such that

$$\rho_i^{n+1} = \rho_i^n - (\Delta t/\Delta x)\mathcal{A}(\rho), \tag{3.29}$$

where

$$\mathcal{A}(\rho) = \left(\max(u_i^n, 0)\rho_{i+1/2,L}^n + \min(u_i^n, 0)\rho_{i+1/2,R}^n\right) - \left(\max(u_i^n, 0)\rho_{i-1/2,L}^n + \min(u_i^n, 0)\rho_{i-1/2,R}^n\right). \tag{3.30}$$

Discretizing the momentum balance equation, the pressure terms cancel, thus yielding the mass conservation equation if and only if $u^{n+1} = u^n$. For the energy balance equation, we let $b = 0$ in the NASG EOS. Applying equilibrium conditions yields

$$(\rho e)_i^{n+1} = (\rho e)_i^n - (\Delta t/\Delta x)\mathcal{A}(\rho e). \tag{3.31}$$

The kinetic energy contribution in the total energy results in a result similar to Eq. (4.1a). The elastic energy contribution to the total energy also cancels out. Applying the pressure- and temperature-wise forms of the EOS for the internal energy, i.e., Eqs. (4.8), we obtain

$$(\mathcal{X}p + \chi)_i^{n+1} = (\mathcal{X}p + \chi)_i^n - (\Delta t/\Delta x)\mathcal{A}(\mathcal{X}p + \chi), \tag{3.32}$$

where

$$\mathcal{X} = \sum \frac{\alpha^{(k)}}{n^{(k)} - 1}, \quad \chi = \sum \frac{\alpha^{(k)} n^{(k)} B^{(k)}}{n^{(k)} - 1},$$

for the pressure-wise form, and

$$(\Theta T + \theta)_i^{n+1} = (\Theta T + \theta)_i^n - \mathcal{A}(\Theta T + \theta), \tag{3.33}$$

where

$$\Theta = \sum_k \rho^{(k)} c^{(k)} \alpha^{(k)}, \quad \theta = \sum_k B^{(k)} \alpha^{(k)},$$

for the temperature-wise form. Eqs. (3.32) and (3.33) are rearranged and one equation for α is obtained to maintain pressure and temperature equilibrium,

$$(\alpha)_i^{n+1} = (\alpha)_i^n - (\Delta t/\Delta x)\mathcal{A}(\alpha). \tag{3.34}$$

This is a numerical discretization of non-conservative the linear advection of α,

$$\frac{\partial \alpha^{(k)}}{\partial t} + u\frac{\partial \alpha^{(k)}}{\partial x} = 0. \tag{3.35}$$

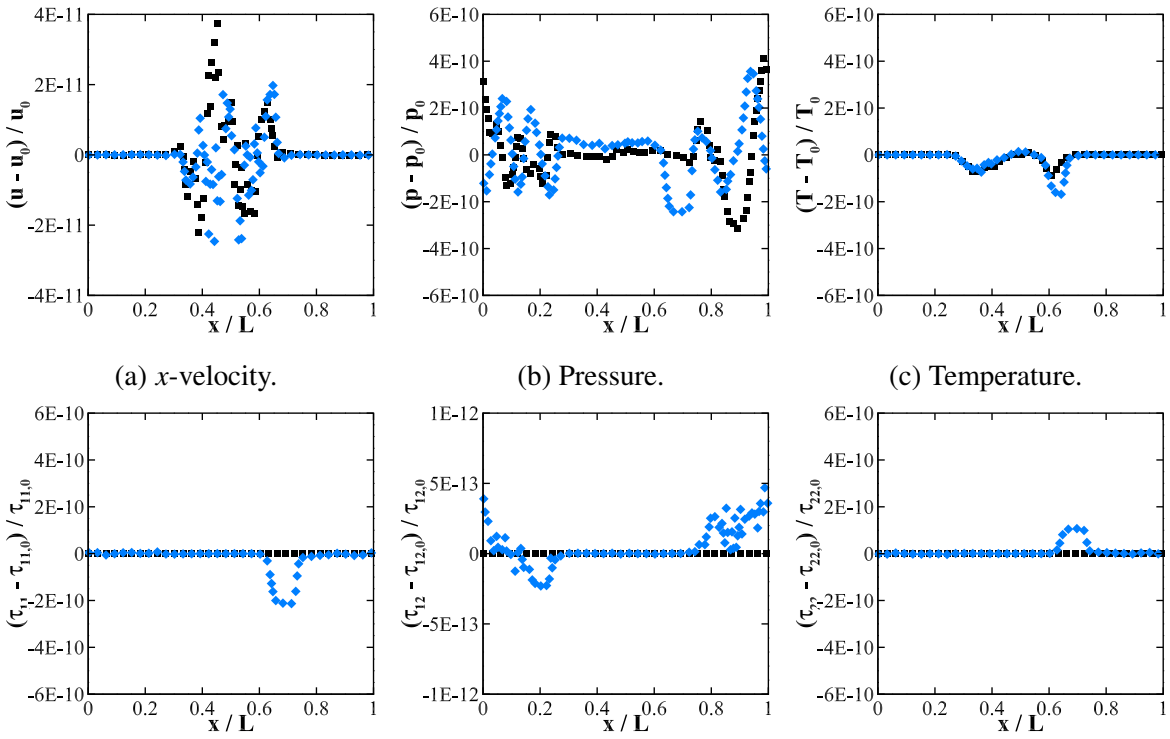

(a) x-velocity. (b) Pressure. (c) Temperature.

(d) Elastic stress $\tau_{11}^{(e)}$. (e) Elastic stress $\tau_{12}^{(e)}$. (f) Elastic stress $\tau_{22}^{(e)}$.

Figure 3.1: Relative error in the interface advection problem after ten periods. Black squares: Newtonian liquid ($G = 0$); blue diamonds: $G = 100$ MPa.

We note that the source term in Eq. (4.6b) would cancel out since the velocity is constant initially. Quantities $\mathcal{X}, \chi, \Theta$, and θ must be computed as described above when solving for p and T to prevent spurious errors (Alahyari Beig & Johnsen, 2015; Rodriguez & Johnsen, 2018).

3.6 Results

We demonstrate our proposed approach by solving 1D and 2D multi-material problems with shocks. Using 1D problems, we demonstrate the framework's ability to maintain equilibrium conditions and resolve the wave structures. We solve 2D shock-cylinder interaction problems in which the cylinder is made of, alternatively, gas, water, and a Zener solid.

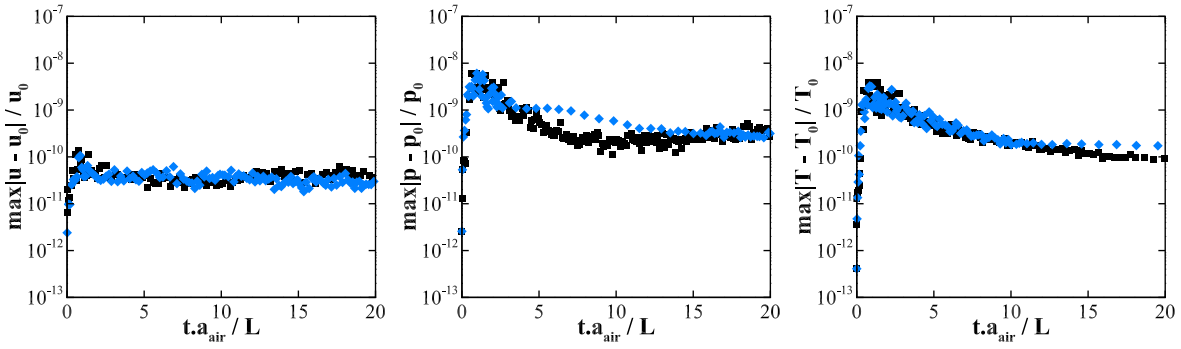

(a) x-velocity. (b) Pressure. (c) Temperature.

Figure 3.2: Time histories of normalized L_∞ errors for the interface advection problem through ten periods. Black squares: Newtonian medium; blue diamonds: viscoelastic medium ($\mu_b = \mu_s = 5$ mPa s, $G = 100$ MPa, $G_r = 50$ MPa).

3.6.1 Material Interface Advection Problem

We demonstrate that the five-equation framework for the AUSM$^+$-up scheme presented in §3.5.3 maintains equilibrium conditions at interfaces (Abgrall, 1996; Shyue, 1998; Johnsen, 2011; Allahyari Beig & Johnsen, 2015; Rodriguez & Johnsen, 2018). We consider the 1D multi-material interface problem of our previous work (Rodriguez & Johnsen, 2018) with the Zener model for the viscoelastic medium and the material properties in Table 6.1. The initial conditions are

$$(\rho, u, v, p) = \begin{cases} (1, 0.5, 0.5, 1/\gamma), \text{if } x/L \in [0.25, 0.75] \\ (1000, 0.5, 0.5, 1/\gamma), \text{otherwise,} \end{cases} \tag{3.36}$$

with $\tau_{11}^{(e)} = \tau_{22}^{(e)} = \tau_{12}^{(e)} = \xi_{11}^{(1)} = \xi_{22}^{(1)} = \xi_{12}^{(1)} = 0$ and $n = 1.4$ for air. For the model viscoelastic material, $\mu_b = \mu_s = 5$ mPa s, $G = 100$ MPa, $G_r = 50$ MPa, $\varsigma^{(1)} = 1$ and $\theta^{(1)} = 100$ MHz. For air, $\kappa = 0.026$ W/(K m), and for the model viscoelastic material, $\kappa = 0.615$ W/(K m). The domain is periodic with $L = 1$ mm, $x \in [0, 1]$, and $N = 200$. The normalized errors in x-velocity, pressure, temperature and elastic components of the Cauchy stress tensor after the solution has traveled ten domain lengths are plotted in Fig. 3.1. At the final time, all the errors are below 4×10^{-10}. The normalized elastic stress errors for $\tau_{11}^{(e)}$ and $\tau_{22}^{(e)}$ are localized at the right interface, i.e., $x/L = 0.75$, due to the

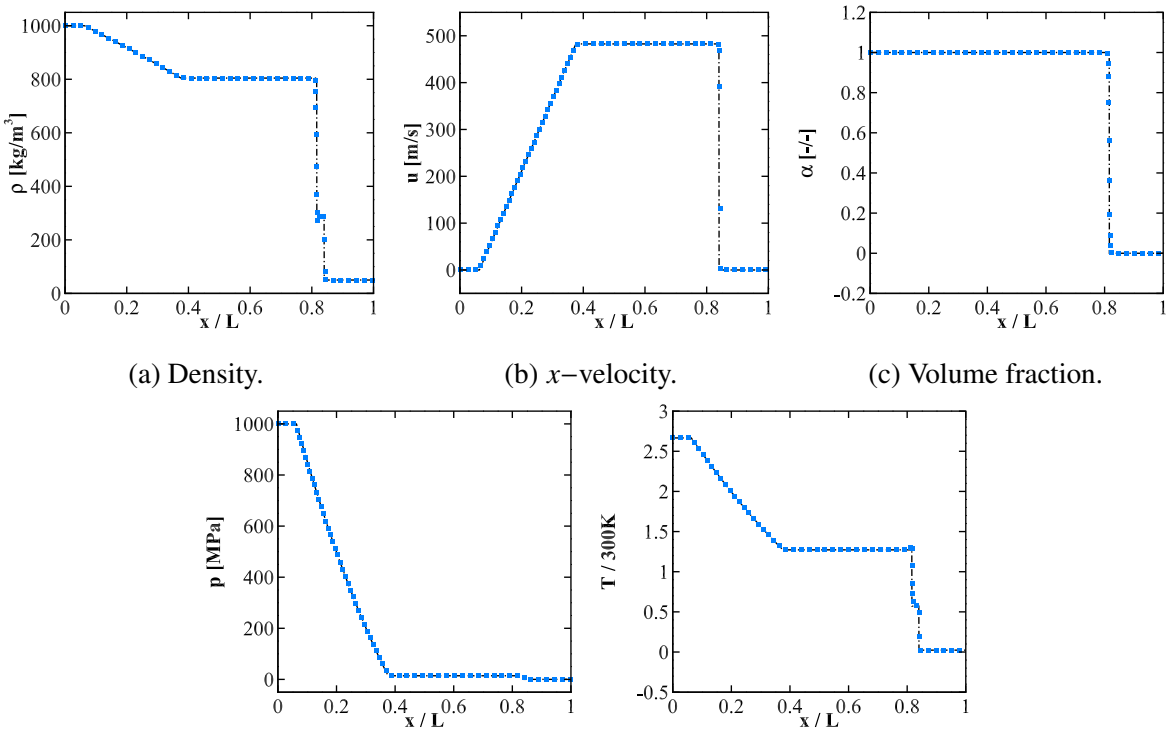

(a) Density. (b) $x-$velocity. (c) Volume fraction.

(d) Pressure. (e) Temperature.

Figure 3.3: Multi-material Riemann problem at $t = 240\ \mu$s with analytical (black dashed line) and numerical (blue square) solutions for the viscous liquid-air shock wave interaction.

advection speed. The time histories of the normalized x-velocity, pressure, and temperature errors are plotted in Fig. 3.2. Within the first two periods of the simulation, the normalized temperature errors quickly rise to 10^{-8}. The temperature profile modifies the pressure through the heat transfer term such that discrepancies in pressure grow to a similar order of magnitude. For an isothermal simulation (results not shown), the normalized pressure errors do not exhibit this rise and remain bounded below 5×10^{-10}. After five periods, both temperature and pressure errors decrease by two orders of magnitude to 10^{-10}. The x-velocity errors remain bounded below 6×10^{-11}. The y-velocity and the elastic stress errors are negligible (data not shown). We conclude that our multi-material framework utilizing AUSM$^+$-up is capable of maintaining equilibrium conditions and prevent spurious interfacial errors.

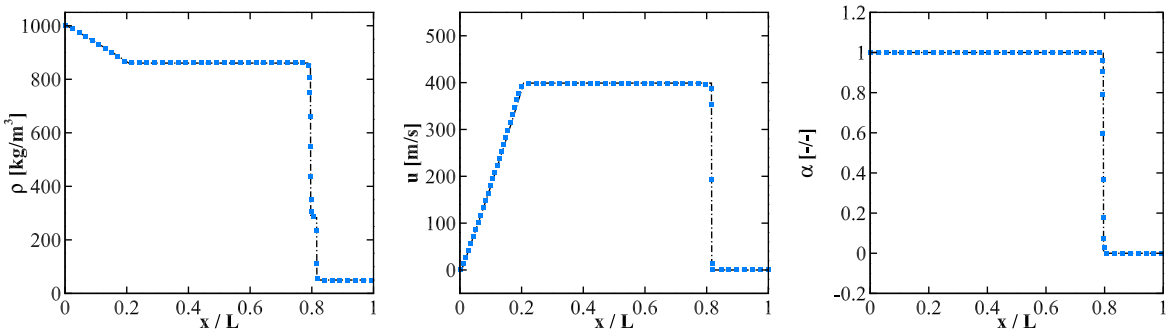

(a) Density. (b) $x-$velocity. (c) Volume fraction.

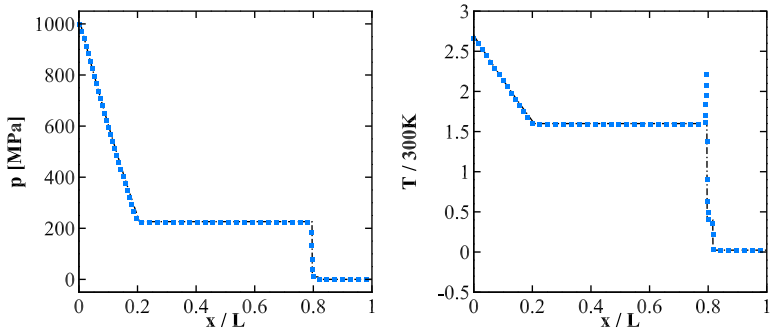

(d) Pressure. (e) Temperature.

Figure 3.4: Multi-material Riemann problem at $t = 240$ μs with analytical (black dashed line) and numerical (blue square) solutions for the Kelvin-Voigt viscoelastic material-air shock wave interaction.

3.6.2 Multi-material Riemann Problem

We verify the extension of the five-equation multiphase model to viscoelastic media with shocks by considering the multi-material Riemann problem in (Alahyari Beig & Johnsen, 2015; Murrone & Guillard, 2005; Allaire *et al.*, 2002) with viscoelasticity (Rodriguez & Johnsen, 2018),

$$(\rho, p, \alpha^{(1)}) = \begin{cases} (1000, 10^9, 1) & \text{if } x/L \in [0, 0.7], \\ (50, 10^5, 0) & \text{otherwise}, \end{cases} \tag{3.37}$$

with $u = v = 0$ and $L = 1$ mm. The initial elastic stresses are $\tau_{11}^{(e)} = \tau_{22}^{(e)} = \tau_{12}^{(e)} = 0$. For the model viscoelastic material, $\kappa = 0.615$ W/(K m) and for the gas, $\kappa = 0.026$ W/(K m). The viscous ($\mu_b = \mu_s = 50$ mPa s) and Kelvin-Voigt ($\mu = 50$ mPa s and $G = 1$ GPa) solutions are

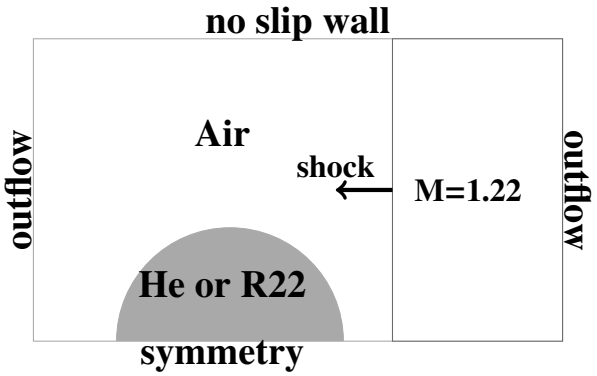

Figure 3.5: Shock-gas cylinder interaction problem setup.

plotted at $t = 240$ μs in Figs. 3.3 and 3.4 along with their respective analytical solutions. The analytical solutions are generated using the Riemann solver of Gavrilyuk *et al.* (2008), in which ρG is assumed constant for the analytical viscoelastic solution. The numerical results show good agreement with the analytical solution since the density and pressure ratios are large. We note that all the relevant waves are captured. A spurious over-heating spike is observed in the temperature plot at the material interface for the Kelvin-Voigt solution. This spike has also been observed for multi-material problems and can be addressed with the fix by Fedkiw *et al.* (1999).

3.6.3 2D Shock-Gas Cylinder Interaction Problems

We demonstrate the numerical framework's ability to handle 2D multifluid problems by studying shock-gas cylinder interaction problems. We compute the problem studied experimentally by Haas and Sturtevant (Haas & Sturtevant, 1987) and simulated numerically by Quirk & Karni (1996). The initial set-up is shown in Fig. 3.5; given the symmetry of the problem half of the domain is simulated. The initial cylinder radius is 25 mm. The computational domain extends six initial bubble radii in the x-direction from the bubble center, with $x \in$[-150 mm, 150 mm] and $y \in$[0 mm, 44.5 mm]. The resolution is 256 points per initial cylinder radius. We define the initial cylinder radius with a diffuse interface whose volume fraction is $\alpha = \frac{1-\tanh(\varrho)}{2}$, where $\varrho = (R - R_o)/\Delta x$, $R = \sqrt{x^2 + y^2}$ and $R_o = 25$ mm is the initial cylinder radius. With volume fraction defined and known velocity and pressure initial conditions throughout the domain, the conservative variables ϕ

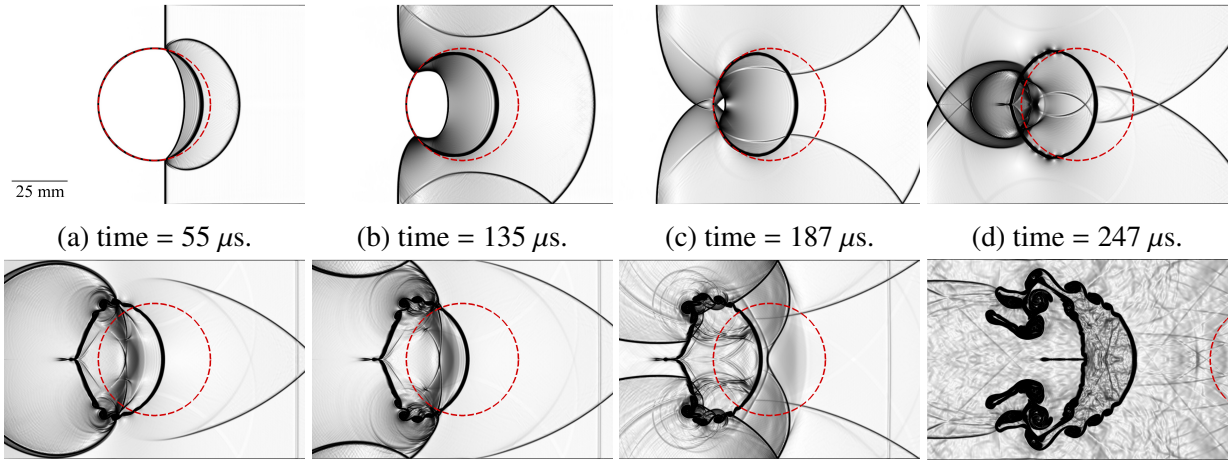

(a) time = 55 μs. (b) time = 135 μs. (c) time = 187 μs. (d) time = 247 μs.

(e) time = 318 μs. (f) time = 342 μs. (g) time = 647 μs. (h) time = 1020 μs.

Figure 3.6: Time evolution of numerical Schlieren contours for the shock-R22 gas cylinder interaction problem with a M = 1.22 shock moving from right to left. The red dotted outline denotes the cylinder's initial location.

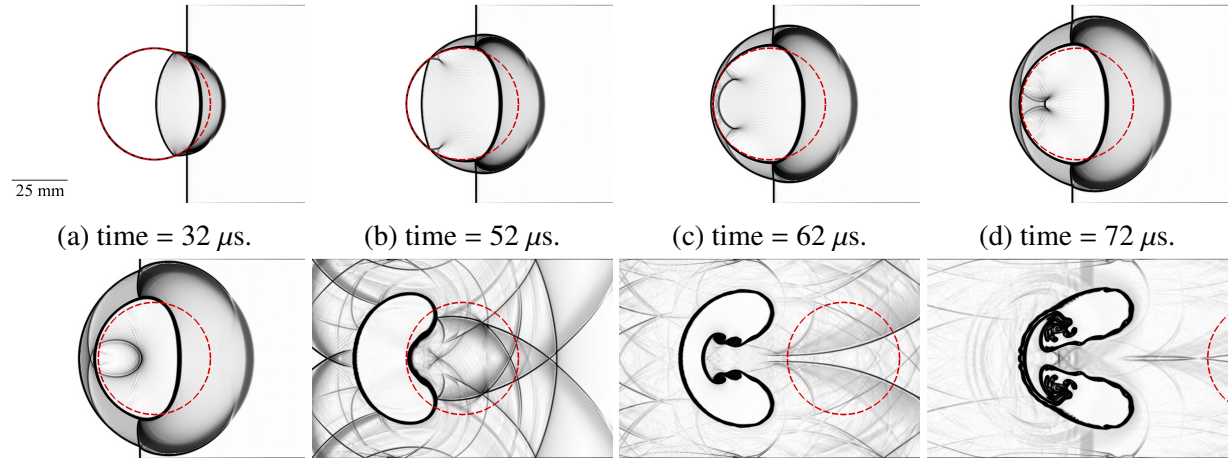

(a) time = 32 μs. (b) time = 52 μs. (c) time = 62 μs. (d) time = 72 μs.

(e) time = 82 μs. (f) time = 245 μs. (g) time = 427 μs. (h) time = 674 μs.

Figure 3.7: Time evolution of numerical Schlieren contours for the shock-helium gas cylinder interaction problem with a M = 1.22 shock moving from right to left. The red dotted outline denotes the cylinder's initial location.

are computed using the mixture relation, $\phi = \alpha^{(1)}\phi_1 + (1 - \alpha^{(1)})\phi_2$.

We solve the compressible Navier-Stokes equations for the convergent (helium) and divergent (R22) cases utilizing the same initial conditions as the experiment. The surrounding medium is air with $\rho = 1.204$ kg/m^3 and $\kappa = 0.026$ W/(K m) with the remaining material properties listed in Table 6.1. Helium and R22 properties reported by Quirk & Karni (1996) were adapted:

$\rho_{He} = 0.222$ kg/m^3, $\kappa_{He} = 0.151$ W/(K m), $\rho_{R22} = 3.69$ kg/m^3, and $\kappa_{R22} = 0.61$ W/(K m). The shock wave is initialized at $x = 5 \times R_0$, using the Rankine-Hugoniot conditions for a $M = 1.22$ normal shock propagating from right to left. No-penetration and no-slip boundary conditions are set along the top wall.

Select contours of the nonlinear shading function from Quirk & Karni (1996) are shown for the R22 and helium cases in Figs. 3.6 and 3.7, respectively. The times shown correspond to those reported by Haas & Sturtevant (1987); Quirk & Karni (1996). To obtain comparable contours to the experiments, the timings on the contours were taken such that at time $t = 0$ the shock is at $x = 28$ mm from the cylinder center and not yet at the upstream cylinder interface. Haas and Sturtevant (Haas & Sturtevant, 1987) reported an error of 10% in their velocity measurements; thus, the 12% discrepancy in start time to obtain comparable contours is reasonable.

3.6.3.1 R22 gas cylinder.

Upon interacting with the right side of the R22 cylinder, the incoming shock is partially reflected and transmitted (frame a). Since the speed of sound in R22 is smaller than that of air, the transmitted shock propagates more slowly than the shock in air (frame b). Additionally, the reflected shock wave propagates radially and is reflected from the top and bottom walls towards the cylinder. The incident shock intersects along the centerline after interacting with the cylinder (frame c) and the transmitted shock is partially transmitted into the air and partially reflected into the cylinder (frame d). The transmitted shock also forms a central wedge downstream of the R22-air interface comparable with the experiments. As the incident shock traverses the interface, the misalignment of density (material interface) and pressure (shock) gradients deposits baroclinic vorticity along the interface and generates roll-ups. Later, the shock is partially transmitted into the surrounding air and propagates radially interacting with the interface; this shock is also reflected from the walls (frames d-g). The transmitted shock-interface interactions further enhance the roll-ups as the cylinder has convected to the left (frames d-g). The two-pronged feature at the downstream centerline edge of the interface noticeable in the numerical simulations of Quirk & Karni (1996)

is also observed. However, this feature is not as pronounced here. Moreover, fewer and smoother roll-ups develop in the later times (frame g) compared to the heavily corrugated interface in Quirk & Karni (1996). We conclude that our AUSM scheme exhibits good qualitative agreement with experiments.

3.6.3.2 Helium gas cylinder.

Since the impedance of the helium cylinder is lower than that of the surrounding air, the incident shock is partially transmitted as a shock and partially reflected as a rarefaction. Due to the higher speed of sound of the helium with 20% air gas (a_{He} = 872 m/s), the transmitted shock propagates ahead of the incident shock and reaches the downstream cylinder interface (frame a). We obtain good agreement with the flow features observed in Quirk & Karni (1996); Haas & Sturtevant (1987). At t = 52 μs (frame b), the four-shock, twin regular reflection-refraction (TRR) configuration described in Henderson *et al.* (1991) is observed. The transmitted shock then reaches the downstream material interface at t = 62 μs (frame c), is partially reflected and develops into two cusps within the cylinder. These two cusps then converge, coincide, and are reflected outward to form a small hoop (frames d and e). Over time, the magnitude of the shock trapped in the cylinder decreases. Outside of the cylinder, the incident and partially transmitted shocks are reflected from the walls and the material interface (frame f). The baroclinic vorticity deposited along the material interface gives rise to a re-entrant jet as the cylinder convects downstream. Unlike the simulations of Quirk & Karni (1996), the roll-ups along the interface are not observed; the cylinder's morphology in our simulations are in better agreement with the experiments. The re-entrant jet develops while the cylinder takes a kidney shape as the shocks in the surroundings weaken as they leave the domain (frame g). Eventually the upstream and downstream cylinder interfaces meet, such that the cylinder takes the form of two vortex lines symmetric upon the centerline, which convect downstream (frame h). Overall, the agreement between the proposed approach and the experiments is good.

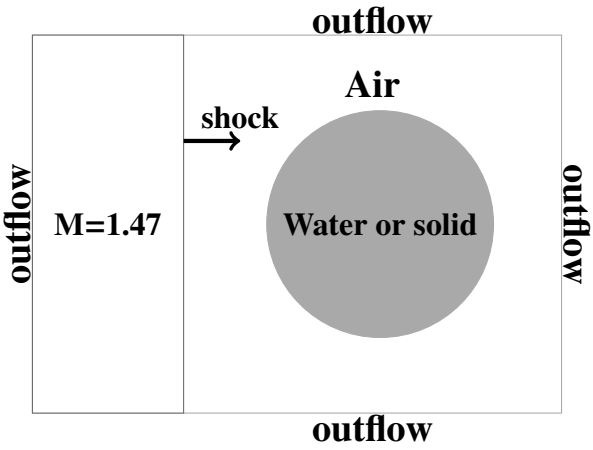

Figure 3.8: Shock-cylinder interaction problem set-up adapted from Chang et al. (Chang & Liou, 2007).

3.6.4 2D Shock-Water/Zener Solid Cylinder Interaction Problems

We study shock-droplet/cylinder interaction problems with density ratios of 1000:1 between the material in the cylinder and the surrounding air. This problem has been studied experimentally (Theofanous *et al.*, 2004) and numerically simulated with the inviscid, compressible Euler equations using FDS schemes in 3D (Meng & Colonius, 2018) and AUSM schemes (Chang & Liou, 2007; Niu *et al.*, 2008; Liou *et al.*, 2008; Kitamura *et al.*, 2014). The shock-water cylinder interaction problem of Kitamura *et al.* (2014) is adapted as shown in Fig. 3.8. The initial cylinder radius is 3.2 mm. The domain extends three initial bubble radii in both directions: $x,\ y \in [-9.6$ mm, 9.6 mm]. The resolution is 128 points per initial cylinder radius. The shock is initialized at $x = -2$ mm, using the Rankine-Hugoniot conditions for a $M = 1.47$ normal shock propagating from left to right. The initial cylinder radius and conservative variables are initialized in the same fashion as in §3.6.3. The Courant number is $\nu = 0.15$ and AUSM$^+$-up velocity-stress coupling coefficients are $k_p = k_u = 1$. Our simulations did not require the variable mixing (blending) procedure (Chang & Liou, 2007; Liou *et al.*, 2008; Kitamura *et al.*, 2014; Pandare & Luo, 2018) where mixing is introduced to prevent the occurrence of non-physical negative pressures and improve numerical stability.

We consider two different materials for the cylinder: water and Zener solid. We seek to eval-

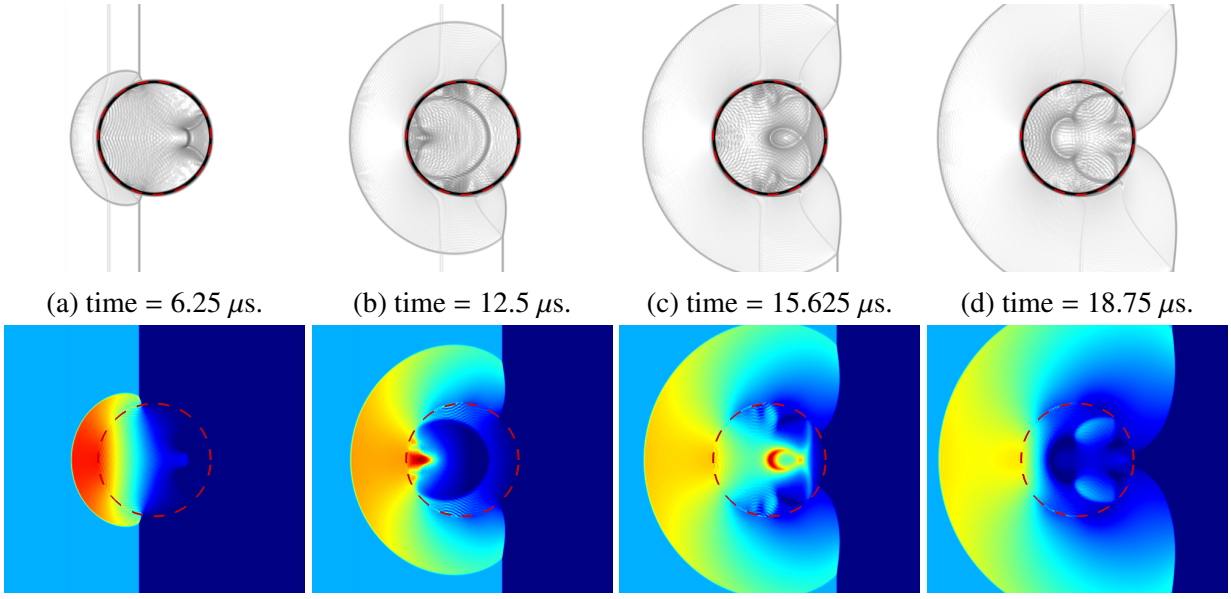

(a) time = 6.25 μs. (b) time = 12.5 μs. (c) time = 15.625 μs. (d) time = 18.75 μs.

(e) time = 6.25 μs. (f) time = 12.5 μs. (g) time = 15.625 μs. (h) time = 18.75 μs.

Figure 3.9: Time evolution of numerical Schlieren (top) and pressure (bottom) contours for the shock-water cylinder interaction problem. The red dotted outline denotes the cylinder's initial location.

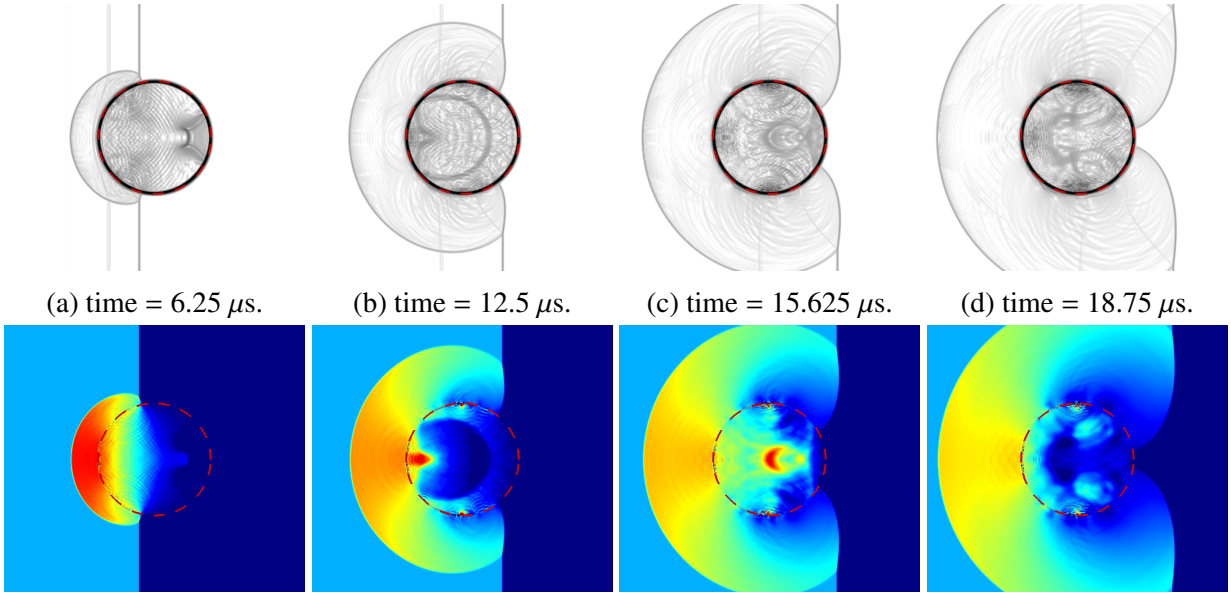

(a) time = 6.25 μs. (b) time = 12.5 μs. (c) time = 15.625 μs. (d) time = 18.75 μs.

(e) time = 6.25 μs. (f) time = 12.5 μs. (g) time = 15.625 μs. (h) time = 18.75 μs.

Figure 3.10: Time evolution of numerical Schlieren (top) and pressure (bottom) contours for the shock-Zener solid cylinder interaction problem. The red dotted outline denotes the cylinder's initial location.

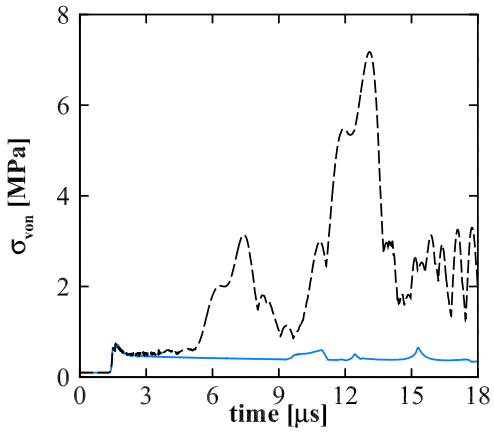

Figure 3.11: Time evolution of the Von Mises stress for the 2D shock-cylinder interaction problem. Blue solid line: water; black dashed line: Zener solid.

uate the effect of the viscoelasticity on the wave dynamics by considering the numerical Schlieren and pressure contours and on the stress response in the time evolution of the maximum Von Mises stress in the domain. Thus, the material properties of the cylinders are set such that viscoelasticity is the only difference between the two simulations. The material properties in Table 6.1 are used for the surrounding air and cylinder materials. For both cylinder materials, $\rho = 1000$ kg/m^3 and $\kappa = 0.615$ W/(K m). By contrast to Kitamura *et al.* (2014) which used the stiffened gas EOS, our simulations are conducted with the NASG EOS to model the cylinder. Therefore, the speed of sound of the materials in the cylinders is higher and we expect to see small differences in numerical Schlieren and pressure contours when compared to Kitamura *et al.* (2014). In the water case, the compressible Navier-Stokes solutions are solved. For the Zener solid case, the model in §3.4.1 is solved with one relaxation time, $\mu_b = 50$ mPa s, $G = 1$ MPa, $G_r = 0.5$ MPa, $\varsigma^{(1)} = 1$, and $\theta^{(1)} = 10$ MHz. Simulation results of the numerical Schlieren function of Chang & Liou (2007); Kitamura *et al.* (2014), $(1 + (\alpha^{(1)})^2)\log(|\nabla\rho| + 1)$, and pressure are presented in Figs. 3.9 and 3.10 for the shock-water and shock-viscoelastic solid cylinder cases, respectively.

3.6.4.1 Water cylinder.

Due to the acoustic impedance mismatch between the water and air, the shock is partially transmitted and reflected as a shock upon interaction with the cylinder. Since water has a higher speed

of sound than air, the transmitted shock propagates ahead of the shock in air and interacts with the downstream interface. The transmitted shock is partially reflected as a rarefaction and focused upstream into the cylinder (frame a and e). This process continues with phase inversion upon each reflection (frames b and f). Upon the third interaction with the downstream interface, the two cusps with a tensile pressure is observed, similar to those in Kitamura *et al.* (2014). However, this feature is further evolved in the present simulations due to a faster speed of sound in the liquid when using the NASG EOS. A shock is also transmitted into the domain, though it is too weak to be visible in the contours. Numerical oscillations in both the numerical Schlieren and pressure contours along the interface are likely due to the carbuncle phenomenon and are also observed in Kitamura *et al.* (2014). The shock diffracted from the partial reflection and the incident shock continue to propagate and are not affected by the flow inside the cylinder. The transmitted shock propagates back to the downstream cylinder interface and is reflected to form a small hoop where a compressive wave is focused (frame c and g). At $t = 18.75$ μs, the small hoop wave advects downstream and evolves into another tensile bow wave with two compressive wing-like waves (frame d and h). We conclude that despite the speed of sound differences and the minor effect of the carbuncle phenomenon (Pandolfi & D'Ambrosio, 2001), the results are qualitatively comparable to Kitamura *et al.* (2014).

3.6.4.2 Zener solid cylinder.

We set the shear modulus $G = 10$ MPa such that it is significant enough to illustrate the effect of viscoelasticity while maintaining a similar speed of sound relative to the water case. Thus, the pressure wave propagation is similar while the differences are attributed to the viscoelasticity. In the Schlieren images, the small waves can be attributed to the weaker elastic shear waves that are slower than the main wave structures described in the water case. The two cusps (frames a and e), tensile wave (frames b and f), small hoop (frames c and f), and tensile wave with compressive wing-like waves (frames d and h) described in the water case are observed for the Zener solid cylinder. The elasticity increases the stress response at the top and bottom of the cylinder interface

as the diffracted shock weakens. Moreover, the incident and diffracted shocks are slightly affected with diffracted elastic shear waves distorting the flow behind the diffracted shock (frames b-d). At later times, the wave structures inside the cylinder are significantly distorted due to the shear waves and weak numerical oscillations, with the latter due to the limited dissipation (frames f and g). These oscillations could be addressed by introducing numerical dissipation for the tangential components, $u_{l,i+1/2}$ and $\eta_{kk,i+1/2}$, of the generalized AUSM$^+$-up scheme in Eqs. (3.27) and (3.28). However, it remains unclear how to properly introduce dissipation in the tangential direction without significantly increasing the scheme's numerical stiffness.

To observe the effect of viscoelasticity, we consider the Von Mises stress as a quantity of interest,

$$\sigma_{von} = \sqrt{(\sigma_{11})^2 - \sigma_{11}\sigma_{22} + (\sigma_{22})^2 + 3(\sigma_{12})^2}, \tag{3.38}$$

which incorporates pressure and all three elastic components of the Cauchy stress tensor. The time evolution of the Von Mises stress is shown in Fig. 3.11 for the water and Zener solid cylinders. The effect of the incident shock interacting with the cylinders and being partly transmitted and partly reflected is apparent in the Von Mises stress profile at $t = 2$ μs. Starting at $t \approx 3$ μs, the profiles diverge as the Von Mises stress is significantly increased in the Zener case. At times $t \approx 7$ μs and $t \approx 11$ μs, the transmitted shock is reflected into the cylinder and doubles in strength. The subsequent peaks in the Von Mises stress profiles are attributed to the internal shocks interacting. Moreover, the results demonstrate the capability of the AUSM$^+$-up extension to the five-equation multiphase model with linear viscoelasticity.

3.7 Conclusions

In this chapter, we extend the AUSM scheme to the five-equation compressible multiphase model with viscoelasticity. Stress relaxation, elasticity and viscosity are included to describe viscoelastic media, whose deformations are assumed to be infinitesimally small such that linear viscoelasticity applies. By taking an objective Lie derivative of the constitutive relation, evolution equations are

introduced for the elastic contribution of the Cauchy stress tensor, while strains are transformed into velocity gradients. Moreover, the momentum and energy balance equations in the system have additional terms in the fluxes not previously addressed using flux-vector splitting schemes. We generalize AUSM schemes to account for the Cauchy stress tensor appearing in the viscoelastic description. We determine the appropriate discretization of the non-conservative volume fraction evolution equation in the five-equation multiphase model to prevent spurious oscillations at material interfaces. The resulting framework is built upon a spatial scheme that is solution-adaptive and high-order using explicit central differences in smooth regions and WENO primitive variable reconstruction for discontinuities. We conduct 1D numerical simulations demonstrating the approach's ability to maintain equilibrium conditions at interfaces and solve multi-material Riemann problems for gas-liquid and gas-viscoelastic solid configurations. 2D problems involving shock-cylinder problems for different fluids are computed, with density ratios up to 1000:1. Qualitative agreement is obtained with past experiments and simulations. Using our proposed approach, we successfully simulate the interaction of a shock wave interacting with a viscoelastic medium, and use the simulations to quantitatively investigate the stresses produced in the object.

Part II:

Bubble dynamics investigations

CHAPTER 4

Inertially-driven bubble collapse in a channel

4.1 Introduction

In a variety of engineering applications, cavitation bubbles are produced in confined geometries. For example, cavitation may enhance the atomization process in sprays that typically involve a liquid jet with cross-sectional areas of a few millimeters squared (Wang *et al.*, 2014; Bergeles *et al.*, 2015; Biçer & Sou, 2016). Though not well understood, cavitation is one of the main mechanisms in the erosion and fragmentation of millimeter-sized kidney stones in biomedical ultrasound therapy tools (Lubock, 1989; Pishchalnikov *et al.*, 2003; Duryea *et al.*, 2014). Ferns sporangia utilize cavitation to eject its spores akin to man-made catapults (Noblin *et al.*, 2012) and snapping-shrimp produce cavitating bubbles by rapidly closing their claws to kill their prey (Versluis *et al.*, 2010). Cavitation is the lifetime-limiting factor for the target used in the operation of the Spallation Neutron Source at Oak Ridge National Laboratory (Haines *et al.*, 2014; Riemer *et al.*, 2014; Naoe *et al.*, 2016). The spallation process produces a shock wave that propagates through the mercury in the target vessel. The shock wave interacts with the vessel walls and a long period of negative pressure is induced on the walls leading to cavitation and subsequent erosion, which limits the radiation power range and experiment duration. Additionally, confined cavitation has been observed to spontaneously occur in porous media and tree vessels (Vincent *et al.*, 2012, 2014). Vincent & Marmottant (2017) studied the effect of confinement on spherically oscillating bubbles.

While the dynamics of a bubble near a flat, rigid surface has studied, the role of confinement on

bubble dynamics is less well known. The confinement problem add one more parameter, namely, the confinement ratio R_0/W, where R_0 is the initial bubble radius and W is the characteristic size of the "container" (e.g., channel). For the problems of interest $R_0/W > \mathcal{O}(10^{-1})$, such that confinement dictates the wave dynamics throughout the collapse.

Although bubble dynamics in a confined geometry have not been systematically investigated, the collapse of a bubble near a flat, rigid surface has been studied extensively. The bubble dynamics and pressures experienced by neighboring surfaces are of key interest to characterize and predict the damage mechanisms. In particular, experimental and early numerical studies have observed the formation of a re-entrant jet for a bubble initially detached, attached from the surface (Kornfeld & Suvorov, 1944; Naude & Ellis, 1961; Plesset & Chapman, 1971; Lauterborn & Bolle, 1975; Blake & Gibson, 1987; Brujan *et al.*, 2002) and for multiple bubbles (Blake *et al.*, 1993). Variations of the canonical geometry have been studied as well with curved and inclined rigid (Wang, 1998; Tomita *et al.*, 2002) and deformable (Blake *et al.*, 1987; Brujan *et al.*, 2001; Gregorčič *et al.*, 2007) surfaces. There has been a rise of analytical (Oguz & Prosperetti, 1998; Hsiao *et al.*, 2013) and experimental (Vincent *et al.*, 2014; Fourest *et al.*, 2015; Vincent & Marmottant, 2017; Brujan *et al.*, 2018) investigations of bubbles collapsing in a channel. However, the current understanding of wave dynamics remains limited.

Numerical simulation have been used to complement theoretical and experimental efforts. Boundary integral methods were used by Blake et al. (Blake & Gibson, 1987) to predict bubble behavior during collapse near a rigid wall. However, these approaches are limited in their ability to capture the late time compressible behavior of the collapse. Advances in compressible multiphase methods and algorithms have enabled the numerical simulations of these problems with high-order accurate, high-fidelity approaches (Abgrall, 1996; Shyue, 1998; Johnsen & Colonius, 2006; Johnsen, 2012; Alahyari Beig & Johnsen, 2015). The approach of Alahyari Beig & Johnsen (2015); Alahyari Beig (2018) shows agreement agreement with experiments by Supponen *et al.* (2016) of the re-entrant jet and bubble morphology at collapse. Moreover, a pressure scaling relationship at the wall based on the initial bubble configuration for detached and attached bubbles is

developed by Beig *et al.* (2018).

The objective of this work is to study the dynamics of a single bubble inertially collapsing in a channel to gain insights on the effect of confinement on the bubble dynamics and pressures on the channel walls. The chapter outline is as follows. The physical and numerical model for binary water-gas multiphase flows are described. The numerical method of Beig *et al.* (2018) is briefly introduced and its performance on the Blue Waters supercomputing system is examined. The problem of interest, namely a single gas bubble inertially collapsing in a channel, and the relevant parameters are presented. Qualitative observations are made of the bubble and wave dynamics. We then conduct a series of quantitative observations and comparisons of the bubble dynamics, maximum pressures between the channel and single wall configurations. Results varying the channel width are presented to determine at which channel width the confinement has a negligible effect on the dynamics. We conclude with future directions for this study.

4.2 Physical and Numerical Modeling

The physical and numerical models are fully detailed in Chapter 2 and is briefly summarized for a binary-phase system. The equations of motion are mass conservation, momentum balance and energy balance:

$$\frac{\partial \rho}{\partial t} + \frac{\partial}{\partial x_j}(\rho u_j) = 0, \tag{4.1a}$$

$$\frac{\partial}{\partial t}(\rho u_i) + \frac{\partial}{\partial x_j}(\rho u_i u_j - p\delta_{ij}) = \frac{\partial \tau_{ij}}{\partial x_j}, \tag{4.1b}$$

$$\frac{\partial E}{\partial t} + \frac{\partial}{\partial x_j}((E + p)u_j) = \frac{\partial}{\partial x_k}(u_i \tau_{ij} - Q_k), \tag{4.1c}$$

where ρ is the total density, u_i the velocity vector, τ_{ij} the viscous stress tensor, Q_k the heat flux, indices $i, j = 1, 2$, and 3, and repeated indices denote summation. The total energy (per unit volume) E is comprised of internal and kinetic contributions: $E = \rho e + \frac{1}{2}\rho u_k^2$. To close the system, an equation of state is required to relate the internal energy to pressure and temperature and a

constitutive relation to define the heat flux and viscous stress tensor. The Noble-Abel Stiffened Gas (NASG) equation of state (EOS) (Le Métayer & Saurel, 2016) is used for the water vapor-water system:

$$\rho e = \frac{p(1-\rho b)}{n-1} + \frac{nB(1-\rho b)}{n-1} + \rho q \qquad \text{(pressure − wise)}, \tag{4.2a}$$

$$= \rho c T + B(1-\rho b) + \rho q \qquad \text{(temperature − wise)}, \tag{4.2b}$$

where T is the temperature and q, n, B, b and c are material properties prescribed to produce the correct sound speeds in liquids and have been validated for a wide range of pressures and temperatures (Harlow & Amsden, 1971; Le Métayer *et al.*, 2005; Le Métayer & Saurel, 2016). Table 6.1 lists the experimentally fitted constants where a is the material's sound speed.

Fourier conduction describes the heat diffusion process and flux:

$$Q_k = -\kappa \frac{\partial T}{\partial x_k}, \tag{4.3}$$

where κ is the thermal conductivity. A newtonian constitutive relation describes the viscous stress tensor. The viscous term has bulk (dilatational) and shear contributions:

$$\tau_{ij} = \mu_b \dot{\epsilon}_{kk} \delta_{ij} + \mu_s \dot{\epsilon}_{ij}^{(d)}, \tag{4.4}$$

where μ_b is the bulk viscosity, μ_s the shear viscosity, and

$$\dot{\epsilon}_{ij} = \frac{1}{2}\left(\frac{\partial u_i}{\partial x_j} + \frac{\partial u_j}{\partial x_i}\right), \qquad \dot{\epsilon}_{ij}^{(d)} = \dot{\epsilon}_{ij} - \frac{1}{3}\dot{\epsilon}_{kk}\delta_{ij}, \tag{4.5}$$

is the strain-rate tensor and its deviatoric part.

The five-equations multiphase model (Allaire *et al.*, 2002; Murrone & Guillard, 2005; Alahyari Beig & Johnsen, 2015) is used to capture gas/liquid flows. An additional species conservation equation is solved in conservative and non-conservative form to maintain interfacial equilibrium

conditions for velocity, pressure and temperature (Alahyari Beig & Johnsen, 2015; Rodriguez & Johnsen, 2018),

$$\frac{\partial}{\partial t}(\rho^{(k)}\alpha^{(k)}) + \frac{\partial}{\partial x_j}(\rho^{(k)}\alpha^{(k)}u_j) = 0, \tag{4.6a}$$

$$\frac{\partial \alpha^{(k)}}{\partial t} + u_j\frac{\partial \alpha^{(k)}}{\partial x_j} = \Gamma^{(k)}\frac{\partial u_j}{\partial x_j}, \tag{4.6b}$$

where $\alpha^{(k)}$ is the volume fraction of the k-th phase. The right-hand-side term coefficient, $\Gamma^{(k)}$, is determined for a binary mixture (Alahyari Beig & Johnsen, 2015),

$$\Gamma^{(k)} = \frac{\alpha^{(k)}\rho^{(k')}(a^{(k')})^2}{\alpha^{(k)}\rho^{(k')}(a^{(k')})^2 + \alpha^{(k')}\rho^{(k)}(a^{(k)})^2}, \tag{4.7}$$

where $\alpha^{(k')} = 1 - \alpha^{(k)}$ and k' and k represent each phase. Similarly, the mixture material properties ϕ (e.g., moduli, viscosities, thermal conductivity, etc.) are weighted by the volume fraction:

$$\phi = \sum_k \alpha^{(k)}\phi^{(k)}. \tag{4.8}$$

Due to the numerical stiffness, the right-hand term at the beginning of the simulation, for the first 1000 time steps the algorithm solves the equations without this term. Moreover, the mixture relation for the sound speed (Brennen, 2013),

$$\frac{1}{\rho a^2} = \frac{\alpha^{(k)}}{\rho^{(k)}(a^{(k)})^2} + \frac{\alpha^{(k')}}{\rho^{(k')}(a^{(k')})^2}, \tag{4.9}$$

is used to calculate the speed of sound when using the right-hand side term in Eq. (4.6b) and

Table 4.1: Constants in the Noble-Abel stiffened gas equation of state for water vapor and water (Le Métayer & Saurel, 2016).

Medium	ρ [kg/m^3]	a [m/s]	n [-]	B [MPa]	b [m^3/kg]
Water, vapor	0.027	439.6	1.47	0	0
Water, liquid	1051	1613	1.19	702.8	6.61×10^{-4}

upwinding.

4.3 Numerical Algorithm and Performance

We leverage the numerical algorithm of Alahyari Beig & Johnsen (2015), which has been used to study the pressures and temperatures produced by inertially collapsing bubbles near a rigid wall (Beig *et al.*, 2018). A brief summary of the numerical algorithm is provided below and full details can be found in Alahyari Beig (2018).

The algorithm uses the third-order accurate Total Variation Diminishing (TVD) Runge-Kutta scheme of Gottlieb & Shu (1998) with an adaptive time step calculation following the appropriate advective and diffusion numerical constraints. The convective fluxes are computed in divergence form using a conservative, solution-adaptive fashion based on the sensor of Henry de Frahan *et al.* (2015) to discriminate between smooth regions and discontinuities. For smooth regions, standard fourth-order explicit central differences are applied. At discontinuities, the HLL Riemann solver (Harten *et al.*, 1983) is used, with appropriate correction for equations in non-conservative form (Saurel & Abgrall, 1999b) in conjunction with the high-order accurate primitive variable WENO reconstruction scheme of Johnsen & Colonius (2006). The first and second derivatives of the diffusion and source terms are computed using explicit fourth-order accurate central differences. Thus, fourth-order accuracy is achieved in smooth problems; though the global convergence rate for problems with discontinuities is first-order, as expected, smooth regions are resolved with the central scheme. The code is written in C++, uses Message Passing Interface (MPI) for parallel processing, and a hierarchical data format (HDF5) for inputting and outputting data in parallel.

We assess the scaling performance of the numerical algorithm on the National Center for Supercomputing Applications BlueWaters system by running simulations of a single bubble undergoing an inertial collapse for 100 time steps. Fig. 4.1 shows the numerical algorithm. Both scaling analyzes show efficient behavior. The problem size is kept constant and the number of processors is doubled for the strong scaling analysis. As a result, the computational wall time is reduced by

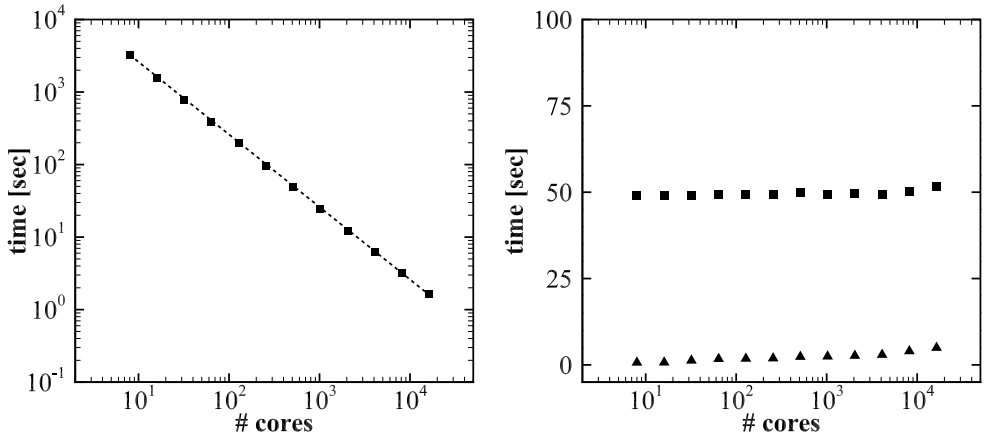

(a) Strong scaling. (b) Weak scaling.

Figure 4.1: Scaling results of the numerical algorithm on the BlueWaters Supercomputing System. Black dotted line: ideal theoretical strong scaling; Black squares: average total computing time per processor; Black triangles: average communication per processor.

nearly a factor of two. In weak scaling analysis, as the problem size is increased with the number of processors, the ideal behavior is achieved with the average total communication time between the processors incurring a minimal increase in the average total computational time of the simulation. The code exhibits ideal behavior up to 16,384 cores; the simulations in our study use 8,192 cores. Similar results were obtained for the Titan supercomputing system at the Oak Ridge Leadership Computing Facility (data not shown).

4.4 Problem Set-up

We consider a single, spherical gas bubble surrounded by liquid water in a channel. The problem set-up is shown in Fig. 4.2. The water pressure at p_∞ and temperature T_∞ surrounds the bubble. Vapor is modeled as a non-condensible ideal gas with vapor pressure p_{vapor} = 3550 Pa and temperature T_o = 300 K. The bubble has an initial radius R_0 = 500 μm and is located at a distance x_0/R_0 from the right wall. The coordinate system in the x-direction is shown with x_{C0} denoted the initial bubble centroid x-location with channel width W. Due to the symmetry in the xz- and xy-plane, a quarter of the domain is simulated with symmetric boundary conditions. The top and back planes have the non-reflecting boundary conditions (Thompson, 1990). Left and right channel walls are

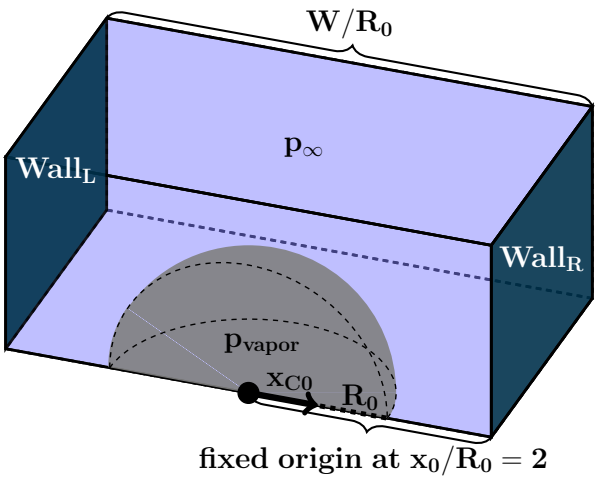

Figure 4.2: Problem set-up of an inertially collapsing bubble in a channel.

rigid walls with perfectly reflecting boundary conditions. The resolution is 192 computational cells per initial bubble radius, which corresponds to approximately 0.45 billion computational points per simulation. Average simulation takes approximately $30 - 40$ thousand time steps, corresponding to 18 wall-time hours, to reach a simulation time after bubble collapse. Three parameters of interest are considered: (i) the driving pressure, p_∞, (ii) the initial bubble centroid location, x_{C0}, and (iii) the channel width, W. The parameters of our baseline case are $p_\infty = 5$ MPa, $x_{C0}/R_0 = 0.75$, and $W/R_0 = 4$. In this study, we vary the parameters of interest. Three different driving pressures are considered, $p_\infty = 2, 5$, and 10 MPa, which have been studied by others for various cavitation applications (Franc *et al.*, 2011; Beig *et al.*, 2018). The corresponding water temperature, T_∞, is determined by the NASG equation of state. At least four different initial bubble centroid locations are rigid walls with perfectly reflecting are considered: 0 (centered in the channel), 0.5, 0.75, and 0.875. Eight channel widths are considered in the range $W = [3, 8]$. The quantities of interest are compared with those obtained from Beig *et al.* (2018) for a single bubble inertially collapsing near a rigid boundary. In the single wall configuration, the same problem set-up is used with $W \to \infty$ and the left boundary condition is a non-reflection boundary condition.

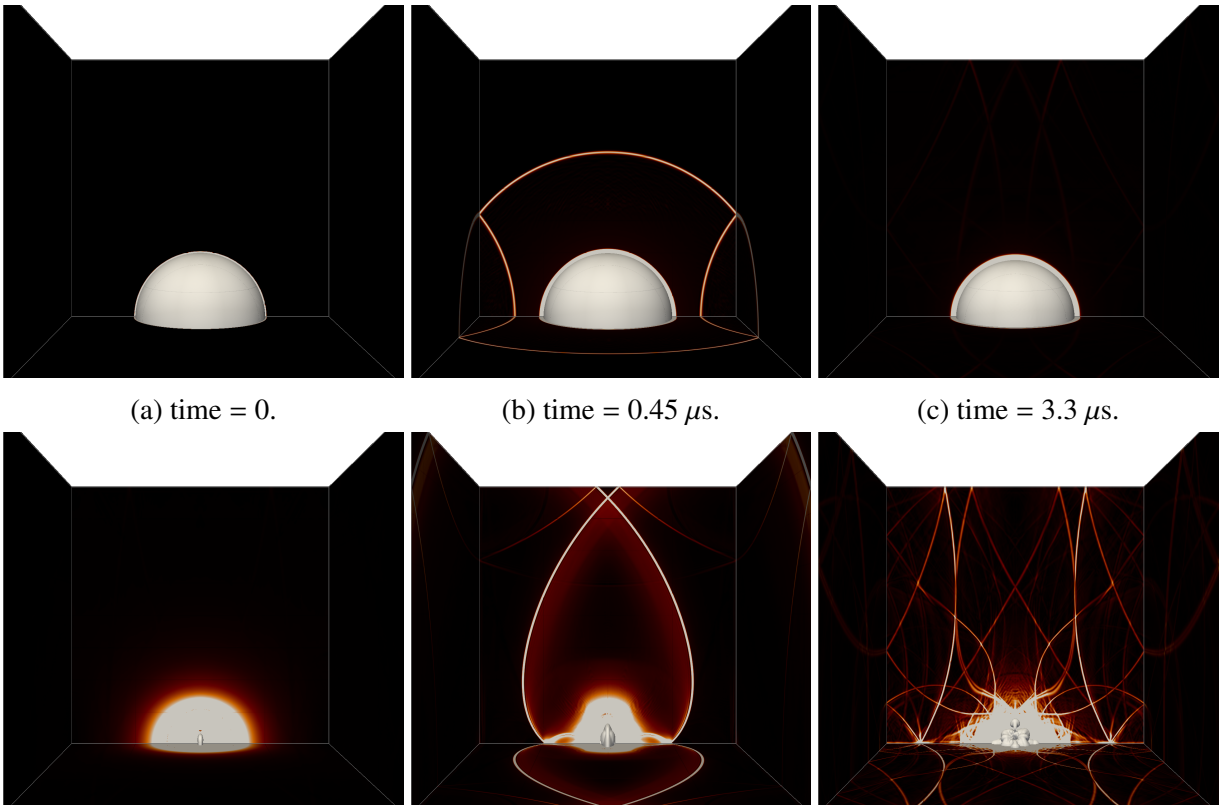

(a) time = 0. (b) time = 0.45 μs. (c) time = 3.3 μs.

(d) time = 8 μs. (e) time = 9 μs. (f) time = 12.5 μs.

Figure 4.3: Numerical Schlieren contours along the centerline *xz*-, *xy*-plane, and channel walls for an inertially collapsing bubble in a channel with $x_{C0}/R_0 = 0$ (symmetric case). White iso-surface represents the bubble interface approximate location.

4.5 Results

4.5.1 Qualitative Results

Fig. 4.3 shows numerical Schlieren contours along the four boundary planes, i.e., the centerline *xz*-, *xy*-planes, and channel walls, along with an isocontour of the volume fraction to illustrate the bubble interface, for the baseline simulation. The initial condition is shown in frame a for this Rayleigh collapse corresponds to a Riemann problem, which releases an inward-propagating shock and an outward-propagating rarefaction while the interface moves radially inward (frame b). Due to the acoustic impedance mismatch between the water and water vapor, the driving pressure is reflected away from the bubble as an outward-propagating rarefaction wave that is then

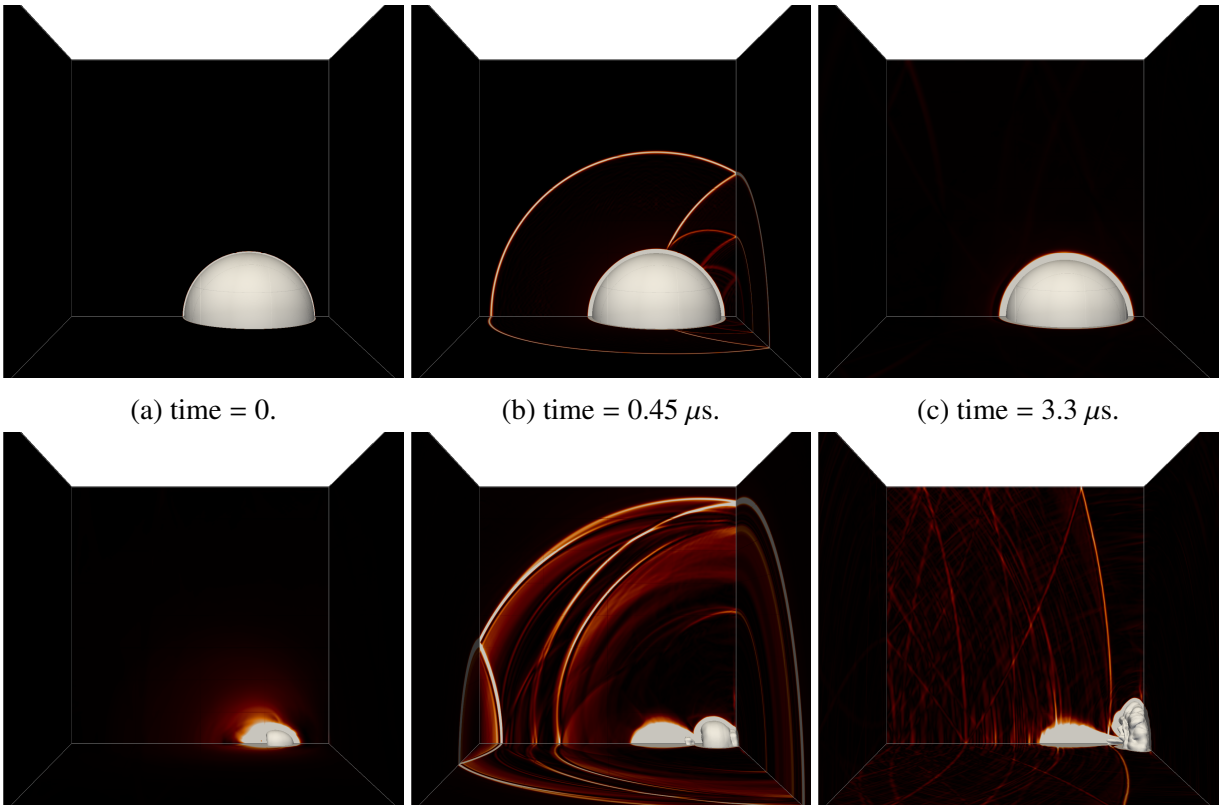

(a) time = 0. (b) time = 0.45 μs. (c) time = 3.3 μs.

(d) time = 8 μs. (e) time = 9 μs. (f) time = 12.5 μs.

Figure 4.4: Numerical Schlieren contours along the centerline *xz*-, *xy*-plane, and channel walls for an inertially collapsing bubble in a channel with $x_{C0}/R_0 = 0.75$. White iso-surface represents the bubble interface approximate location.

reflected towards the bubble by the channel walls in a symmetric fashion (frame b). The rarefaction waves continue reflecting between the wall and the bubble as the bubble begins to implode (frame c). These waves change polarity upon reflections off the bubble interface due to the impedance mismatch. Over time, the amplitude of these waves diminishes. During the collapse, the pressure gradients from these waves deposit baroclinic vorticity along the bubble interface leading to re-entrant jets at the right and left bubble interface directed towards either wall (frame d). The jets further penetrate the bubble during collapse and eventually impinge upon each other. The bubble then achieves minimum volume, and emits an outward-propagating water-hammer shock into the surroundings (frame d and e).

For comparison, we consider a case with the initial bubble centroid location at $x_{C0}/R_0 = 0.75$ in Fig. 4.4 (frame a). As in the previous case, the initial Riemann problem leads to an inward-

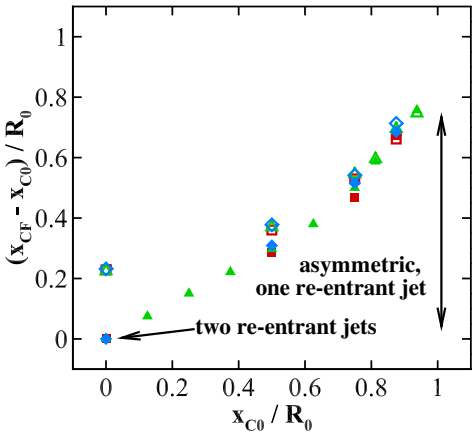

Figure 4.5: Bubble centroid location at collapse for an inertially collapsing bubble in a channel at three different driving pressures. Red symbols: 2 MPa; green symbols: 5 MPa; blue symbols: 10 MPa. Filled symbols: channel; empty symbols: single wall.

propagating shock, outward-propagating rarefaction, and inward-moving bubble interface. Due to the asymmetry in the geometry, the rarefaction reflected off the right wall interacts with the bubble first (frame b and c). The collapse is asymmetric, with a single re-entrant jet directed towards the right wall (frame d). The impingement of the jet upon the distal side of the bubble produces an outward propagating water-hammer shock (frame e). The bubble centroid moves in the x-direction towards the right wall as it collapses (frame c-e). After collapsing, the bubble takes the form of a vortex ring forms convecting towards the right wall (frame f).

4.5.2 Bubble Migration and Collapse Volume in a Channel

Two quantities of interest for the bubble dynamics are the migration distance of the bubble centroid from the initial location to the location at collapse, i.e., $x_{C0} - x_{CF}$, and the volume at collapse. These two quantities indicate the bubble proximity to the neighboring wall and intensity of its collapse. Comparing these quantities between the channel and single wall configurations reveals the effect of confinement, in any, on bubble dynamics. Fig. 4.5 shows the bubble migration distance for the three different driving pressures and various x_{C0} locations for both the channel and single wall configurations. For the initially symmetric case, i.e., $x_{C0} = 0$, the bubble undergoes a symmetric collapse (as seen in Fig. 4.3) and collapses at its original location. The single wall configurations

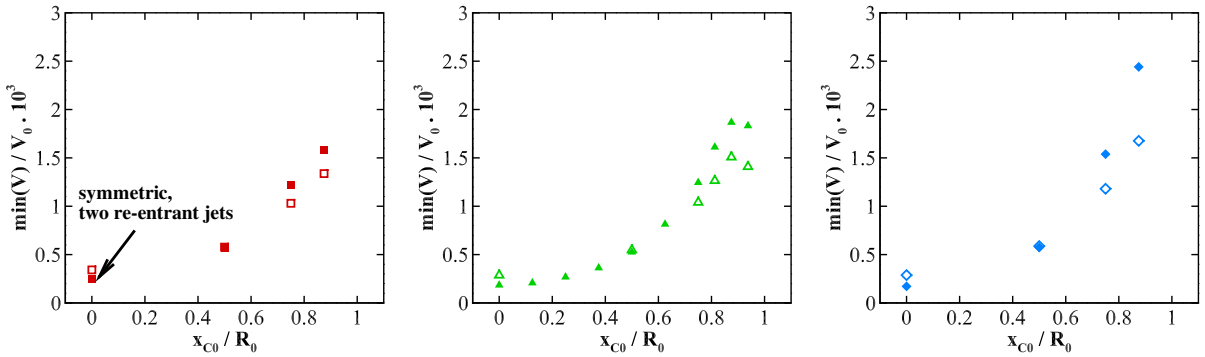

(a) p_∞= 2 MPa. (b) p_∞= 5 MPa. (c) p_∞= 10 MPa.

Figure 4.6: Minimum bubble volume for an inertially collapsing bubble in a channel at three different driving pressures. Filled symbols: channel; empty symbols: single wall.

have a positive bubble migration distance. For non-zero initial bubble locations, the bubble collapses asymmetrically and a single re-entrant jet is observed. As the initial bubble location is set closer to the wall, the migration distance tends to that for a single wall configuration. This result is expected as the initially released rarefaction travels a longer distance toward the left wall before interacting with the bubble; in the limiting case of the left wall being infinitely far from the bubble (or far enough that the rarefaction does not have time to travel there and back before collapse), the problem reduces to that of a single bubble collapsing near a single wall.

The intensity of the bubble collapse can be quantified by the minimum bubble volume which is achieved at collapse. Fig. 4.6 shows the minimum bubble volume for the different driving pressures for the channel and single wall configurations. The smallest minimum volume is achieved under symmetric collapse ($x_{C0} = 0$). This is attributed to the increased inertia from the two impinging re-entrant jets (Figs. 4.3) further compressing the bubble into a smaller volume relative to the single re-entrant jets. For $0 \leq x_{C0} < 0.5$, the minimum bubble volumes achieved in the channel are smaller than those in the single wall configurations. For $x_{C0} > 0.5$, the trend is inverted with the smaller minimum volumes being achieved for the single wall configuration. This is due to the bubbles in the channel configuration feeling the effect of the reflected leftward propagating rarefaction, which reduces the intensity of the collapse.

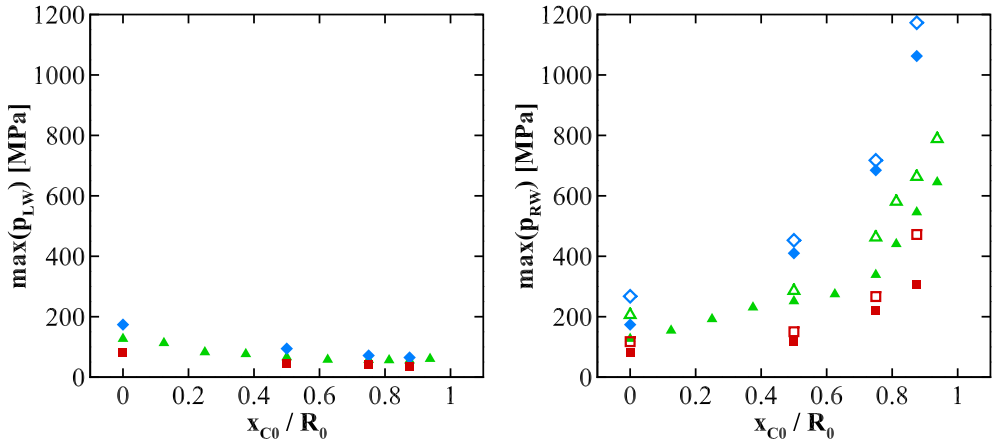

(a) Left wall. (b) Right wall.

Figure 4.7: Maximum pressures for the left and right walls for an inertially collapsing bubble at three different driving pressures. Red symbols: 2 MPa; green symbols: 5 MPa; blue symbols: 10 MPa. Filled symbols: channel; empty symbols: single wall.

4.5.3 Maximum Pressures on the Channel Walls

The maximum pressures experienced at the channel wall are considered as they are indicative of the impact loads driving cavitation erosion and shown in Fig. 4.7. Except for the x_{C0} case, the maximum pressures at the left channel wall are significantly lower than those at the right wall. As evidenced in Fig. 6.6, which shows that the minimum volume is smallest for the more symmetric collapse, the collapse pressure is highest for stand-off distances close to $x_{C0} = 0$. However, the dependence of the maximum wall pressure on initial stand-off distance indicates that the dominant factor for determining the wall pressure is the location of the bubble at collapse. The single wall configuration yields higher maximum pressures at the right wall than those in the channel. This result is expected for $x_{C0} > 0.5$ as bubble minimum volume is smaller for single wall configuration than in the channel (see Fig. 4.6). For cases with $x_{C0} \leq 0.5$, the channel configuration yields more violent collapses and stronger outward-propagating shocks than the single wall configuration. However, the rarefactions trapped in the channel limit the collapse intensity (see Fig. 4.6) and, therefore, the strength of the emitted water-hammer shock at the right wall relative to the single wall configuration. While the confined geometry leads to highly-focused collapses that are more violent than their single wall counterpart for cases $x_{C0} \leq 0.5$, the trapped rarefaction waves lead to

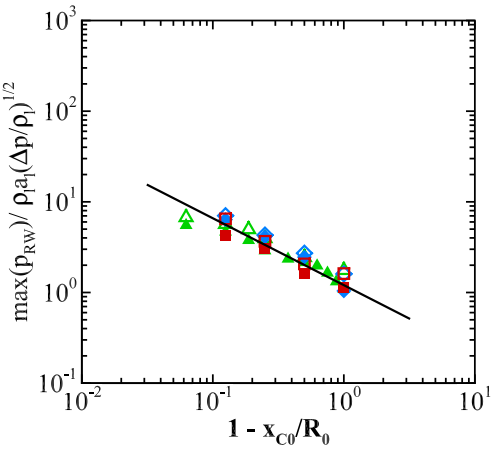

Figure 4.8: Maximum pressures for the left and right walls for an inertially collapsing bubble at three different driving pressures. Red symbols: 2 MPa; green symbols: 5 MPa; blue symbols: 10 MPa. Filled symbols: channel; empty symbols: single wall.

lower maximum pressures at the right channel wall for all x_{C0} relative to the single wall configuration. Fig. 4.8 shows the maximum pressures nondimensionalized by the scaling developed by Beig *et al.* (2018) with the results appearing to collapse to the same single curve as that for the single wall configuration. The maximum pressures are nondimensionalized by $\rho_l a_l(\Delta p/\rho_l)^{1/2}$, where ρ_l and a_l are the density of water and water sound speed, respectively, and $\Delta p = p_\infty - p_{vapor}$. Moreover, the maximum pressure at the wall decays as $1/(1 - x_{C0})$ which was also shown by Johnsen & Colonius (2009a).

4.5.4 Channel Width Dependence on the Inertial Bubble Collapse Dynamics

The results provided above demonstrate that for a confinement ratio $R_0/W = 0.25$, the initial location of the bubble in the channel has an effect of the dynamics relative to the single wall. We now investigate the effect of confinement by varying the channel width, i.e., W, to determine the confinement ratio at which the dynamics achieve the single wall results. Such knowledge provide a criterion at which point confinement effects need not be considered when developing cavitation-induced damage mitigation strategies. The initial bubble centroid location and driving pressure are fixed to the baseline values, i.e., $x_{C0} = 0.75$ and $p_\infty = 5$ MPa. Fig. 4.9 shows the bubble centroid migration distance and minimum bubble volume achieved at collapse. Expected results

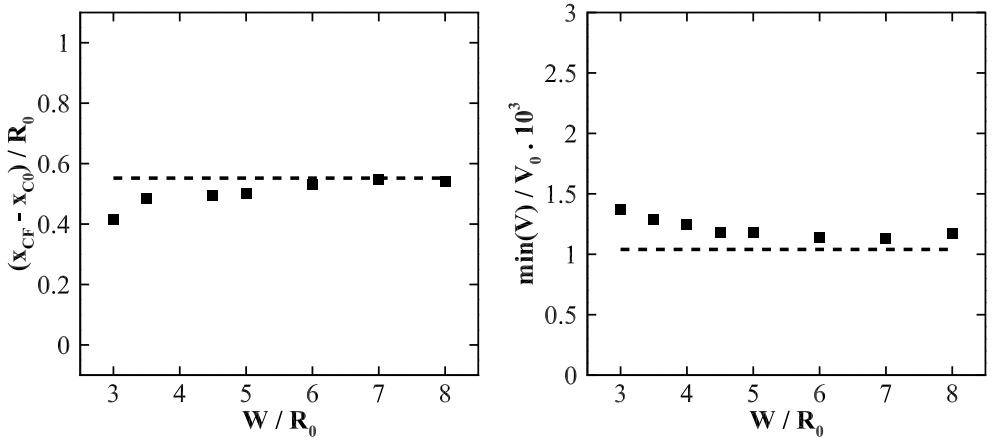

(a) Bubble migration distance. (b) Minimum bubble volume.

Figure 4.9: Bubble centroid location at collapse and minimum bubble volume of an inertially collapsing bubble for various channel widths. Black dotted line: single wall bubble collapse.

are achieved; as the channel width increases, the migration distance and minimum bubble volume asymptotically approach the value observed in the single wall configuration. Additionally, for channel widths $W > 8 \times R_0$, the leftward rarefaction from the driving pressure and shock from the collapse no longer have an appreciable effect on the collapse dynamics. This is attributed to the rarefactions waves not having enough time to travel to the left wall and reflect back onto the bubble by the time of collapse. Moreover, the bubble migration and minimum volume increase as the confinement, R_0/W, increases which is attributed to increasing symmetry in the initial configuration leading to a more intense collapse as seen in the $W = 4$ cases (see Figs. 4.5 and 4.6). Fig. 4.10 shows the maximum pressures on the channel walls. On the left channel wall, the expected $1/r$ decay is achieved as the water-hammer shock traverses longer channel distances. The maximum pressures at the right channel wall demonstrate similar behavior as the bubble dynamics results in Fig. 4.9 and additional simulations for longer channel widths will need to be studied.

4.6 Conclusions

The effect of confinement on dynamics of inertially collapsing bubbles and the mechanisms that lead to cavitation erosion are not well understood. We conducted numerical simulations to gain

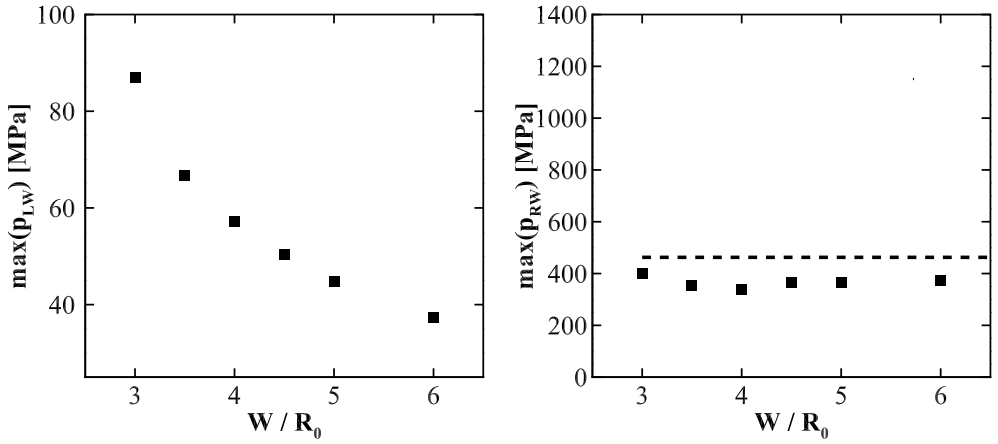

(a) Left wall. (b) Right wall.

Figure 4.10: Maximum pressure at the left and right walls for various channel widths. Black dotted line: single wall bubble collapse.

insights into the effect of confinement for a single inertially collapsing bubble in a channel. We leveraged the numerical algorithm of Beig *et al.* (2018) and characterized its performance to compare quantities of interest for two configurations (channel and single wall) as parameters of interest (bubble centroid initial location, driving pressure, channel width) were varied. Differences were observed in the bubble migration distance and volume at collapse between the single wall and channel wall configuration. For $x_{C0} = 0$, channel configuration exhibit the smallest volume due to the impingement of two re-entrant jets increasing the bubble compression and intensifying the collapse. At $x_{C0} = 0.5$, an inversion of the minimum bubble volume at collapse between the channel and single wall configures was observed. This was attributed to the trapped rarefaction waves (tension) in the channel decreasing the inertia (compression) driving the collapse. Similar behavior occurred for the maximum pressures at the right channel wall and the scaling developed by Beig *et al.* (2018) for the single wall holds for a channel as well. We observed that for widths $W > 8 \times R_0$ the effect of confinement diminishes significantly and approaches the single wall configuration values. This is attributed to the rarefaction wave from the Rayleigh collapse not having sufficient time due to the increased distance to travel to the left wall and reflect back onto the bubble to enhance the collapse intensity. Future studies will examine the appropriate scaling relations to predict pressures and on channel surfaces.

CHAPTER 5

Shock-induced collapse as a mechanism enhancing stone comminution in extracorporeal shock wave lithotripsy

5.1 Introduction

Cavitation bubble dynamics plays an important role in a number of cavitation-based biomedical ultrasound procedures. Extracorporeal shock wave lithotripsy (ESWL) is a non-invasive ultrasound therapy tool used to fractionate kidney stones (Lubock, 1989). Shock waves are generated outside the body and focused to fragment kidney stones to the extent that they can then be passed by the renal system (Coleman *et al.*, 1987; Sass *et al.*, 1991). A common ESWL waveform consists of a positive pressure peak (a shock) followed by a rarefaction, which reaches ~10 MPa in tension. The peak pressures used in practice are ~40 MPa (Coleman *et al.*, 1987; Zhu *et al.*, 2002). The tensile region generates cavitation bubbles along the kidney stone surface, which grow and collapse. Two primary stone comminution mechanisms have been proposed based on experimental observations: (i) the tensile stresses generated from the reflected shock waves within the stone leading to spallation, and (ii) cavitation erosion fatiguing and leading to material failure (Lubock, 1989; Crum, 1988; Zhong *et al.*, 1993; Brujan, 2004; Weinberg & Ortiz, 2009). Moreover, experiments by Zhu *et al.* (2002) in water and castor oil demonstrated that the combined effect of the tensile stress wave and the cavitation produce the most effective comminution (see Fig. 1.3).

Numerical simulations have been used to gain insights into stone communition mechanisms. To determine the tensile stress leading to spallation inside the stone, studies have focused on the wave propagation inside the stone to determine how and where stresses form inside the stone (Dahake & Gracewski, 1997a,b; Mihradi *et al.*, 2004; Cleveland & Sapozhnikov, 2005; Weinberg & Ortiz, 2009). These solvers, however, were designed to represent the wave dynamics and small deformations, and do not take into account the interaction between the shock wave and cavitation bubbles along the surface of the stone. A bubble cloud model has been used to study the pressure loadings of the stone (Krimmel *et al.*, 2010) from the bubble collapses by coupling the fluid dynamics results with the solids mechanics solver of Cleveland & Sapozhnikov (2005). However, this study used a bubble cloud model that neglects the asymmetric collapses bubbles undergo near rigid objects (Tanguay, 2004). Direct simulations by Johnsen & Colonius (2008) were used to study shock-bubble interaction by modeling the stone as a rigid wall. These simulations accounted for the asymmetric collapse of the bubble and the subsequent effects (i.e., re-entrant jet and emitted water-hammer shock wave). In a separate study, these results were coupled with the solver of Cleveland & Sapozhnikov (2005) to determine the wave propagation of inside stone using as a results from the bubble collapse near the wall (Kim *et al.*, 2014). However, the wave interactions (i.e., transmission and reflections) between stone and the bubble and their effect on kidney stone comminution has yet to be studied. By leveraging our novel numerical described in Chapter 2 (Rodriguez & Johnsen, 2018), novel insights are obtained on the interplay of these wave interactions and their role in kidney stone comminution.

The objective of this chapter is to study the bubble and wave dynamics of a shock-bubble interaction near a model kidney stone. We leverage our numerical model to conduct 2D numerical simulations to investigate the bubble dynamics and wave propagation in ESWL by studying shock-induced bubble collapse near a model kidney stone. The effect of different model kidney stone sizes and bubble location stand-off distances on the maximum principal stress in the stone are investigated. Moreover, an augmentation of the potential for material failure when the cavitation bubble is present is achieved relative a problem with no bubble present.

5.2 Single-bubble Collapse Near a Model Kidney Stone

5.2.1 Problem Set-up

We consider the interaction of a shock wave with an air bubble adjacent to a model kidney stone. For simplicity and by analogy to comparisons to experiments in Chapter 2, we consider a two-dimensional version of the problem, in which the bubble is cylindrical, as is the model kidney stone. The schematic of this set-up is presented in Fig. 5.1, inspired from ESWL experiments by (Pishchalnikov *et al.*, 2003) and numerical simulations (Cleveland & Sapozhnikov, 2005). The domain size is set such that there are at least three initial bubble radii from the closest material interface. The initial bubble radius is $R_a = 300$ μm and is initialized at a stand-off distance H/R_a from the proximal side of the stone. The initial model kidney stone radius is R_s. We model the lithotripsy wave as a shock wave with a post-shock pressure of 30.4 MPa, which is consistent with amplitudes used in practice (Coleman *et al.*, 1987; Pishchalnikov *et al.*, 2003). For simplicity, we examine the role of the peak pressure of the lithotripsy wave, known to produce high pressures (Johnsen & Colonius, 2008, 2009a), and neglect the rarefaction at the tail of the wave. The ambient temperature is $300K$ and the shock is initialized with the Rankine-Hugoniot conditions. Using our numerical framework, the stone is modeled as a linear elastic solid with material properties within the ranges reported by Zhong *et al.* (1993) for kidney stones (Table 5.1). The thermal conductivity of the model kidney stone is set to $\kappa = 0.58$ W/(K m). It is known that as the comminution of the stone progresses, the effectiveness of the lithotriper shock diminishes and the cavitation is hypothesized to dominate as leading to stone comminution. Thus, we explore five different stone sizes, from $R_s = 1$ mm (small stone) to 2 mm (large stone) (Johnsen & Colonius, 2009b). From studies of bubble collapse near a rigid wall, the initial proximity of the bubble increases the likelihood of damage from the re-entrant jet and water-hammer, thus, five different stand-off distances H/R_a are also considered. As a baseline case, $H/R_a = 2$ and $R_s/R_a = 5$ with the air bubble present. The resolution of the baseline case is 240 points per initial stone radius,

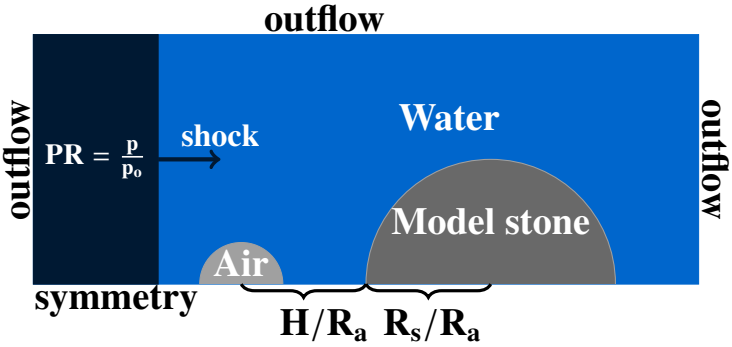

Figure 5.1: Problem set-up for the shock-induced collapse of an initially cylindrical gas bubble near a model kidney stone.

which is sufficient to resolve the wave dynamics. As limiting cases, we consider the same problem with no bubble (shock wave interaction with a kidney stone), as well as the same problem with no model kidney stone (shock-bubble interaction). The resolution is 48 points per initial air bubble radius. While higher resolutions are desirable to achieve convergence in the strength of the emitted shock wave, the resolution provided obtain comparable collapse strengths relative those discussed in §6.2 which are resolved.

5.2.2 Results

Fig. 5.2 shows the time evolution of pressure and numerical Schlieren contours of Chang & Liou (2007); Kitamura *et al.* (2014) for the baseline case, the same problem with no bubble, and the same

Table 5.1: Material properties corresponding to the materials used for simulations of shock-induced bubble collapse near a model kidney stone described by the NASG EOS.

Property	Air	Water	Model kidney stone
ρ [kg/m^3]	1	1000	1700
c_L [m/s]	376	1570	3500
n	1.4	1.19	2.35
b[m^3/kg$\times 10^{-4}$]	0	6.61	0
B[Pa$\times 10^9$]	0	0.702	5.45
q [kJ/kg]	0	-1.167	-1.167
c [kJ/kg·K]	0.718	4.167	4.167

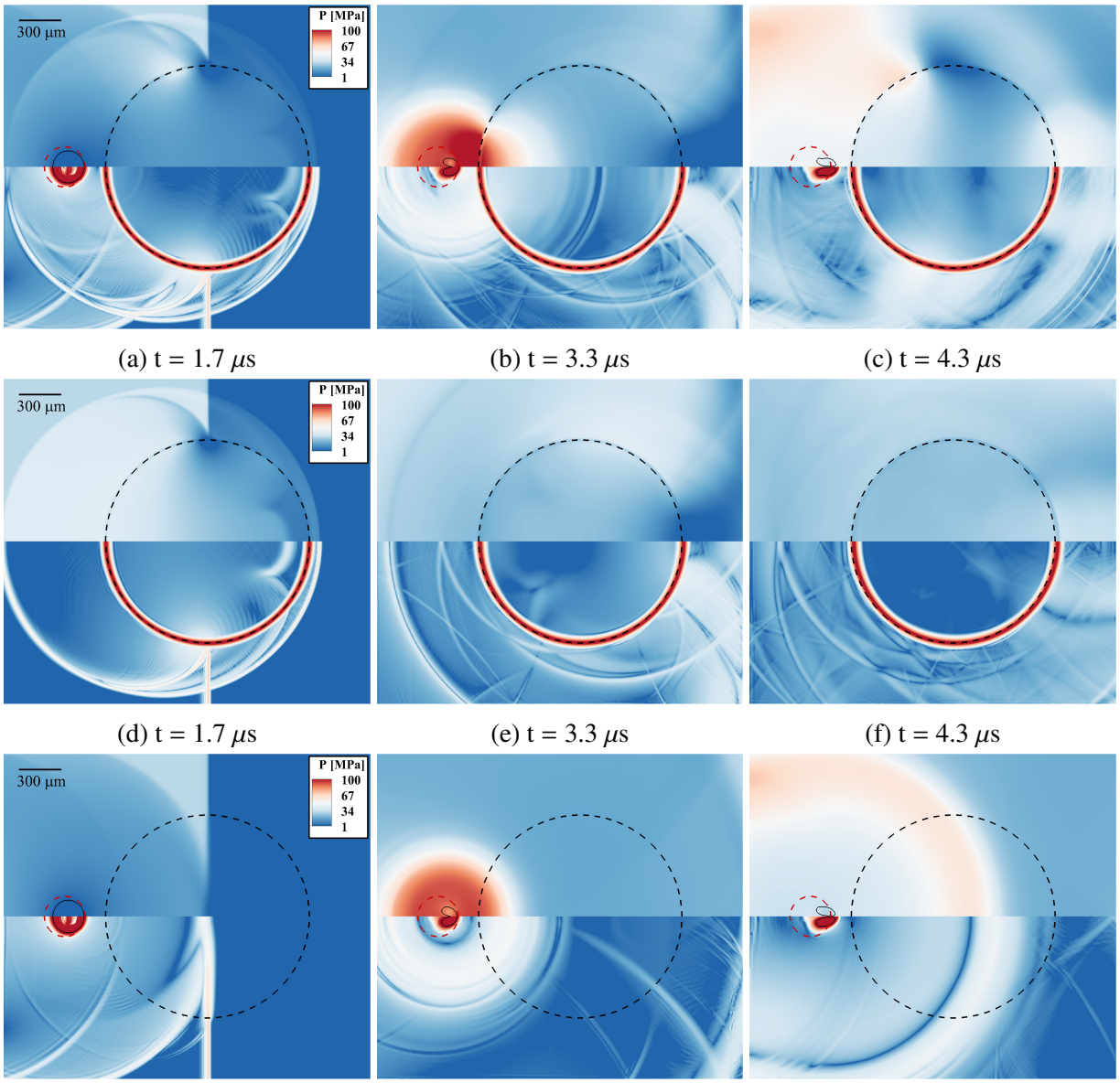

(a) t = 1.7 μs (b) t = 3.3 μs (c) t = 4.3 μs

(d) t = 1.7 μs (e) t = 3.3 μs (f) t = 4.3 μs

(g) t = 1.7 μs (h) t = 3.3 μs (i) t = 4.3 μs

Figure 5.2: Pressure (top) and numerical Schlieren (bottom) contours for the 2D shock-model kidney stone interaction problem with (top row), without a bubble (middle row), and without the model kidney stone (bottom row). Contour lines represent the material interface approximate locations.

problem with no kidney stone. After inducing the implosion of the bubble, the incident shock is partially transmitted into the model kidney stone and partially reflected to the surroundings (frames a and d). Due to the stone's higher sound speed relative to water, the transmitted shock wave reaches the distal side of the stone while the incident shock wave has propagated over a distance

of approximately one initial radius in water. The patterns of wave propagation show differences depending on whether a bubble is present or not (frame g). Upon reaching the distal side of the stone, the shock wave is partially transmitted to the water and partially reflected as a tension wave, thus forming a cusp. A four-shock TRR configuration is observed (Henderson *et al.*, 1991). This configuration involves a rarefaction propagating behind the leading shock wave and inside the stone. A similar phenomenon is observed in the simulations by Cleveland & Sapozhnikov (2005), namely, what is referred to as surface waves along the equatorial surface. The bubble collapses, forming a re-entrant jet, and subsequently implodes, emitting an outward-propagating water-hammer shock wave partially transmitted into the stone (frame b). The water-hammer shock propagates into the stone and is at the center of the stone in frame b. The water-hammer shock wave also propagates in water along the stone surface as the collapsed bubble forms into a pair of vortex lines convecting towards the stone. In the absence of the bubble, the shock waves trapped within the stone continue to undergo internal reflections and dampen over time (frames e and f). In the absence of the stone, the bubble collapse is weaker and the shock wave propagates radially out of the domain (frames h and i).

To quantify the effect of the shock-bubble interaction on the stresses experienced in the stone, the principal stresses are measured to characterize failure for brittle materials such as kidney stones (Crum, 1988; Zhu *et al.*, 2002). In 2D planar Cartesian coordinates, the principal stresses are

$$\sigma_1 = \sigma_{11}\cos^2(\theta_p) + \sigma_{22}\sin^2(\theta_p) + 2\tau_{12}^{(e)}\cos(\theta_p)\sin(\theta_p) \tag{5.1a}$$

$$\sigma_2 = \sigma_{11}\sin^2(\theta_p) + \sigma_{22}\cos^2(\theta_p) - 2\tau_{12}^{(e)}\cos(\theta_p)\sin(\theta_p). \tag{5.1b}$$

where the rotation angle to the current basis is

$$\theta_p = \frac{1}{2}\arctan\left(\frac{2\tau_{12}^{(e)}}{\sigma_{11} - \sigma_{22}}\right), \tag{5.2}$$

and $\sigma_{kk} = -p + \tau_{kk}^{(e)}$ and $\tau_{ij}^{(e)}$ is the elastic stress contribution of the Cauchy stress tensor, and $i, j = 1$

and 2. We note that a positive sign for a stress component corresponds to tension. Another quantity of interest is the maximum and minimum principal stress,

$$\sigma_{max,min} = \frac{\sigma_{11} + \sigma_{22}}{2} \pm \sqrt{\left(\frac{\sigma_{11} - \sigma_{22}}{2}\right)^2 + \tau_{12}^{(e)}}, \tag{5.3}$$

and maximum shear stress,

$$\tau_{max} = \frac{\sigma_{max} - \sigma_{min}}{2}. \tag{5.4}$$

The Von Mises stress has also been used as a failure criterion for lithotripsy simulations (Cleveland & Sapozhnikov, 2005), however, this criterion is primarily used for ductile materials so, for brevity, it is not considered for this study. In addition to the maximum principal stresses, we focus on the maximum principal stresses in tension,

$$\sigma_{T,max} = \sigma_{max} \quad \text{if} \quad \sigma_{max} > 0. \tag{5.5}$$

Fig. 5.3 shows the maximum principal stress in the 1-direction and maximum shear stress for the cases with (frames a–c) and without (frames d–f) the air bubble adjacent to the model stone. As the incident shock wave traverses the stone interface, a rarefaction (tension wave) is observed in both the maximum principal and shear stress (frame a and d). The transmitted shock wave propagates to the distal side of the stone and is reflected as a rarefaction (frames b and e). The water-hammer shock wave from the bubble collapse produces a region of maximum shear stress on the proximal side of the stone (frame b). This water-hammer shock wave then propagates to the distal side of the stone and is reflected as a rarefaction with high tension and shear (frame c). For the case with no bubble present, the trapped wave in the stone dampens as it reflects from the proximal and distal sides and does not increase the maximum principal and shear stresses (frame f). The shock-bubble interaction with no kidney stone shows the compression wave propagating through the domain and not exhibiting tensile stresses (frames g–i). The maximum values of these stresses are shown in the temporal evolution of the maximum tensile principal stress for both with

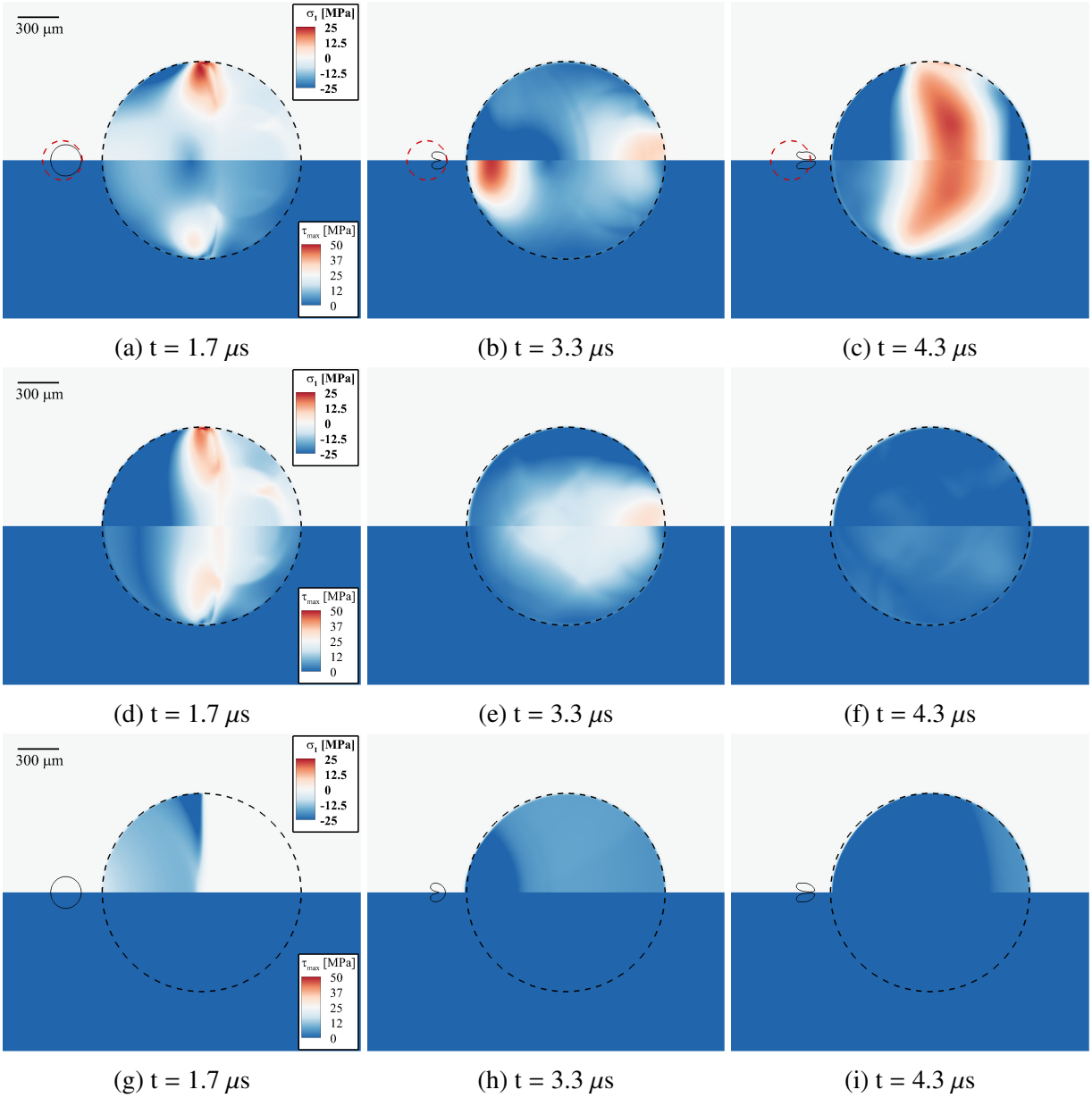

(a) t = 1.7 μs (b) t = 3.3 μs (c) t = 4.3 μs

(d) t = 1.7 μs (e) t = 3.3 μs (f) t = 4.3 μs

(g) t = 1.7 μs (h) t = 3.3 μs (i) t = 4.3 μs

Figure 5.3: Maximum principal stress in the 1-direction (top) and maximum shear stress (bottom) contours for the 2D shock-model kidney stone interaction problem with (top row), without a bubble (middle row), and without the model kidney stone (bottom row). Contour lines represent the material interface approximate locations.

and without the bubble in Fig. 5.4. The three peaks in the maximum principal stress in tension correspond to the three key events in the flow: (i) the incident shock wave propagation along the stone surface t~1–2.5 μs, (ii) the water-hammer shock wave from the bubble partially transmission into the stone t~2.5–3.5 μs , and (iii) water-hammer shock wave reflection as a rarefaction wave

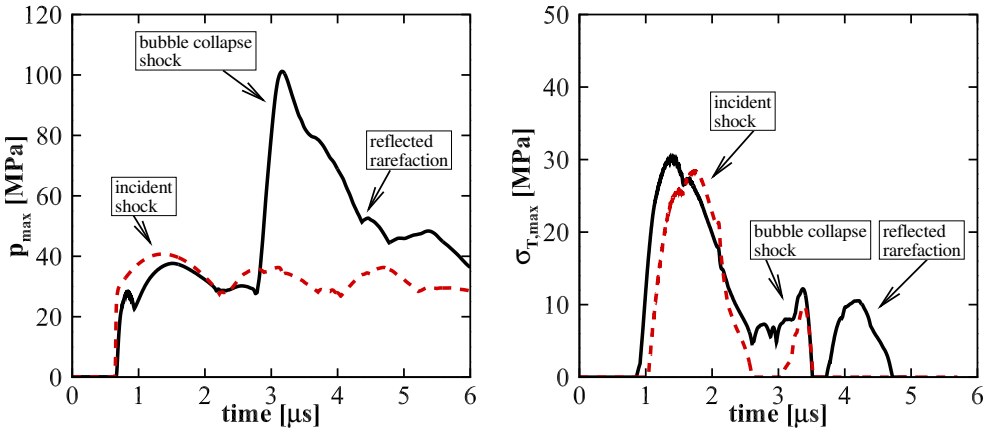

(a) Maximum pressure. (b) Maximum principal stress.

Figure 5.4: Time evolution of the maximum pressure and principal stress in the kidney model object for shock-induced bubble collapse (black solid line) and shock-model stone (red dotted line) cases.

in the stone t~3.5–5 μs. Comparing the maximum tensile principal stresses evolution with and without the bubble, the presence of the bubble generates higher maximum tensile principal stresses relative to the shock-model kidney stone interaction. This is due to the rarefaction from the incident shock-bubble interaction, augmenting the tension in the TRR configuration. Moreover, the wave-bubble interactions near the stone augment the tensile stress response and likelihood of material failure also observed in experiments (Crum, 1988; Sass *et al.*, 1991; Holmer *et al.*, 1991; Zhu *et al.*, 2002).

The relative importance of these three peaks is expected to depend on the size of the stone. The effect of the stone size and initial air bubble stand-off distance on the maximum bubble re-entrant jet velocity, a measure of the bubble collapse violence, is shown in Fig. 5.5. For comparison, the value corresponding to the shock-induced bubble collapse in a free field is also included. Higher maximum re-entrant jet velocities are achieved with the bubble collapsing near the stone due impedance mismatch between the water and stone partially reflecting the incident shock wave towards the air bubble furthering its collapse. The maximum re-entrant jet velocity has no observable dependence on the stone size. As H/R_a increased, the jet velocity decreases asymptotically to the results observed in collapse in a free field.

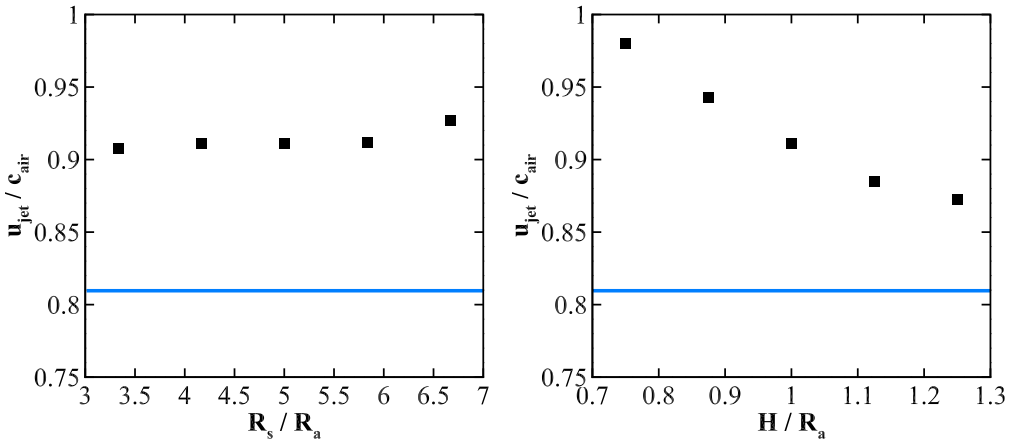

(a) R_s/R_a dependence, $H/R_a = 2$. (b) H/R_a dependence, $R_s/R_a = 5$.

Figure 5.5: Maximum bubble jet for different model kidney stone sizes, R_s/R_a, and bubble stand-off distances from the stone, H/R_a. Black squares: shock-induced bubble collapse near a stone, blue line: shock-induced bubble collapse in a free field.

The maximum tensile principal stresses dependence on stone size and initial bubble stand-off distance is shown in Figs. 5.6 and 5.7, respectively, for the three peaks identified in Fig. 5.4. The shock-kidney stone interaction results are presented for comparison. The incident shock wave generates the largest maximum tensile principal stress experienced throughout the simulation, followed by the water-hammer shock wave emitted by the bubble and its reflected rarefaction wave. However, the presence of the bubble leads to a smaller tensile response relative to having only the shock-stone interaction for kidney stones smaller than $R_s/R_a \approx 4.2$. This is due to the bubble shielding the model kidney stone from the incident rarefaction wave. A similar trend is observed for the reflected rarefaction and emitted shock. Minimal dependence of the maximum tensile response on the initial bubble stand-off distance is observed for the incident and water-hammer shock wave time periods. The closer the bubble to the stone, the stronger the emitted shock wave due to the partially reflected shock wave further compressing the bubble as it collapses. However, in these cases, most of the water-hammer shock wave from the bubble collapse is reflected towards the bubble and does not propagate along the stone surface; subsequently, this leads to a weaker maximum tensile stress in the stone. These results provide insights on the interplay between the spallation and bubble collapse wave dynamics achieve preferential gains towards breaking up large

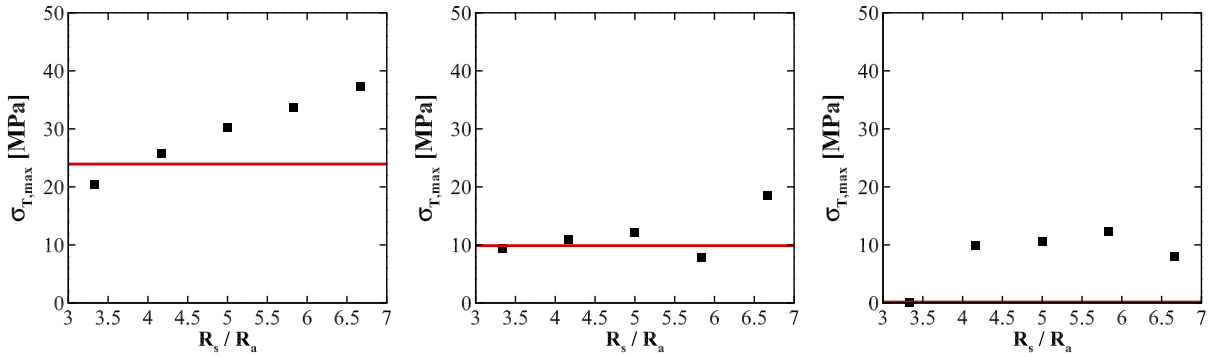

(a) Incident shock. (b) Bubble collapse shock. (c) Reflected rarefaction.

Figure 5.6: Peak values of the maximum principal stress in tension at three different times for five different model kidney stone sizes, R_s/R_a. $H/R_a = 2$. Black squares: shock-induced bubble collapse, red line: shock-model kidney stone interaction (no bubble case).

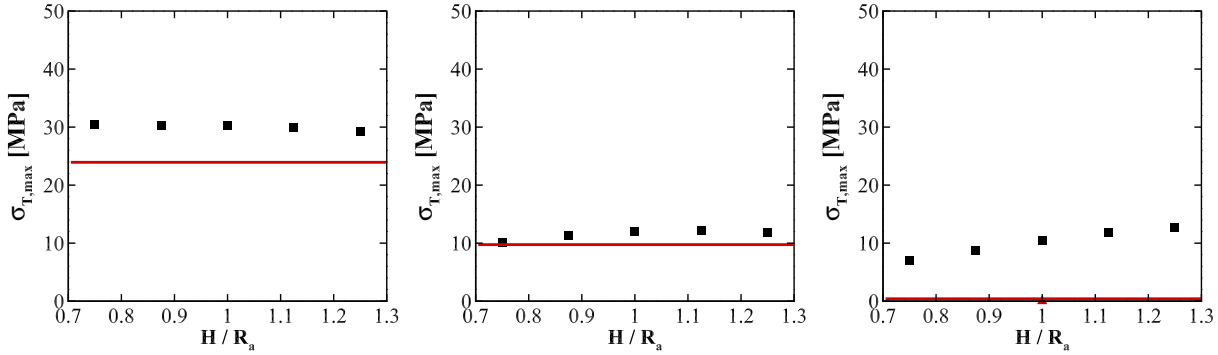

(a) Incident shock. (b) Bubble collapse shock. (c) Reflected rarefaction.

Figure 5.7: Peak values of the maximum principal stress in tension at three different times for five different air bubble stand-off distances, H/R_a, from the model kidney stone. $R_s/R_a = 5$. Black squares: shock-induced bubble collapse, red line: shock-model kidney stone interaction (no bubble case).

stones. These gains diminish for stones sizes $R_s/R_a < 4$.

5.3 Conclusions

To provide a better understanding of cavitation erosion in ESWL, we carried out high-resolution numerical simulations of 2D shock-induced collapse of an initially cylindrical gas bubble near a model kidney stone. We characterized the wave and bubble dynamics of shock-induced collapse near a model kidney stone for various stone sizes and initial bubble location stand-off distances

modeling extracorporeal shock wave lithotripsy. The peaks in maximum tensile principal stresses were identified with the three events in the flow. Significant increases in the maximum tensile principal stresses in the model stone were observed when a nearby bubble is present relative to a shock-stone configuration. This increase in the maximum tensile principle stress depends on the model stone size with no appreciable gain observed for $R_s/R_a < 4$. The gain was found to be insensitive to initial bubble location stand- off distance from the stone. These results support, in part, the three stage process of kidney stone comminution process detailed in Johnsen & Colonius (2009b). In this process, the shock wave leads the kidney stone comminution process for larger stones (i.e., $R_s > 2$ mm). An important result is that cavitation bubbles near the kidney stones amplify the potential for spallation from the shock wave. For smaller stones, the potential for spallation via shock wave diminishes due to the shielding from the incident shock wave. In these instances, the cavitation damage (e.g., the re-entrant jet) dominate the kidney stone comminution. Different shapes for the model stone and relevant lithotripsy wave forms to interact with the stone and induce the bubble collapse will be the subject of future studies. Moreover, these results are expected to change for 3D simulations as the incident wave, depending on the model kidney stone size and shape, can be highly focused within the stone.

CHAPTER 6

Effectiveness of elastomeric coatings in mitigating shocks produced by bubble collapse

Portions of this chapter are adapted from Alahyari Beig *et al.* (2016).

6.1 Introduction

Flows in naval engineering involve low-Mach number regions in the liquid, while local Mach numbers can be supersonic in gas/liquid mixture regions where the sound speed can be as low as tens of meters per second (Reisman *et al.*, 1998; Gnanaskandan & Mahesh, 2015; Ganesh *et al.*, 2016). One of the important consequences of cavitation is the structural damage to neighboring surfaces due to bubble collapse (Kornfeld & Suvorov, 1944; Philipp & Lauterborn, 1998; Lindau & Lauterborn, 2003; Franc *et al.*, 2012). The structural damage on these surfaces or coatings degrades the performance and need for require or replacement of critical components. Cavitation erosion to hard, ductile materials is relatively well understood. The modern description of cavitation erosion is based on a sequence of four steps (Kim *et al.*, 2014): production of small-scale vapor structures, impact loads due to bubble collapse, pitting, and failure. According to this model, cavitation erosion originates from the impact loading produced by the local bubble dynamics on the material. It is unclear whether this description holds for cavitation damage to compliant, elastomeric materials, such as polyurea, proposed and studied for blast mitigation (Amini *et al.*, 2010; Grujicic *et al.*, 2012; Samiee *et al.*, 2013) and in naval hydrodynamic applications. One challenge lies in

the non-trivial implementation of constitutive models describing the material that include effects such as (nonlinear) elasticity, history and viscosity. Studies have shown that these materials can have a viscoelastic response (Qiao *et al.*, 2011). The propagation of shock and rarefaction waves in a multiphase medium interacting with these neighboring soft materials results in a multiscale and multi-physics problem at the intersection of fluid and solid dynamics. Although this problem has been investigated over the past years, effective mitigation strategies have yet to be developed.

Numerical simulations have been used to complement analytical and experimental studies of bubble dynamics and cavitation erosion. Early simulations of the bubble dynamics implemented incompressible approaches to predict the initial behavior of the bubble (Blake & Gibson, 1987). However, such methods break down in the stages of the collapse when compressibility effects become important. Recently, researchers have been focusing on developing algorithms capable of simulating these flows by solving the Euler equations in a compressible framework to handle shocks, contacts and material interfaces (Ball *et al.*, 2000; Nourgaliev *et al.*, 2006; Johnsen & Colonius, 2006; Hawker & Ventikos, 2012; Coralic & Colonius, 2014). These algorithms tend to be computationally expensive and challenging in their implementation. They also bring about other numerical difficulties, such as the generation of pressure and temperature oscillations across the material discontinuities for interfacial flows, which limit the usability of these methods (Abgrall, 1996; Shyue, 1998; Johnsen, 2012; Alahyari Beig & Johnsen, 2015). Viscoelasticity introduces further complications. Numerical models, based on the Rayleigh-Plesset equation (Fogler & Goddard, 1970; Tanasawa & Yang, 1970; Yang & Church, 2005; Hua & Johnsen, 2013; Gaudron *et al.*, 2015) have been developed to study the bubble dynamics near or in viscoelastic materials. However, these approaches are limited by the assumptions that the bubble dynamics are spherically symmetric and that the near-field flow is incompressible. These assumptions break down in the last stages of the asymmetric collapse of a gas bubble near a compliant object/coating. To overcome these numerical modeling issues, we leverage our novel numerical multiphase compressible model described in Chapter 2 (Rodriguez & Johnsen, 2018), to conduct high-order accurate 2D simulations of multiphase flows involving gases, liquids and solids.

The objective of the present work is to better understand the mechanisms of cavitation-induced damage near soft materials/coatings relevant to naval hydrodynamic applications. To determine the bubble, wave, and material dynamics, we consider the shock-induced collapse of a bubble and bubble pair near an elastomeric coating. In addition, we investigate the effects of bubble-bubble interactions on dynamics of a collapsing pair of bubbles. For the problem of interest, it is assumed that that the compliant object's deformations are infinitesimally small from the pressure load of an individual bubble collapse. Moreover, the bubbles collapse due to the heterogeneous environment (e.g., shocks from neighboring collapsing bubbles), for simplicity we consider a shock to induce the bubble collapse.

6.2 Single-Bubble Collapse Near a Compliant Object

6.2.1 Problem Set-up

We consider the collapse of a cylindrical air bubble of R_o in water, located a distance δ near a compliant object of thickness T covering a perfectly rigid solid. We define the total distance $H = \delta + T$. The problem setup is shown in Fig. 6.1, and is inspired from the experiments of Gibson & Blake (1982); Swantek & Austin (2010). Due to the symmetry, the top half of the domain is simulated with a symmetric boundary condition along the bottom. The initial stand-off distances from the bubble center to the neighboring surface are $\delta/R_o = [1.125, 1.875]$. The compliant object has a baseline thickness of $T/R_o = 0.75$ with a perfectly-rigid wall boundary condition at the end of the object. The initial bubble radius of 100 μm is used. We use ambient temperature 300 K and the shock is initialized using the appropriate Rankine-Hugoniot conditions. The post-shock pressure is p_s, ambient pressure p_o and PR $= p_s/p_o = 300$. Two media are considered for the compliant object: (i) water as a baseline case and (ii) polyurea, an elastomeric material. The numerical approach detailed in Chapter 2 with the Kelvin-Voigt model is used to compute this problem. The polyurea is modeled as a Kelvin-Voigt solid using the following approximated property values: $\rho = 1190$ kg/m^3, $\kappa = 0.58$ W/m/K, $\mu_b = \mu_s = 0.5$ Pa s. We use a uniform Cartesian grid with

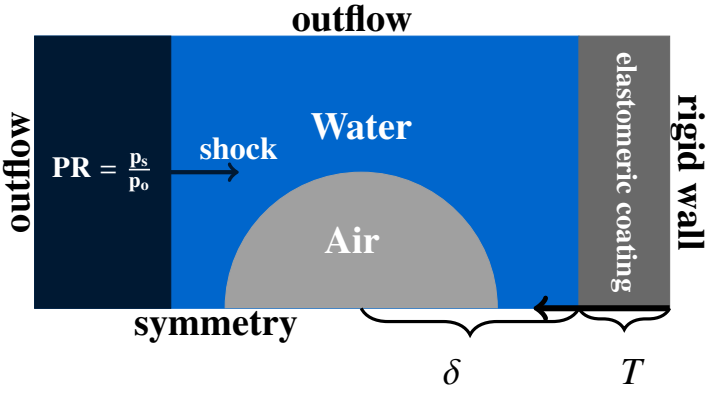

Figure 6.1: Problem set-up for the shock-induced collapse of an initially cylindrical gas bubble near an elastomeric coating. The coordinate system origin is set at the rigid wall (black arrow).

the resolution of 672×384 corresponding to 128 cells per initial bubble radius. The Noble-Abel Stiffened Gas equation of state is used to model the materials and properties used for this section and §6.3 are summarized in Table 6.1.

6.2.2 Results

Fig. 6.2 shows different contours of the bubble collapsing and its interaction with an elastomeric coating (polyurea in this instance). In the first frame (frame a), the right-moving shock has interacted with the bubble. Due to the air being acoustically softer than water, the shock is partially reflected as a rarefaction wave and partially transmitted as a shock into the bubble. The shock then interacts with the elastomeric coating as the bubble begins to collapse (frame b). Due to the acoustic impedance mismatch between the water and the elastomeric coating, a portion of the in-

Table 6.1: Material properties corresponding to the materials used for simulations of shock-induced bubble collapse near an elastomeric object described by the stiffened-gas EOS.

Property	Air	Water	Polyurea
n	1.4	2.35	2.35
B [Pa$\times 10^9$]	0	0.7	2.1
b [m^3/kg$\times 10^{-4}$]	0	6.61	0
c [kJ/kg K]	0.718	1.816	4.34
q [kJ/kg]	0	-1.18	-1.17

coming shock is reflected towards the bubble as a shock and part is transmitted into the elastomeric coating. The transmitted shock is subsequently reflected by the wall towards the bubble, thus doubling the pressure. As the bubble collapses, the transmitted and reflected shock interacts with the bubble, thus enhancing the collapse (frame c). The surrounding water and elastomeric coating are entrained by this converging flow (frame d). The bubble collapses forming a re-entrant jet towards the elastomeric coating (frame e). An outward propagating water-hammer shock is emitted into the surroundings and interacting with elastomeric coating (frames e and f). After its collapse, the bubble takes the form of a pair of lines converging towards the wall and further deforms the elastomeric coating (frame f).

We first investigate the wave dynamics due to the coating by simulating the 1D version of the problem in Fig. 6.1 without the bubble. Fig. 6.3 shows the X-T diagram for the shock wave interacting with elastomeric coating and rigid wall for the domain in Fig. 6.1 without the bubble. For comparison, the X-T diagrams of the baseline configuration with the rigid wall located at H = δ + T and H = δ are also presented. The shock wave-coating-rigid wall configuration shows the partially reflected and partially transmitted wave from the shock-coating interaction and the transmitted wave reflection from the rigid wall. For the baseline configuration with the rigid wall at H = δ + T, the shock is reflected from the rigid wall later in time relative to the shock wave-coating-rigid wall configuration. This is due to the shock wave propagating faster in the coating given its higher sound speed than water. For the baseline case with the rigid wall at H = δ, the reflected shock reflects from the rigid wall and has the same trajectory as the partially reflected shock wave in the shock wave-coating-rigid wall configuration.

To investigate the bubble dynamics, the quantities of interest are the re-entrant jet velocity and bubble volume at collapse. Both quantities are measures of the strength of the outward-propagating water-hammer shock wave that interacts with the rigid wall. The shock wave then produces maximum pressures on the wall which are representative of the impact loads leading to material loss and pitting (Kim *et al.*, 2014). Fig. 6.4 shows the maximum bubble jet velocities normalized by the characteristic speed, i.e., $\sqrt{\frac{\Delta p}{\rho_l}}$, defined by Plesset & Chapman (1971) based on the initial distance

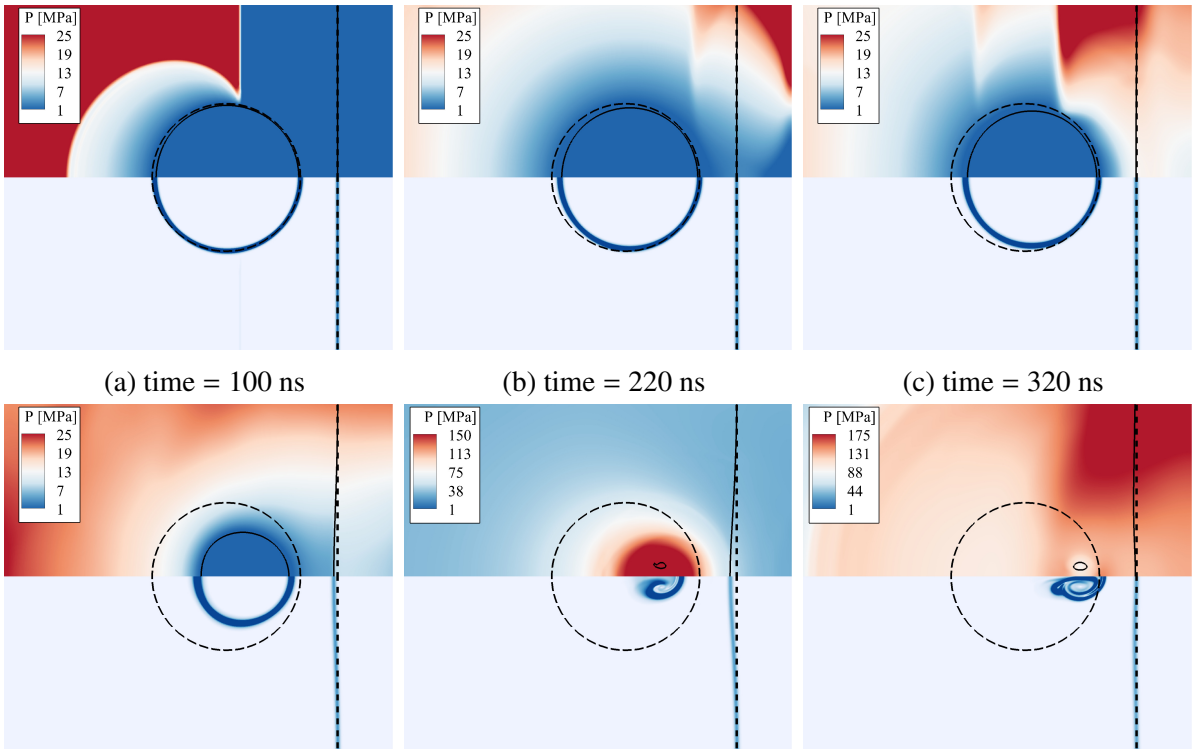

(a) time = 100 ns (b) time = 220 ns (c) time = 320 ns

(d) time = 640 ns (e) time = 880 ns (f) time = 1.06 μs

Figure 6.2: Pressure (top) and numerical Schlieren (bottom) contours for the 2D shock-induced bubble collapse near an elastomeric coating. Contour lines represent the material interface approximate locations. Black dotted line represents the initial bubble location.

to the rigid wall, H, and initial distance to the nearest object, δ. For the same initial distance to the rigid wall, the bubble re-entrant jet velocities are higher with the coating relative to without the elastomeric coating. However, since the partially reflected shock wave interacts with the bubble in a similar fashion as the $H = \delta$ case in Fig. 6.3, the bubble dynamics are expected to exhibit the same behavior when considering the distance to the nearest object, i.e., δ as shown in the second subfigure of Fig. 6.4. As the bubble's initial location is closer to the nearest boundary, the maximum re-entrant jet velocity approach similar values. The slope of the maximum re-entrant jet velocities for the problem with the coating is steeper than those of the baseline configuration. While further investigation is needed, it is expected that as the bubble is initially placed farther away from the coating, the trailing rarefaction waves behind the reflected shocks that interact with the bubble (see frame c in Fig. 6.2) inhibit the re-entrant jet formation more than the case without the elastomeric coating.

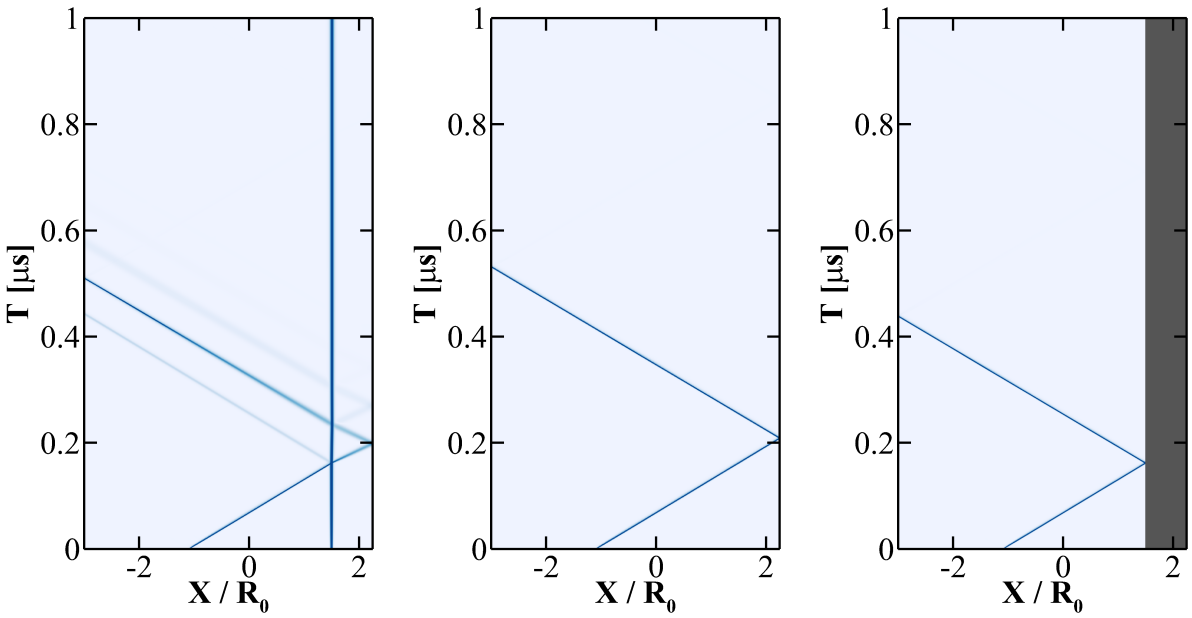

(a) Shock-coating-wall. (b) Shock-wall, H = δ + T. (c) Shock-wall, H = δ.

Figure 6.3: X-T diagrams for a shock-wall interaction with and without the coating in the absence of the bubble.

The bubble volumes at collapse for the baseline and elastomeric coating configurations are shown in Fig. 6.5. For both configurations, as the bubble is initialized closer to rigid wall, the bubble volume at collapse increases. For the baseline configuration, trailing rarefaction waves from the reflected shocks inhibit the bubble collapse until the cases where the bubble is placed $H/R_o <$ 1.125. For these cases, the bubble volume decreases. For the elastomeric coating configuration, the minimum bubble volume is further inhibited by the elastomeric coating's elasticity resisting the entrainment of fluid as the bubble collapses. However, when considering the closest boundary (δ), the minimum bubble volumes are less than those of the exhibited for the baseline configuration. This is attributed to the partially transmitted wave into the elastomeric coating and subsequently reflected from the rigid wall towards the bubble later in time, relative to the baseline configuration, and furthering the collapse of the bubble.

The maximum pressures exhibited in the surrounding water and at the wall are shown in Figs. 6.6 and 6.7, respectively. The maximum pressures are normalized by the characteristic water-hammer pressure defined by Plesset & Chapman (1971), i.e., $\rho_l a_l \sqrt{\frac{\Delta p}{\rho_l}}$, where ρ_l is the water den-

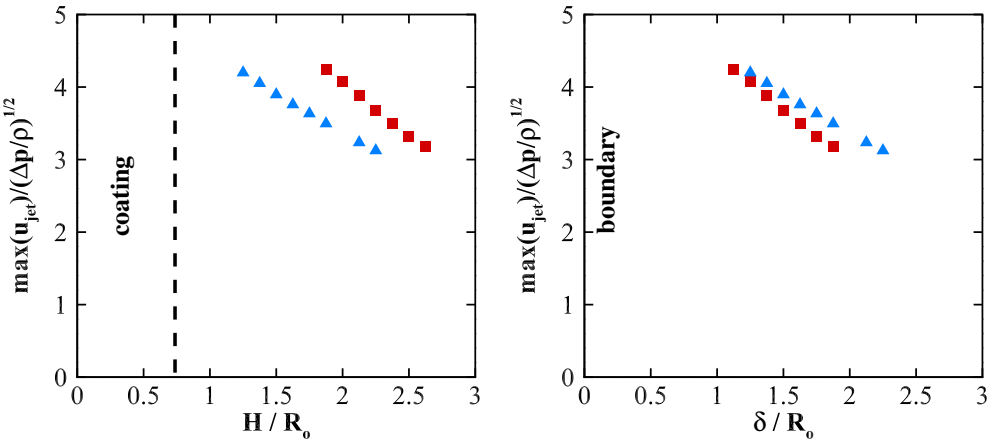

(a) H dependence. (b) δ dependence.

Figure 6.4: Maximum bubble jet velocities for different initial bubble stand-off distances from the rigid wall (left) and nearest object (right) for a 2D shock-induced bubble collapse without (blue triangles) and with an elastomeric coating (red squares).

sity, a_l the water sound speed, and $\Delta p = p_s - p_o$. Fig. 6.6 shows the maximum pressures in the surrounding water from the water-hammer shock for the initial bubble stand-off distances relative to the rigid wall and the nearest object. For $\delta/R_o > 1.5$, the maximum pressure exhibited in the water from the water-hammer shock with the coating approaches the baseline configuration values as the effect of the reflected incident wave diminishes. For $\delta/R_o < 1.5$, the exhibited maximum pressures for the baseline configuration increase due to the incident shock wave reflecting from the rigid wall increasing the bubble re-entrant jet velocity and decreasing the bubble volume at collapse (see Figs. 6.4 and 6.5). Despite the bubble re-entrant jet velocity increasing as the initial bubble location approaches the elastomeric coating, the elastomeric coating's elasticity inhibits the bubble collapse volume as seen in Fig. 6.5 resulting in a relatively constant maximum pressure exhibited in the water due to the water-hammer shock. For Fig. 6.7, the location of the bubble collapse is considered instead of the initial bubble location since an expected $\sim 1/r$ trend for the maximum pressure exhibited at the wall as shown in Chapter 4 and in Beig *et al.* (2018). For the baseline configuration, the expected result is achieved with the maximum wall pressures increase as the bubble collapses closer to the wall. The maximum wall pressures for the elastomeric coating configuration exhibit similar values as those with the coating, however, the slope of the trend is

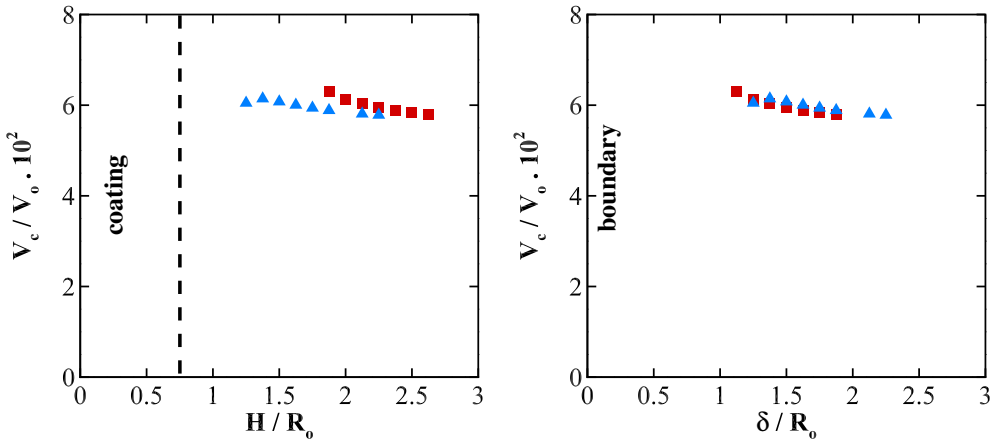

(a) H dependence. (b) δ dependence.

Figure 6.5: Bubble collapse volume for different initial bubble stand-off distances from the rigid wall (left) and nearest object (right) for a 2D shock-induced bubble collapse without (blue triangles) and with an elastomeric coating (red squares).

lower than without the coating. This result is attributed to the relatively constant maximum pressures water-hammer pressures in the liquid due to the elastomeric inhibiting the bubble collapse (see Fig. 6.7). Moreover, Fig. 6.8 shows the maximum wall pressures with varying elastomeric coating thickness while keeping $\delta = 1.5$. As the elastomeric coating thickness, the maximum wall pressure increases; however, the effect is minimal. Further investigations would be needed increasing the coating's elasticity to determine the bubble collapse dependence the elasticity and resulting maximum wall pressures with the elastomeric coating.

6.3 Collapse of a Bubble Pair Near an Elastomeric Coating

6.3.1 Problem Set-up

Although single-bubble collapse is a valuable canonical problem, cavitation erosion most commonly occurs due to the collapse of bubble clouds. Thus, understanding how interactions between the bubbles affect the dynamics as well as the mechanical loads are produced on neighboring objects. At the present time, capturing the detailed bubble-bubble interactions is beyond the reach of even the most sophisticated cloud models (Fuster & Colonius, 2011), particularly if the bubble

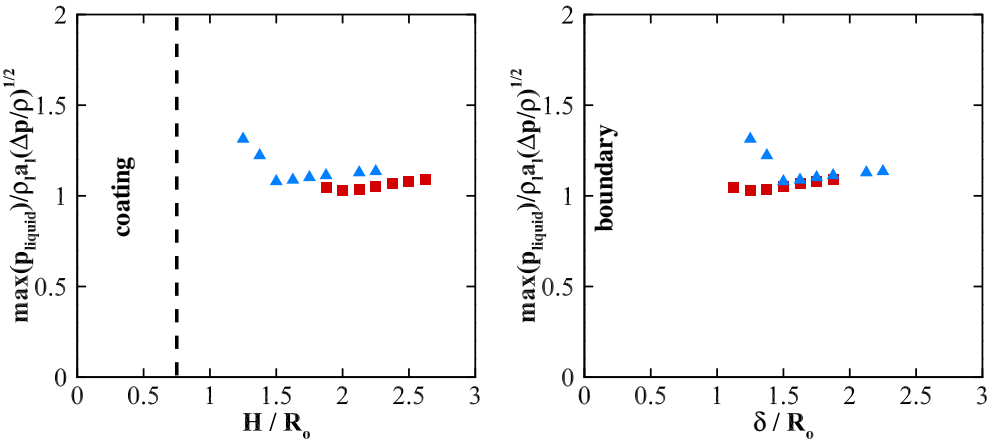

(a) H dependence. (b) δ dependence.

Figure 6.6: Maximum water pressure for different initial bubble centroid stand-off distances from the rigid wall (left) and nearest object (right) for a 2D shock-induced bubble collapse without (blue triangles) and with an elastomeric coating (red squares).

dynamics are non-spherical. To investigate the effects of the presence of a second nearby bubble, we perform 2D simulations of a bubble pair collapsing near a compliant surface. Fig. 6.9 shows the problem setup. Two initially cylindrical air bubbles are in water with the primary bubble located a distance δ away from the elastomeric coating of thickness T. As in §6.2, $T/R_o = 0.75$ and $\delta/R_o = 1.5$. The secondary bubble is an initial distance D from the primary bubble with an angle ϕ between the line that connects the bubbles' initial centroids and the horizon. For simplicity, we consider the bubble pair to be monodisperse (same radii) with $R_o = 500$ μm and one initial distance, $D/R_o = 2.5$. Only ϕ is varied in this study as it presents the most distinct initial bubble pair configurations, and therefore bubble collapse dynamics, relative to varying D. Ambient temperature $300K$ is used and the Rankine-Hugoniot conditions are used to initialize the shock. The post-shock pressure is p_s, ambient pressure p_o and PR $= p_s/p_o = 300$. Two media are considered for the compliant object: (i) water as a baseline case and (ii) polyurea, an elastomeric material. The elastomeric coating is modeled as a Kelvin-Voigt solid using the properties of polyurea, an elastomeric material, using the stiffened-gas equation of state as described in §6.2 with the material properties in Table 6.1. We have a uniform Cartesian grid with a resolution that varies with ϕ such that there is 96 cells per initial bubble radius, for example, the $\phi = 45°$ case has a resolution

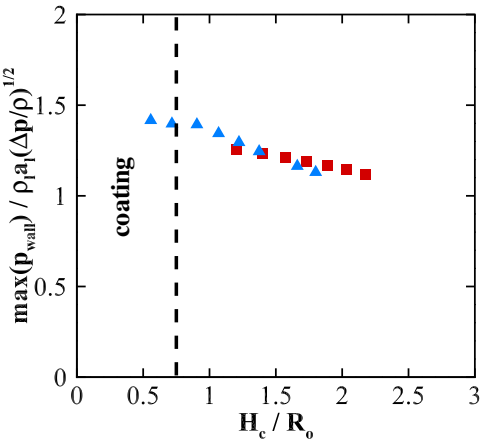

Figure 6.7: Maximum wall pressure for different initial bubble centroid stand-off distances from the rigid wall (left) and nearest object (right) for a 2D shock-induced bubble collapse without (blue triangles) and with an elastomeric coating (red squares).

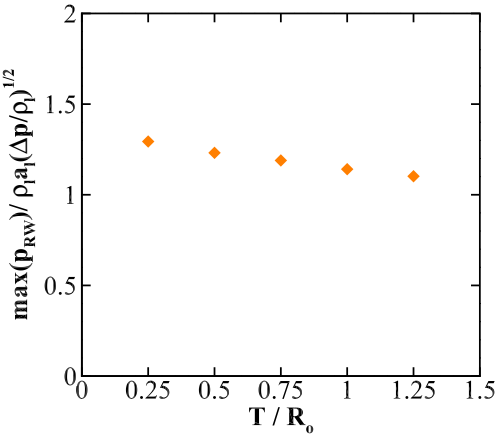

Figure 6.8: Maximum wall pressure for different elastomeric coating thicknesses with $\delta = 1.5$ for a 2D shock-induced bubble collapse.

of 673×745.

6.3.2 Results

Fig. 6.10 shows contours of shock-induced collapse of a bubble pair for the case with $\phi = 45°$. The right-moving shock interacts with the two bubbles. First, the incident shock wave interacts with the secondary and primary bubbles. Due to the acoustic impedance mismatch between water and air, the shock wave is partially transmitted as a shock wave into the bubbles and partially reflected into the surroundings as rarefaction waves (frame a). Additionally, the incident shock wave

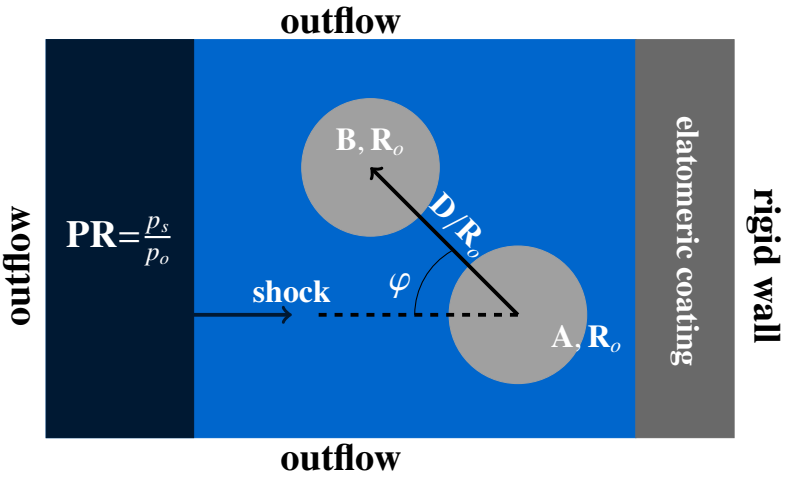

Figure 6.9: Problem set-up for the shock-induced collapse of a pair of initially cylindrical gas bubbles near an elastomeric coating.

interacts with the elastomeric coating. Since the elastomeric coating is acoustically stiffer than water, the shock wave is partially transmitted and partially reflected as shock waves. The partially transmitted shock wave is then reflected from the rigid wall and doubles in strength as the primary and secondary bubbles begin to collapse (frame b). The secondary bubble collapses and produces a re-entrant jet directed towards the primary bubble (frames c and d). Upon impact of the re-entrant jet with the distal side, the secondary bubble emits an outward-propagating water-hammer shock (frame d) and becomes a distorted pair of vortex lines that convects towards the primary bubble (frames e and f). Due to its farther initial distance from the incident shock relative to the secondary bubble, the collapse of the primary bubble takes place after the secondary bubble (frames a-d). Two re-entrant jets form during collapse due to the combined interaction with the primary bubble and the wall (frame e). The primary bubble's resulting re-entrant jet is at approximately 45^o from the horizontal. These results are consistent with bubble pairs collapsing near a perfectly rigid wall (Alahyari Beig, 2018). The primary bubble's emitted water-hammer shock is substantially stronger than that of the secondary bubble (frame e). For the elastomeric coating, the primary bubble's pair of vortex lines convects toward the coating and its impingement on the coating causes the deformation (frame b). The primary bubble's water-hammer shock is partially transmitted into the elastomeric coating (frame e). This water-hammer shock is then reflected from the perfectly rigid

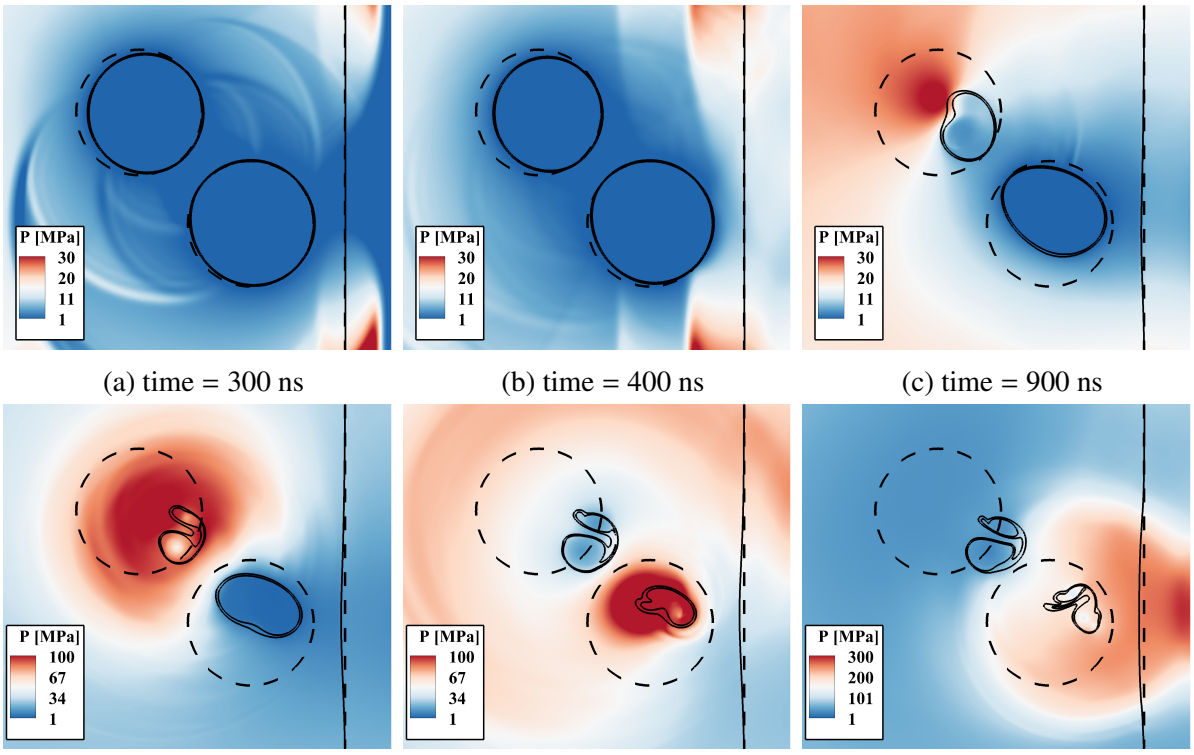

(a) time = 300 ns (b) time = 400 ns (c) time = 900 ns

(d) time = 1.1 μs (e) time = 1.2 μs (f) time = 1.3 μs

Figure 6.10: Pressure (top) and numerical Schlieren (bottom) contours for the 2D shock-induced collapse of an initially single bubble near an elastomeric coating. Contour lines represent the material interface approximate locations. Black dotted lines represent the initial bubble locations.

wall and doubles in strength (frame f). The reflected water-hammer shock (see frame f) would induce subsequent weaker collapses from the bubble pair. We note that the primary and secondary bubble collapses are different from the single bubble case as both bubbles had re-directed re-entrant jets during collapse enhancing the strength of the emitted water-shocks. Moreover, the deformation of the elastomeric coating is further sustained relative to the single bubble configuration. This is due to the primary bubble collapsing at angle and as opposed to convecting towards the coating in the normal direction and thereby deforming the coating towards its original configuration.

In the context of naval hydrodynamic cavitation-induced damage, the quantity of interest is the maximum pressures exhibited in the elastomeric coating. Pressures being representative of the impact loads that lead to pitting and material loss (Kim *et al.*, 2014). The maximum pressures as a function of ϕ are presented in Fig. 6.11 for the baseline configuration (water) and the elastomeric coating configuration. For comparison, the maximum wall pressure from the single

bubble-elastomeric coating configuration with $\delta = 1.5$ is also presented. For $\phi = 90°$, the bubble pair is aligned such that the incident shock wave interacts with the bubbles at the same time. Thus, the bubbles collapse is synchronized and the outwardly propagating water-hammer shocks are reflected from the rigid wall and exhibit a similar value as the single bubble collapse value for the baseline and elastomeric coating configurations. For $\phi < 90°$, the incident shock wave and bubble pair interaction is desynchronized with the shock wave inducing the collapse of the secondary bubble before the primary bubble (see Fig. 6.10 for the $\phi = 45°$ example). While the partially reflected shock wave from the incident shock-elastomeric coating interaction interacts with the bubble pair (see frame b in Fig. 6.10), the effect is minimal compared to the outward-propagating water-hammer shock wave from the secondary bubble interacting with the primary bubble. As a result, the secondary bubble collapses first and the emitted outward-propagating water-hammer further strengthens the collapse of the primary bubble resulting in a higher maximum wall pressure. For all ϕ, the baseline case (water case) exhibits a higher maximum wall pressure than the elastomeric coating case, this result is expected due to primary bubble's outward-propagating water-hammer shock wave being (i) partially transmitted into the coating due to the impedance mismatch between the elastomeric coating water and (ii) dampened from propagating the additional distance of the coating thickness. Although this is a preliminary study, we have gained insights on the synchronization and bubble collapse enhancement based on the bubble pair's initial spatial configuration. This result suggests a mechanism for permanently deformation of the coating (e.g., pitting (Kim *et al.*, 2014)) via the collapse of bubble pairs. More detailed studies will be needed to further characterize the sustained deformation dependence on the inter-bubble pair distance D and angle ϕ.

6.4 Conclusions

To provide a better understanding of cavitation erosion, we conducted numerical simulations of 2D shock-induced collapse of an initially cylindrical gas bubble near an elastomeric coating for

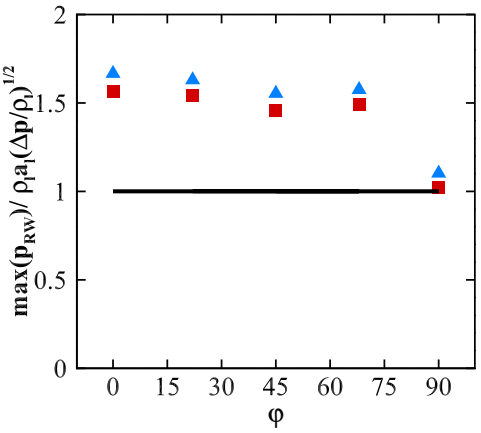

Figure 6.11: Maximum wall pressure for different bubble-bubble angles from the horizontal without (blue triangles) and with (red squares) the elastomeric coating with $\delta = 1.5$. Solid black line is the single bubble shock-induced collapse elastomeric configuration value for $\delta = 1.5$.

different geometrical configurations. We investigated the detailed flow physics of the problem with an emphasis on wave propagation and viscoelastic effects for bubble collapse near an elastomeric coating. The acoustic impedance mismatch between the surround fluid and elastomeric coating led to a higher re-entrant jet velocity relative to the water case surrounding the bubble. Soon afterwards, the collapse is further strengthened by the shock wave that was reflected from the perfectly rigid wall. The synchronization and amplification of these two shock waves depends on the elastomeric coating thickness and initial bubble radius. The initial deformation is due to conservation of mass as the bubble entrains the surroundings as it collapses. The re-entrant jet and convecting pair of vortex lines then contributes to the material returning to its original state. Additionally, we simulated the shock-induced collapse of a bubble pair near an elastomeric coating. We demonstrated that strong bubble-bubble interactions may significantly affect the dynamics of the flow: amplify pressures produced at the collapse. As a result, the elastomeric coating deformation from the surface was significantly larger and more sustained than the single bubble case. Future parametric studies will enable further modeling efforts for polydisperse and monodisperse bubble clouds near compliant objects and elastomeric coatings and similar soft materials.

CHAPTER 7

Conclusions

This chapter summarizes the research objectives, contributions to the field, and future research directions.

7.1 Summary

The two objectives of this thesis were: (i) to develop a high-order accurate, interface-capturing compressible multiphase numerical model with linear viscoelasticity to study flows at all speeds and involving non-spherical bubble dynamics, and (ii) to better understand cavitation damage by investigating bubble collapse dynamics and neighboring rigid/soft objects for confined cavitation, ultrasound-induced cavitation, and cavitation in naval engineering applications. The following is a summary of Chapter 2 through 6 in the thesis.

Two contributions were made to the field in achieving the first objective.

1. We introduce a novel Eulerian approach for numerical simulations of wave propagation in heterogeneous viscoelastic media, with application to compressible materials described by linear constitutive relations, specifically Maxwell, Kelvin-Voigt or generalized Zener models Rodriguez & Johnsen (2018).

2. We extended our numerical approach to the AUSM scheme which is capable of handling all speed flows Rodriguez *et al.* (2018).

This numerical framework is then leveraged to study three thematic areas of cavitation damage of interest and achieve our second objective:

1. We conducted numerical computations to gain fundamental quantitative insights on the effect of confinement for an inertially collapsing bubble in a channel. The bubble centroid initial location within the channel, driving pressure, and channel width were varied.

2. To gain insights into the cavitation erosion mechanisms in extracorporeal shock wave lithotripsy, we conducted numerical simulations of 2D shock-induced collapse of an initially cylindrical gas bubble near a model kidney stone. We validated our numerical framework for shock-induced bubble collapse problems with 2D experimental results. The wave and bubble dynamics were characterized for various model stone sizes and initial bubble stand-off distances from the stone.

3. We conducted 2D shock-induced collapse of gas bubbles near an elastomeric coating for different configurations to understand cavitation-induced damage relevant to naval engineering applications. The shock-induced collapse of a single bubble and a bubble pair near an elastomeric coating are considered for different initial geometric configurations. We investigated the detailed flow physics with an emphasis on wave propagation and viscoelastic effects.

7.2 Conclusions

The following conclusion are drawn for Chapter 2 through 6:

1. We developed an Eulerian approach for numerical simulations of wave propagation in heterogeneous viscoelastic media (Rodriguez & Johnsen, 2018), that is suitable to investigate problems involving cavitation-induced damage. Our numerical framework is explicit in time and space, and high-order accurate. The spatial scheme is based on a solution-adaptive approach, where central differences are used in smooth regions and high-order shock capturing at discontinuities (material interfaces, contacts and shocks). We verified the method using a

stringent suite of test problems involving smooth wave, shock, shear and contact waves problems in viscoelastic media. The spatial scheme is based on a solution-adaptive formulation, in which a discontinuity sensor discriminates between smooth and discontinuous regions. To compute the convective fluxes, explicit high-order central differences are applied in smooth regions, while a high-order finite-difference Weighted Essentially Non-Oscillatory (WENO) scheme is used at discontinuities (shocks, material interfaces and contacts). At least fourth-order accuracy is achieved in smooth problems, and the correct wave speeds are obtained. Eigenanalysis confirms that our Lie derivative implementation yields correct results. Spurious pressure and temperature errors at interfaces were shown to be prevented, and all wave families are accurately represented. The method is verified using a stringent suite of 1D and 2D test problems involving smooth wave, shock, shear and contact waves problems in viscoelastic media. Overall, we developed and verified a robust framework to compute fully coupled fluid-solid problems viable for studying cavitation-induced damage.

2. We extended the abilities of our novel approach (Rodriguez & Johnsen, 2018) by using the AUSM scheme (Rodriguez *et al.*, 2018). Our approach introduces elastic stresses in the convective fluxes that are treated by generalizing AUSM flux-vector splitting (FVS) to account for the Cauchy stress tensor. The approach provides a paradigm on how to develop FVS schemes for physical models that exhibit traits to those of linear viscoelasticity. Prior to this work, the five-equation multiphase model or viscoelasticity had yet to be implemented into flux-vector splitting (FVS) schemes such as AUSM. Multiphase FVS schemes were primarily used for solving the compressible Euler equations with the six-equation multiphase model. The generalization of AUSM to account for the Cauchy stress tensor appearing in the viscoelastic description was a novel development for FVS schemes. We determine an appropriate discretization of non-conservative equations that appear in the five-equation multiphase model with AUSM schemes to prevent spurious oscillations at material interfaces. Moreover, the discretization we obtained is the same for other FVS schemes. The framework's spatial scheme is solution-adaptive with a discontinuity sensor discriminating

between smooth and discontinuous regions. The smooth regions are computed using explicit high-order central differences. At discontinuities (i.e., shocks, material interfaces and contacts), the convective fluxes are treated using a high-order WENO scheme with AUSM$^+$-up for upwinding. This numerical approach is a preferred approach given its ability to compute flows at all speeds which is not straightforward for finite-difference schemes (FDS) schemes. The framework is used to simulate 1D and 2D problems that demonstrate the ability to maintain equilibrium interfacial conditions and solve challenging multi-dimensional and multi-material problems.

3. We gained fundamental quantitative insights into the effect of confinement for an inertially collapsing bubble in a channel. Differences observed in the bubble migration distance and volume at collapse between the single wall and channel wall configuration. For $x_{C0} = 0$, channel configuration exhibits the smallest volume due to the impingement of two re-entrant jets increasing the bubble compression and intensifying the collapse. At $x_{C0} = 0.5$, an inversion of the minimum bubble volume at collapse between the channel and single wall configures was observed. This was attributed to the trapped rarefaction waves (tension) in the channel decreasing the inertia (compression) driving the collapse. We observed that other than for the case where the bubble was initially in the center of the channel, the bubbles collapsed in a similar asymmetric fashion as that of a single wall configuration. Moreover, as the bubble was initialized closer to the right wall, the bubble centroid migration for the channel converged to the single wall values. The maximum pressures along the right wall exhibited similar trends as those of the single wall configuration; thus, the scaling developed by Beig *et al.* (2018) holds for the channel configuration. This indicates that the confinement plays a limited role in inertially collapsing bubbles in channel to the extent that the dynamics are relatively similar to the single wall configuration. Additionally studies of more confined configurations may be needed, e.g., bubbles attached to the right wall, two bubbles in the channel, to determine if the dynamics deviate from their single wall counterparts. For widths $W > 8 \times R_0$, the effect of confinement diminishes and approaches the single wall

configuration values.

4. Numerical simulations of shock-induced bubble collapse near a kidney stone were used to determine the the mechanisms involved stone comminution with a neighboring cavitation bubble. Three events were identified where a local maximum principal stress in tension was produced in the stone: (i) along the surface of the stone as the incident shock wave interacts with the stone, (ii) on the stone's side facing the cavitation bubble from the bubble's emitted water-hammer shock, and (iii) on the distal side of the stone relative to the bubble from the reflected water-hammer shock becoming a tensile wave. These local maximum tensile stress appeared descending in magnitude with the incident shock response being the strongest. We observed an increase in the maximum tensile principle stress depends on the model stone size with no appreciable gain observed for stones with radii $R_s < 4 \times R_a$, where R_a is the bubble radius. The gain was found to be insensitive to initial bubble stand-off distance from the stone. These results support, in part, the three-stage process of kidney stone comminution process detailed in Johnsen & Colonius (2009b). In this process, the shock wave leads the kidney stone comminution process for larger stones (i.e., $R_s > 2$ mm). The insight gained in this work is that cavitation bubbles near the kidney stones amplify the potential for spallation from the shock wave. For smaller stones, the potential for spallation via shock wave diminishes. In these instances, the cavitation damage (e.g., the re-entrant jet) dominate the kidney stone comminution.

5. The 2D numerical simulations of shock-induced collapse of gas bubbles near an elastomeric coating for different configurations provided valuable insights on cavitation-induced damage mechanisms for elastomeric coatings. The single bubble case demonstrated that both the acoustic impedance and elastomeric coating's thickness determine the bubble dynamics and the impact loading and deformation of the coating. Due to the acoustic impedance mismatch between the liquid and coating, the partially reflected shock wave from the incident shock/elastomeric coating interaction led to a higher re-entrant jet velocity relative

to the water only case. Soon afterwards, the collapse is further strengthened by the shock wave that was reflected from the perfectly rigid wall. The synchronization and amplification of these two shock waves depends on the elastomeric coating thickness and initial bubble radius. Additional studies will be needed to characterize the synchronization/amplification dependence on ratio of coating thickness to bubble radius ratio T/R_o. The initial deformation is due to conservation of mass as the bubble entrains the surroundings as it collapses. The re-entrant jet and convecting pair of vortex lines then contributes to the material returning to its original state. In the bubble pair case, we observed bubble-bubble interactions significantly affecting the dynamics of the flow: amplify pressures produced in the elastomeric coating. For centroid-to-centroid angles of the bubble pairs from the horizon $\phi < 90^o$, a desynchronization of the bubble pair collapses was observed. The desynchonization resulted in higher maximum wall pressures relative to the comparable single bubble shock-induced bubble collapse value. For $\phi = 45^o$, the desynchronization involved two re-entrant jets forming in the primary bubble significantly amplifying the collapse strength after the secondary bubble collapsed. Additionally, the primary bubble's re-entrant jet was redirected at an angle towards the wall due to the fluid entrainment from the secondary bubble's collapse. As a result, the elastomeric coating deformation from the surface was significantly larger and sustained than the single bubble case. This result suggests a mechanism for permanently deformation of the coating (e.g., pitting) via the collapse of bubble pairs. More detailed studies will be needed to further characterize the sustained deformation dependence on the inter-bubble distance D and angle ϕ.

7.3 Future Research Directions

7.3.1 Physical and Numerical Model

The physical model is limited to infinitesimally small strains and neglects surface tension and mass transfer. The hypoelastic framework using the Lie derivative has been shown to be consistent with

hyperelastic constitutive relations (e.g., Neo-Hookean) and the approach of Altmeyer *et al.* (2015) could be incorporated into the current numerical model. Doing so would enable cavitation damage investigations studies involving materials undergoing finite deformations. While the numerical models for the Godunov-based Eulerian physical model discussed in Chapter 2 are in their infancy this approach has potential long-term advantages. Viscoelastic constitutive relations for non-linear finite deformations and non-linear stress relaxation, e.g., the popular model of Bernstein *et al.* (1963), are well-suited for this physical model as they are effective in modeling elastomeric materials in a hyperelastic framework. Moreover, there have been efforts incorporating stress relaxation using Godunov-approach (Ndanou *et al.*, 2015).

Mass transfer (e.g., the evaporation and condensation in the gas bubble) is important during the collapse and rebound of the bubble. To incorporate mass transfer and phase change, the approach of Pelanti & Shyue (2014) could be followed with the current physical model. Surface tension is important when considering non-spherical perturbations at bubble interfaces and bubble oscillations prior to collapse. To incorporate surface tension, the approach of Schmidmayer *et al.* (2017) could also be incorporated into the physical and numerical model.

7.3.2 Numerical Methods and Computation

The current solver incorporating the high-order multiphase framework with linear viscoelasticity is limited to 2D calculations. However, the solver of Alahyari Beig & Johnsen (2015) used in Chapter 3 could be extended to incorporated linear viscoelasticity with the appropriate algorithmic modifications.

The extension of the numerical model with AUSM$^+$-up is numerically stiff when incorporating the source term in the non-conservative volume fraction equation in the five-equations model. Future numerical analysis will be needed to identify and, if possible, alleviate this issue. An avenue to pursue is analytically demonstrating the numerically consistent approach to calculate both the speed of sound for upwinding and incorporating the source term.

When the bubble collapses to a volume typically four orders of magnitude lower than the initial

volume, significant resolution is needed with a fixed mesh to resolve the late-time collapse small-scale features. The calculations typically need mesh resolutions over 100 computational cells per initial bubble radius to achieve grid convergence with a high-order scheme (Beig *et al.*, 2018). Moreover, the solution-adaptive approach leads to a computational workload imbalance during the later stages of the bubble collapse. The processors solving the flow where the bubble is located typically require an order of magnitude more operations as more cells are flagged to utilize the high-order accurate method. Utilizing Adaptive Mesh Refinement (AMR) techniques could be a viable way to address both the workload imbalance issue and limitations in resolving small-scale features. AMR is advantageous on increasing the resolution only where needed and the high-order accurate AMR approach of Shen *et al.* (2011) could be incorporated into the numerical solver. Understandably, the load imbalance issue may still persist but it would be reduced relative to the current solution-adaption approach.

7.3.3 Physical Investigations

Our studies explored wave and bubble dynamics for certain range of material properties (e.g., gas in bubble, shear modulus) and geometries (e.g., confinement ratio and model stone to bubble size ratio). In Chapter 4, the maximum wall pressures in the confinement problem appeared to collapse to the same curve as those as the values obtained for the single wall configuration. Additional parametric investigations with higher confinement ratios and bubbles attached to the wall are needed to determine if confinement has an effect on the maximum wall pressures relative to those exhibited for the single wall configuration. In Chapter 5, the stone-bubble size ratios considered were of order $\mathscr{O}(10^0)$ such that stones were small enough that bubble-lithotripsy shock wave interactions were significant. Investigations with relevant lithotripsy waveforms are needed to further explore the bubble-shock wave interactions during the comminution of stones with $\sim 10 - 15$ mm diameters (Cleveland & Sapozhnikov, 2005). Moreover, the results are expected to change for 3D simulations as the incident wave, depending on the model kidney stone size and shape, can be highly focused within the stone. In Chapter 6, the properties of polyurea were used to represent the

elastomeric coating and the elasticity of the coating inhibited the bubble collapse. However, similar maximum wall pressures were exhibited for configurations with and without the elastomeric coating. Different elastomeric material (with different shear moduli) properties and coating thicknesses would need to be considered to further characterize the effect of the coating's elasticity on the maximum wall pressures. Moreover, considering different size ratios for the bubble pair would further modeling efforts of bubble clouds near elastomeric coatings.

Two emerging areas of interest to pursue with this work are (i) high-strain rate rheometry of soft matter and (ii) damage mechanisms from high-amplitude wave propagation in soft tissue. Significant advances have been made in modeling a spherically collapsing bubble in viscoelastic media (Warnez & Johnsen, 2015; Gaudron *et al.*, 2015). The work of Estrada *et al.* (2017) demonstrates the potential of utilizing cavitation bubble dynamics to characterize soft matter in the high-strain rate regime. These efforts are currently limited to idealized conditions where the bubble collapses spherically. The numerical framework in this thesis could provide a valuable computational tool to complement experiments. Moreover, it would enable the study of asymmetrical bubble collapses in soft matter, the non-spherical perturbations, and re-entrant jet formation.

The damage/injury mechanisms due to high-frequency or high-amplitude waves (e.g., ultrasound, shocks/blasts) in soft tissue is not well understood. An example of this is lung hemorrhaging due to diagnostic ultrasound (Child *et al.*, 1990). Recent investigations using computational fluids dynamics (Patterson & Johnsen, 2018) have demonstrated how baroclinic vorticity distorts the material interface. This deformation is hypothesized to potentially lead to damage. However, this approach uses an inviscid solver; and the extent to which viscoelasticity affects the tissue's response and deformations remains unknown. As an initial step, the strains necessary to initiate damage in soft matter could be infinitesimally small. The numerical framework in this thesis is could be used to investigate the role of linear viscoelasticity in soft matter damage.

BIBLIOGRAPHY

Abgrall, R. 1996. How to Prevent Pressure Oscillations in Multicomponent Flow Calculations: A Quasi Conservative Approach. *J. Comput. Phys.*, **125**, 150–160.

Alahyari Beig, S. 2018. *A Computational Study of the Inertial Collapse of Gas Bubbles Near a Rigid Surface*. Ph.D. thesis, University of Michigan, Ann Arbor.

Alahyari Beig, S., & Johnsen, E. 2015. Maintaining interface equilibrium conditions in compressible multiphase flows using interface capturing. *J. Comput. Phys.*, **302**, 548–566.

Alahyari Beig, S., Rodriguez, M., & Johnsen, E. 2016. Non-spherical bubble collapse near rigid and compliant surfaces. *In: 31st Symp. Nav. Hydrodyn.*

Allaire, G., Clerc, S., & Kokh, S. 2002. A Five-Equation Model for the Simulation of Interfaces between Compressible Fluids. *J. Comput. Phys.*, **181**, 577–616.

Allen, J. S., & Roy, R. A. 2000. Dynamics of gas bubbles in viscoelastic fluids. II. Nonlinear viscoelasticity. *J. Acoust. Soc. Am.*, **108**, 1640–1650.

Altmeyer, G., Rouhaud, E., Panicaud, B., Roos, A., Kerner, R., & Wang, M. 2015. Viscoelastic models with consistent hypoelasticity for fluids undergoing finite deformations. *Mech. Time-Dependent Mater.*, **19**, 375–395.

Altmeyer, G., Panicaud, B., Rouhaud, E., Wang, M., Roos, A., & Kerner, R. 2016. Viscoelasticity behavior for finite deformations, using a consistent hypoelastic model based on Rivlin materials. *Contin. Mech. Thermodyn.*, **28**, 1741–1758.

Amini, M. R., Simon, J., & Nemat-Nasser, S. 2010. Numerical modeling of effect of polyurea on response of steel plates to impulsive loads in direct pressure-pulse experiments. *Mech. Mater.*, **42**, 615–627.

Ando, K., Colonius, T., & Brennen, C. E. 2013. Shock propagation in polydisperse bubbly liquids. *Bubble Dyn. Shock Waves*, **37**, 141–175.

Arienti, M., Hung, P., Morano, E., & Shepherd, J. E. 2003. A level set approach to Eulerian-Lagrangian coupling. *J. Comput. Phys.*, **185**, 213–251.

Baer, M., & Nunziato, J. 1986. A two-phase mixture theory for the deflagration-to-detonation transition (ddt) in reactive granular materials. *Int. J. Multiph. Flow*, **12**, 861–889.

Bahei-El-Din, Y. A., Dvorak, G. J., & Fredricksen, O. J. 2006. A blast-tolerant sandwich plate design with a polyurea interlayer. *Int. J. Solids Struct.*, **43**, 7644–7658.

Ball, G. J., Howell, B. P., Leighton, T. G., & Schofield, M. J. 2000. Shock-induced collapse of a cylindrical air cavity in water: a Free-Lagrange simulation. *Shock Waves*, **10**, 265–276.

Barton, P. T., Obadia, B., & Drikakis, D. 2011. A conservative level-set based method for compressible solid/fluid problems on fixed grids. *J. Comput. Phys.*, **230**, 7867–7890.

Barton, P. T., Deiterding, R., Meiron, D., & Pullin, D. 2013. Eulerian adaptive finite-difference method for high-velocity impact and penetration problems. *J. Comput. Phys.*, **240**, 76–99.

Barton, P. T., & Drikakis, D. 2010. An Eulerian method for multi-component problems in non-linear elasticity with sliding interfaces. *J. Comput. Phys.*, **229**, 5518–5540.

Barton, P. T., Drikakis, D., Romenski, E., & Titarev, V. A. 2009. Exact and approximate solutions of Riemann problems in non-linear elasticity. *J. Comput. Phys.*, **228**, 7046–7068.

Bécache, E., Ezziani, A., & Joly, P. 2005. A mixed finite element approach for viscoelastic wave propagation. *Comput. Geosci.*, **8**, 255–299.

Beig, S. A., Aboulhasanzadeh, B., & Johnsen, E. 2018. Temperatures produced by inertially collapsing bubbles near rigid surfaces. *J. Fluid Mech.*, **852**, 105–125.

Benjamin, T. B., & Ellis, A. T. 1966. The Collapse of Cavitation Bubbles and the Pressures thereby Produced against Solid Boundaries. *Philos. Trans. R. Soc. A Math. Phys. Eng. Sci.*, **260**, 221–240.

Bergeles, G., Li, J., Wang, L., Koukouvinis, F., & Gavaises, M. 2015. An Erosion Aggressiveness Index (EAI) Based on Pressure Load Estimation Due to Bubble Collapse in Cavitating Flows Within the RANS Solvers. *SAE Int. J. Engines*, **8**, 2276–2284.

Bernstein, B., Kearsley, E. A., & Zapas, L. J. 1963. A Study of Stress Relaxation with Finite Strain. *Trans. Soc. Rheol.*, **7**, 391–410.

Biçer, B., & Sou, A. 2016. Application of the improved cavitation model to turbulent cavitating flow in fuel injector nozzle. *Appl. Math. Model.*, **40**, 4712–4726.

Blake, J. R., & Gibson, D. C. 1987. Cavitation Bubbles Near Boundaries. *Annu. Rev. Fluid Mech.*, **19**, 99–123.

Blake, J. R., Taib, B. B., & Doherty, G. 1986. Transient cavities near boundaries. Part 1. Rigid boundary. *J. Fluid Mech.*, **170**, 479–497.

Blake, J. R., Taib, B. B., & Doherty, G. 1987. Transient cavities near boundaries Part 2. Free surface. *J. Fluid Mech.*, **181**, 197–212.

Blake, J. R., Robinson, P. B., Shima, A., & Tomita, Y. 1993. Interaction of two cavitation bubbles with a rigid boundary. *J. Fluid Mech.*, **255**, 707–721.

Bourne, N. K., & Field, J. E. 1992. Shock-induced collapse of single cavities in liquids. *J. Fluid Mech.*, **244**, 225–240.

Brennen, C. E. 2013. *Cavitation and Bubble Dynamics*. Cambridge: Cambridge University Press.

Brujan, E. A. 2004. The role of cavitation microjets in the therapeutic applications of ultrasound. *Ultrasound Med. Biol.*, **30**, 381–387.

Brujan, E. A., Keen, G. S., Vogel, A., & Blake, J. R. 2002. The final stage of the collapse of a cavitation bubble close to a rigid boundary. *Phys. Fluids*, **14**, 85–92.

Brujan, E.-A., Nahen, K., Schmidt, P., & Vogel, A. 2001. Dynamics of laser-induced cavitation bubbles near an elastic boundary. *J. Fluid Mech.*, **433**, 251–281.

Brujan, E.-A. A., Noda, T., Ishigami, A., Ogasawara, T., & Takahira, H. 2018. Dynamics of laser-induced cavitation bubbles near two perpendicular rigid walls. *J. Fluid Mech.*, **841**, 28–49.

Carcione, J. M. 1993. Seismic modeling in viscoelastic media. *Geophysics*, **58**, 110–120.

Carcione, J. M. 2014. *Wave Fields in Real Media, Third Edition: Wave Propagation in Anisotropic, Anelastic, Porous and Electromagnetic Media*. Third edn. Elsevier Science.

Chang, C.-H., & Liou, M.-S. 2003. A New Approach to the Simulation of Compressible Multifluid Flows with AUSM+ Scheme. *In: 16th AIAA Comput. Fluid Dyn. Conf.* Reston, Virigina: American Institute of Aeronautics and Astronautics.

Chang, C. H., & Liou, M. S. 2007. A robust and accurate approach to computing compressible multiphase flow: Stratified flow model and AUSM+-up scheme. *J. Comput. Phys.*, **225**, 840–873.

Child, S., Hartman, C., Schery, L., & Carstensen, E. 1990. Lung damage from exposure to pulsed ultrasound. *Ultrasound Med. Biol.*, **16**, 817–825.

Cleveland, R. O., & Sapozhnikov, O. A. 2005. Modeling elastic wave propagation in kidney stones with application to shock wave lithotripsy. *J. Acoust. Soc. Am.*, **118**, 2667–2676.

Coleman, A. J., Saunders, J. E., Crum, L. A., & Dyson, M. 1987. Acoustic cavitation generated by an extracorporeal shockwave lithotripter. *Ultrasound Med. Biol.*, **13**, 69–76.

Coralic, V., & Colonius, T. 2014. Finite-volume WENO scheme for viscous compressible multicomponent flows. *J. Comput. Phys.*, **274**, 95–121.

Crum, L. A. 1988. Cavitation Microjets as a Contributory Mechanism for Renal Calculi Disintegration in Eswl. *J. Urol.*, **140**, 1587–1590.

Dahake, G., & Gracewski, S. M. 1997a. Finite difference predictions of P-SV wave propagation inside submerged solids. I. Liquidsolid interface conditions. *J. Acoust. Soc. Am.*, **102**, 2138–45.

Dahake, G., & Gracewski, S. M. 1997b. Finite difference predictions of P-SV wave propagation inside submerged solids. II. Effect of geometry. *J. Acoust. Soc. Am.*, **102**, 2138–2145.

de Brauer, A., Iollo, A., & Milcent, T. 2016. A Cartesian scheme for compressible multimaterial models in 3D. *J. Comput. Phys.*, **313**, 121–143.

De Chizelle, Y. K., Ceccio, S. L., & Brennen, C. E. 1995. Observations and scaling of travelling bubble cavitation. *J. Fluid Mech.*, **293**, 99–126.

Despres, B. 2007. A geometrical approach to nonconservative shocks and elastoplastic shocks. *Arch. Ration. Mech. Anal.*, **186**, 275–308.

Dumbser, M., Peshkov, I., Romenski, E., & Zanotti, O. 2015. High order ADER schemes for a unified first order hyperbolic formulation of continuum mechanics: viscous heat-conducting fluids and elastic solids. *J. Comput. Phys.*, **314**, 824–862.

Duryea, A. P., Roberts, W. W., Cain, C. A., Tamaddoni, H. A., & Hall, T. L. 2014. Acoustic Bubble Removal to Enhance SWL Efficacy at High Shock Rate: An In Vitro Study. *J. Endourol.*, **28**, 90–95.

Eringen, A. C. 1962. *Nonlinear theory of continuous media*. New York, NY: McGraw-Hill.

Estrada, J. B., Barajas, C., Henann, D. L., Johnsen, E., & Franck, C. 2017. High Strain-rate Soft Material Characterization via Inertial Cavitation. *J. Mech. Phys. Solids*, **112**, 291–317.

Evje, S., & Fjelde, K. K. 2003. On a rough AUSM scheme for a one-dimensional two-phase model. *Comput. Fluids*, **32**, 1497–1530.

Favrie, N., & Gavrilyuk, S. 2011. Mathematical and numerical model for nonlinear viscoplasticity. *Philos. Trans. A. Math. Phys. Eng. Sci.*, **369**, 2864–2880.

Favrie, N., Gavrilyuk, S. L., & Saurel, R. 2009. Solid-fluid diffuse interface model in cases of extreme deformations. *J. Comput. Phys.*, **228**, 6037–6077.

Fedkiw, R. P., Marquina, A., & Merriman, B. 1999. An Isobaric Fix for the Overheating Problem in Multimaterial Compressible Flows. *J. Comput. Phys.*, **148**, 545–578.

Fogler, H. S., & Goddard, J. D. 1970. Collapse of spherical cavities in viscoelastic fluids. *Phys. Fluids*, **13**, 1135–1141.

Fourest, T., Laurens, J. M., Deletombe, E., Dupas, J., & Arrigoni, M. 2015. Confined Rayleigh-Plesset equation for Hydrodynamic Ram analysis in thin-walled containers under ballistic impacts. *Thin-Walled Struct.*, **86**, 67–72.

Franc, J.-P., Riondet, M., Karimi, A., & Chahine, G. L. 2011. Impact Load Measurements in an Erosive Cavitating Flow. *J. Fluids Eng.*, **133**, 1–8.

Franc, J. P., Riondet, M., Karimi, A., & Chahine, G. L. 2012. Material and velocity effects on cavitation erosion pitting. *Wear*, **274-275**, 248–259.

Fung, Y.-C. 1993. *Biomechanics*. New York, NY: Springer New York.

Fuster, D., & Colonius, T. 2011. Modelling bubble clusters in compressible liquids. *J. Fluid Mech.*, **688**, 352–389.

Ganesh, H., Mäkiharju, S. A., & Ceccio, S. L. 2016. Bubbly shock propagation as a mechanism for sheet-to-cloud transition of partial cavities. *J. Fluid Mech.*, **802**, 37–78.

Gaudron, R., Warnez, M. T., & Johnsen, E. 2015. Bubble dynamics in a viscoelastic medium with nonlinear elasticity. *J. Fluid Mech.*, **766**, 54–75.

Gavrilyuk, S. L., Favrie, N., & Saurel, R. 2008. Modelling wave dynamics of compressible elastic materials. *J. Comput. Phys.*, **227**, 2941–2969.

Gibson, D. C., & Blake, J. R. 1982. The growth and collapse of bubbles near deformable surfaces. *Appl. Sci. Res.*, **38**, 215–224.

Gnanaskandan, A., & Mahesh, K. 2015. A numerical method to simulate turbulent cavitating flows. *Int. J. Multiph. Flow*, **70**, 22–34.

Godunov, S. K., & Romenskii, E. I. 1972. Nonstationary equations of nonlinear elasticity theory in eulerian coordinates. *J. Appl. Mech. Tech. Phys.*, **13**, 868–884.

Godunov, S. K., & Romenskii, E. I. 2003. *Elements of Continuum Mechanics and Conservation Laws*. Boston, MA: Springer US.

Gorsse, Y., Iollo, A., Milcent, T., & Telib, H. 2014. A simple Cartesian scheme for compressible multimaterials. *J. Comput. Phys.*, **272**, 772–798.

Gottlieb, S., & Shu, C.-W. 1998. Total variation diminishing Runge-Kutta schemes. *Math. Comput. Am. Math. Soc.*, **67**, 73–85.

Gregorčič, P., Petkovšek, R., & Možina, J. 2007. Investigation of a cavitation bubble between a rigid boundary and a free surface. *J. Appl. Phys.*, **102**, 1–8.

Grétarsson, J. T., & Fedkiw, R. 2013. Fully conservative leak-proof treatment of thin solid structures immersed in compressible fluids. *J. Comput. Phys.*, **245**, 160–204.

Grujicic, A., Laberge, M., Grujicic, M., Pandurangan, B., Runt, J., Tarter, J., & Dillon, G. 2012. Potential improvements in shock-mitigation efficacy of a polyurea-augmented advanced combat helmet. *J. Mater. Eng. Perform.*, **21**, 1562–1579.

Haas, J.-F. F., & Sturtevant, B. 1987. Interaction of weak shock waves with cylindrical and spherical gas inhomogeneities. *J. Fluid Mech.*, **181**, 41–76.

Haines, J. R., McManamy, T. J., Gabriel, T. A., Battle, R. E., Chipley, K. K., Crabtree, J. A., Jacobs, L. L., Lousteau, D. C., Rennich, M. J., & Riemer, B. W. 2014. Spallation neutron source target station design, development, and commissioning. *Nucl. Instruments Methods Phys. Res. Sect. A Accel. Spectrometers, Detect. Assoc. Equip.*, **764**, 94–115.

Harlow, F. H., & Amsden, A. A. 1971. *Fluid Dynamics*. Los Alamos, NM: Los Alamos Scientific Laboratory.

Harten, A., Lax, P. D., & van Leer, B. 1983. On Upstream Differencing and Godunov-Type Schemes for Hyperbolic Conservation Laws. *SIAM Rev.*, **25**, 35–61.

Hawker, N. A., & Ventikos, Y. 2012. Interaction of a strong shockwave with a gas bubble in a liquid medium: a numerical study. *J. Fluid Mech.*, **701**, 59–97.

Henderson, L. F., Colella, P., & Puckett, E. G. 1991. On the refraction of shock waves at a slowfast gas interface. *J. Fluid Mech.*, **224**, 1–27.

Henry de Frahan, M. T., Varadan, S., & Johnsen, E. 2015. A new limiting procedure for discontinuous Galerkin methods applied to compressible multiphase flows with shocks and interfaces. *J. Comput. Phys.*, **280**, 489–509.

Holmer, N., Almquist, L., Hertz, T., Holm, A., Lindstedt, E., Persson, H., & Hertz, C. 1991. On the mechanism of kidney stone disintegration by acoustic shock waves. *Ultrasound Med. Biol.*, **17**, 479–489.

Hsiao, C.-T. T., Choi, J.-K. K., Singh, S., Chahine, G. L., Hay, T. A., Ilinskii, Y. A., Zabolotskaya, E. A., Hamilton, M. F., Sankin, G., Yuan, F., & Zhong, P. 2013. Modelling single- and tandem-bubble dynamics between two parallel plates for biomedical applications. *J. Fluid Mech.*, **716**, 137–170.

Hsiao, C.-T., Jayaprakash, A., Kapahi, A., Choi, J.-K., & Chahine, G. L. 2014. Modelling of material pitting from cavitation bubble collapse. *J. Fluid Mech.*, **755**, 142–175.

Hua, C., & Johnsen, E. 2013. Nonlinear oscillations following the Rayleigh collapse of a gas bubble in a linear viscoelastic (tissue-like) medium. *Phys. Fluids*, **25**, 1–22.

Jiang, G.-S., & Shu, C.-W. 1996. Efficient Implementation of Weighted ENO Schemes. *J. Comput. Phys.*, **126**, 202–228.

Johnsen, E., & Colonius, T. 2009a. Numerical simulations of non-spherical bubble collapse. *J. Fluid Mech.*, **629**, 231–262.

Johnsen, E. 2011. On the treatment of contact discontinuities using WENO schemes. *J. Comput. Phys.*, **230**, 8665–8668.

Johnsen, E. 2012. An Interface-Capturing Scheme for Direct Simulations of Bubble Dynamics with Viscous and Thermal Diffusion. *Pages 13–19 of: Proc. 8th Int. Symp. Cavitation*. Singapore: Research Publishing Services.

Johnsen, E. 2013. Analysis of Numerical Errors Generated by Slowly Moving Shock Waves. *AIAA J.*, **51**, 1269–1274.

Johnsen, E., & Colonius, T. 2006. Implementation of WENO schemes in compressible multicomponent flow problems. *J. Comput. Phys.*, **219**, 715–732.

Johnsen, E., & Colonius, T. 2008. Shock-induced collapse of a gas bubble in shockwave lithotripsy. *J. Acoust. Soc. Am.*, **124**, 2011–2020.

Johnsen, E., & Colonius, T. 2009b. *Numerical simulations of non-spherical bubble collapse with applications to shockwave lithotripsy*. Ph.D. thesis, California Institute of Technology.

Kalateh, F., & Koosheh, A. 2018. Finite Element Analysis of Flexible Structure and Cavitating Nonlinear Acoustic Fluid Interaction under Shock Wave Loading. *Int. J. Nonlinear Sci. Numer. Simul.*, **19**, 459–473.

Kapahi, A., & Udaykumar, H. S. 2013. Dynamics of void collapse in shocked energetic materials: Physics of void-void interactions. *Shock Waves*, **23**, 537–558.

Kapahi, A., & Udaykumar, H. S. 2015. Three-dimensional simulations of dynamics of void collapse in energetic materials. *Shock Waves*, **25**, 177–187.

Kapahi, A., Sambasivan, S., & Udaykumar, H. S. 2013a. A three-dimensional sharp interface Cartesian grid method for solving high speed multi-material impact, penetration and fragmentation problems. *J. Comput. Phys.*, **241**, 308–332.

Kapahi, A., Sambasivan, S., & Udaykumar, H. S. 2013b. Simulation of collapse and fragmentation phenomena in a sharp interface Eulerian setting. *Comput. Fluids*, **87**, 26–40.

Kapahi, A., Sambasivan, S. K., & Udaykumar, H. 2011. Shock wave Interaction with Voids in Heterogeneous Energetic Material. *Pages 1–29 of: 20th AIAA Comput. Fluid Dyn. Conf.* Reston, Virigina: American Institute of Aeronautics and Astronautics.

Kapila, A. K., Menikoff, R., Bdzil, J. B., Son, S. F., & Stewart, D. S. 2001. Two-phase modeling of deflagration-to-detonation transition in granular materials: Reduced equations. *Phys. Fluids*, **13**, 3002–3024.

Kim, K.-H., Chahine, G., Franc, J.-P., & Karimi, A. (eds). 2014. *Advanced Experimental and Numerical Techniques for Cavitation Erosion Prediction*. Fluid Mechanics and Its Applications, vol. 106. Dordrecht: Springer Netherlands.

Kitamura, K., Liou, M. S., & Chang, C. H. 2014. Extension and comparative study of AUSM-family schemes for compressible multiphase flow simulations. *Commun. Comput. Phys.*, **16**, 632–674.

Klatt, D., Hamhaber, U., Asbach, P., Braun, J., & Sack, I. 2007. Noninvasive assessment of the rheological behavior of human organs using multifrequency MR elastography: a study of brain and liver viscoelasticity. *Phys. Med. Biol.*, **52**, 7281–7294.

Knapp, R. T. 1955. Recent Investigations of the Mechanics of Cavitation and Cavitation Damage. *Trans. ASME*, **77**, 1045–1054.

Kornfeld, M., & Suvorov, L. 1944. On the destructive action of cavitation. *J. Appl. Phys.*, **15**, 495–506.

Krimmel, J., Colonius, T., & Tanguay, M. 2010. Simulation of the effects of cavitation and anatomy in the shock path of model lithotripters. *Urol. Res.*, **38**, 505–518.

Kulikovskii, A., Pogorelov, N., Semenov, A., & Piechor, K. 2002. Mathematical Aspects of Numerical Solution of Hyperbolic Systems. Monographs and Surveys in Pure and Applied Mathematics, Vol. 118. *Appl. Mech. Rev.*, **55**.

Lauterborn, W., & Bolle, H. 1975. Experimental investigations of cavitation-bubble collapse in the neighbourhood of a solid boundary. *J. Fluid Mech.*, **72**, 391–399.

Lauterborn, W., & Kurz, T. 2010. Physics of bubble oscillations. *Reports Prog. Phys.*, **73**, 1–88.

Le Floch, P., & Olsson, F. 1990. A second-order Godunov method for the conservation laws of nonlinear elastodynamics. *Impact Comput. Sci. Eng.*, **2**, 318–354.

Le Métayer, O., Massoni, J., & Saurel, R. 2005. Modelling evaporation fronts with reactive Riemann solvers. *J. Comput. Phys.*, **205**, 567–610.

Le Métayer, O., & Saurel, R. 2016. The Noble-Abel Stiffened-Gas equation of state. *Phys. Fluids*, **28**, 1–22.

Lindau, O., & Lauterborn, W. 2003. Cinematographic observation of the collapse and rebound of a laser-produced cavitation bubble near a wall. *J. Fluid Mech.*, **479**, 327–348.

Liou, M. S. 1992. On a new class of flux splittings. *Pages 115–119 of: Thirteen. Int. Conf. Numer. Methods Fluid Dyn.* Berlin, Heidelberg: Springer Berlin Heidelberg.

Liou, M.-S., Chang, C.-H., Nguyen, L., & Theofanous, T. G. 2008. How to Solve Compressible Multifluid Equations: a Simple, Robust, and Accurate Method. *AIAA J.*, **46**, 2345–2356.

Liou, M.-S. 1996. A Sequel to AUSM: AUSM+. *J. Comput. Phys.*, **129**, 364–382.

Liou, M.-S. 2006. A sequel to AUSM, Part II: AUSM+-up for all speeds. *J. Comput. Phys.*, **214**, 137–170.

Liou, M.-S., & Steffen, C. J. 1993. A New Flux Splitting Scheme. *J. Comput. Phys.*, **107**, 23–39.

Liu, J., & Marsden, A. L. 2018. A unified continuum and variational multiscale formulation for fluids, solids, and fluidstructure interaction. *Comput. Methods Appl. Mech. Eng.*, **337**, 549–597.

Lombard, B., & Piraux, J. 2004. Numerical treatment of two-dimensional interfaces for acoustic and elastic waves. *J. Comput. Phys.*, **195**, 90–116.

Lombard, B., & Piraux, J. 2011. Numerical modeling of transient two-dimensional viscoelastic waves. *J. Comput. Phys.*, **230**, 6099–6114.

López Ortega, A., Lombardini, M., & Hill, D. J. 2011. Converging shocks in elastic-plastic solids. *Phys. Rev. E*, **84**, 1–21.

López Ortega, A., Lombardini, M., Pullin, D., & Meiron, D. 2014. Numerical simulation of elastic-plastic solid mechanics using an Eulerian stretch tensor approach and HLLD Riemann solver. *J. Comput. Phys.*, **257**, 414–441.

López Ortega, A., Lombardini, M., Barton, P., Pullin, D., & Meiron, D. 2015. RichtmyerMeshkov instability for elasticplastic solids in converging geometries. *J. Mech. Phys. Solids*, **76**, 291–324.

Lubock, P. 1989. The physics and mechanics of lithotripters. *Dig. Dis. Sci.*, **34**, 999–1005.

Luo, H., Baum, J. D., & Löhner, R. 2004. On the computation of multi-material flows using ALE formulation. *J. Comput. Phys.*, **194**, 304–328.

Massoni, J., Saurel, R., Nkonga, B., & Abgrall, R. 2002. Proposition de méthodes et modèles eulériens pour les problèmes à interfaces entre fluides compressibles en présence de transfert de chaleur. *Int. J. Heat Mass Transf.*, **45**, 1287–1307.

McGurn, M. T., Ruggirello, K. P., & DesJardin, P. E. 2013. An Eulerian-Lagrangian moving immersed interface method for simulating burning solids. *J. Comput. Phys.*, **241**, 364–387.

Meng, J. C., & Colonius, T. 2018. Numerical simulation of the aerobreakup of a water droplet. *J. Fluid Mech.*, **835**, 1108–1135.

Mihradi, S., Homma, H., & Kanto, Y. 2004. Numerical Analysis of Kidney Stone Fragmentation by Short Pulse Impingement. *JSME Int. J. Ser. A*, **47**, 581–590.

Miller, G. H. 2004. An iterative Riemann solver for systems of hyperbolic conservation laws, with application to hyperelastic solid mechanics. *J. Comput. Phys.*, **193**, 198–225.

Miller, G. H., & Colella, P. 2001. A High-Order Eulerian Godunov Method for Elastic-Plastic Flow in Solids. *J. Comput. Phys.*, **167**, 131–176.

Miller, G., & Colella, P. 2002. A Conservative Three-Dimensional Eulerian Method for Coupled Solid-Fluid Shock Capturing. *J. Comput. Phys.*, **183**, 26–82.

Moës, N., & Belytschko, T. 2002. Extended finite element method for cohesive crack growth. *Eng. Fract. Mech.*, **69**, 813–833.

Morro, A. 2017. A thermodynamic Approach to Rate Equations in Continuum Physics. *J. Phys. Sci. Appl.*, **7**, 15–23.

Murrone, A., & Guillard, H. 2005. A five equation reduced model for compressible two phase flow problems. *J. Comput. Phys.*, **202**, 664–698.

Naoe, T., Kogawa, H., Wakui, T., Haga, K., Teshigawara, M., Kinoshita, H., Takada, H., & Futakawa, M. 2016. Cavitation damage prediction for the JSNS mercury target vessel. *J. Nucl. Mater.*, **468**, 313–320.

Naude, C. F., & Ellis, A. T. 1961. On the Mechanism of Cavitation Damage by Nonhemispherical Cavities Collapsing in Contact With a Solid Boundary. *J. Basic Eng.*, **83**, 648.

Ndanou, S., Favrie, N., & Gavrilyuk, S. 2013. Criterion of Hyperbolicity in Hyperelasticity in the Case of the Stored Energy in Separable Form. *J. Elast.*, **115**, 1–25.

Ndanou, S., Favrie, N., & Gavrilyuk, S. 2015. Multi-solid and multi-fluid diffuse interface model: Applications to dynamic fracture and fragmentation. *J. Comput. Phys.*, **295**, 523–555.

Niu, Y.-Y., Lin, Y.-C., & Chang, C.-H. 2008. A further work on multi-phase two-fluid approach for compressible multi-phase flows. *Int. J. Numer. Methods Fluids*, **58**, 879–896.

Noblin, X., Rojas, N. O., Westbrook, J., Llorens, C., Argentina, M., & Dumais, J. 2012. The Fern Sporangium: A Unique Catapult. *Science*, **335**, 1322–1322.

Noh, W. 1987. Errors for calculations of strong shocks using an artificial viscosity and an artificial heat flux. *J. Comput. Phys.*, **72**, 78–120.

Nourgaliev, R., Dinh, T., & Theofanous, T. 2006. Adaptive characteristics-based matching for compressible multifluid dynamics. *J. Comput. Phys.*, **213**, 500–529.

Oguz, H. N., & Prosperetti, A. 1998. The natural frequency of oscillation of gas bubbles in tubes. *J. Acoust. Soc. Am.*, **103**, 3301–3308.

Paillère, H., Corre, C., & García Cascales, J. R. 2003. On the extension of the AUSM+ scheme to compressible two-fluid models. *Comput. Fluids*, **32**, 891–916.

Palacio-Torralba, J., Hammer, S., Good, D. W., Alan McNeill, S., Stewart, G. D., Reuben, R. L., & Chen, Y. 2015. Quantitative diagnostics of soft tissue through viscoelastic characterization using time-based instrumented palpation. *J. Mech. Behav. Biomed. Mater.*, **41**, 149–160.

Pandare, A. K., & Luo, H. 2018. A robust and efficient finite volume method for compressible inviscid and viscous two-phase flows. *J. Comput. Phys.*, **371**, 67–91.

Pandolfi, M., & D'Ambrosio, D. 2001. Numerical Instabilities in Upwind Methods: Analysis and Cures for the"Carbuncle" Phenomenon. *J. Comput. Phys.*, **166**, 271–301.

Parsons, C. A., & Cook, S. S. 1919. Investigations into the causes of corrosion or erosion of propellers. *J. Am. Soc. Nav. Eng.*, **31**, 536–541.

Patterson, B., & Johnsen, E. 2018. Growth of liquid-gas interfacial perturbations driven by acoustic waves. *Phys. Rev. Fluids*, **3**, 1–22.

Pelanti, M., & Shyue, K. M. 2014. A mixture-energy-consistent six-equation two-phase numerical model for fluids with interfaces, cavitation and evaporation waves. *J. Comput. Phys.*, **259**, 331–357.

Perigaud, G., & Saurel, R. 2005. A compressible flow model with capillary effects. *J. Comput. Phys.*, **209**, 139–178.

Philipp, A., & Lauterborn, W. 1998. Cavitation erosion by single laser-produced bubbles. *J. Fluid Mech.*, **361**, 75–116.

Pishchalnikov, Y. A., Sapozhnikov, O. A., Bailey, M. R., Williams, J. C., Cleveland, R. O., Colonius, T., Crum, L. A., Evan, A. P., & McAteer, J. A. 2003. Cavitation Bubble Cluster Activity in the Breakage of Kidney Stones by Lithotripter Shockwaves. *J. Endourol.*, **17**, 435–446.

Plesset, M. S., & Chapman, R. B. 1971. Collapse of an initially spherical vapour cavity in the neighbourhood of a solid boundary. *J. Fluid Mech.*, **47**, 283–290.

Plohr, B. J., & Sharp, D. H. 1988. A conservative Eulerian formulation of the equations for elastic flow. *Adv. Appl. Math.*, **9**, 481–499.

Qiao, J., Amirkhizi, A. V., Schaaf, K., Nemat-Nasser, S., & Wu, G. 2011. Dynamic mechanical and ultrasonic properties of polyurea. *Mech. Mater.*, **43**, 598–607.

Quirk, J. J., & Karni, S. 1996. On the dynamics of a shockbubble interaction. *J. Fluid Mech.*, **318**, 129–163.

Radovitzky, R., & Ortiz, M. 1999. Error estimation and adaptive meshing in strongly nonlinear dynamic problems. *Comput. Methods Appl. Mech. Eng.*, **172**, 203–240.

Rayleigh, L. 1917. On the pressure developed in a liquid during the collapse of a spherical cavity. *London, Edinburgh, Dublin Philos. Mag. J. Sci.*, **34**, 94–98.

Reisman, G. E., Wang, Y.-C., & Brennen, C. E. 1998. Observations of shock waves in cloud cavitation. *J. Fluid Mech.*, **355**, 255–283.

Riemer, B. W., McClintock, D. A., Kaminskas, S., & Abdou, A. A. 2014. Correlation between simulations and cavitation-induced erosion damage in Spallation Neutron Source target modules after operation. *J. Nucl. Mater.*, **450**, 183–191.

Rijensky, O., & Rittel, D. 2016. Polyurea coated aluminum plates under hydrodynamic loading: Does side matter? *Int. J. Impact Eng.*, **98**, 1–12.

Robertsson, J. O. A., Blanch, J. O., & Symes, W. W. 1994. Viscoelastic finite-difference modeling. *Geophysics*, **59**, 1444–1456.

Rodriguez, M., & Johnsen, E. 2018. A high-order accurate, five-equations compressible multiphase approach for viscoelastic fluids and solids with relaxation and elasticity. *J. Comput. Phys.*, Under review.

Rodriguez, M., Powell, K. G., & Johnsen, E. 2018. A high-order accurate AUSM$^+$-up approach for simulations of compressible multiphase flows with linear viscoelasticity. *Shock Waves*, Submitted.

Sambasivan, S. K., & UdayKumar, H. S. 2009. Ghost Fluid Method for Strong Shock Interactions Part 2: Immersed Solid Boundaries. *AIAA J.*, **47**, 2923–2937.

Samiee, A., Amirkhizi, A. V., & Nemat-Nasser, S. 2013. Numerical study of the effect of polyurea on the performance of steel plates under blast loads. *Mech. Mater.*, **64**, 1–10.

Sass, W., Bräunlich, M., Dreyer, H.-P., Matura, E., Folberth, W., Priesmeyer, H.-G., & Seifert, J. 1991. The mechanisms of stone disintegration by shock waves. *Ultrasound Med. Biol.*, **17**, 239–243.

Saurel, R., & Abgrall, R. 1999a. A Multiphase Godunov Method for Compressible Multifluid and Multiphase Flows. *J. Comput. Phys.*, **150**, 425–467.

Saurel, R., & Abgrall, R. 1999b. A Simple Method for Compressible Multifluid Flows. *SIAM J. Sci. Comput.*, **21**, 1115–1145.

Saurel, R., & Lemetayer, O. 2001. A multiphase model for compressible flows with interfaces, shocks, detonation waves and cavitation. *J. Fluid Mech.*, **431**, 239–271.

Saurel, R., Petitpas, F., & Berry, R. A. 2009. Simple and efficient relaxation methods for interfaces separating compressible fluids, cavitating flows and shocks in multiphase mixtures. *J. Comput. Phys.*, **228**, 1678–1712.

Scandaliato, A. L., & Liou, M.-S. 2012. AUSM-Based High-Order Solution for Euler Equations. *Commun. Comput. Phys.*, **12**, 1096–1120.

Schmidmayer, K., Petitpas, F., Daniel, E., Favrie, N., & Gavrilyuk, S. 2017. A model and numerical method for compressible flows with capillary effects. *J. Comput. Phys.*, **334**, 468–496.

Schoch, S., Nordin-Bates, K., & Nikiforakis, N. 2013. An Eulerian algorithm for coupled simulations of elastoplastic-solids and condensed-phase explosives. *J. Comput. Phys.*, **252**, 163–194.

Seo, J. H., Lele, S. K., & Tryggvason, G. 2010. Investigation and modeling of bubble-bubble interaction effect in homogeneous bubbly flows. *Phys. Fluids*, **22**, 1–19.

Shen, C., Qiu, J.-M., & Christlieb, A. 2011. Adaptive mesh refinement based on high order finite difference WENO scheme for multi-scale simulations. *J. Comput. Phys.*, **230**, 3780–3802.

Shima, E., & Kitamura, K. 2011. Parameter-Free Simple Low-Dissipation AUSM-Family Scheme for All Speeds. *AIAA J.*, **49**, 1693–1709.

Shukla, R. K., Pantano, C., & Freund, J. B. 2010. An interface capturing method for the simulation of multi-phase compressible flows. *J. Comput. Phys.*, **229**, 7411–7439.

Shyue, K.-M. 1998. An Efficient Shock-Capturing Algorithm for Compressible Multicomponent Problems. *J. Comput. Phys.*, **142**, 208–242.

Supponen, O., Obreschkow, D., Tinguely, M., Kobel, P., Dorsaz, N., & Farhat, M. 2016. Scaling laws for jets of single cavitation bubbles. *J. Fluid Mech*, **802**, 263–293.

Surana, K. S., Ma, Y., Romkes, A., & Reddy, J. N. 2010. The Rate Constitutive Equations and Their Validity for Progressively Increasing Deformation. *Mech. Adv. Mater. Struct.*, **17**, 509–533.

Šuštarič, P., Seabra, M. R., Cesar De Sa, J. M., & Rodič, T. 2014. Sensitivity analysis based crack propagation criterion for compressible and (near) incompressible hyperelastic materials. *Finite Elem. Anal. Des.*, **82**, 1–15.

Swantek, A. B., & Austin, J. M. 2010. Collapse of void arrays under stress wave loading. *J. Fluid Mech.*, **649**, 399–427.

Tanasawa, I., & Yang, W. J. 1970. Dynamic behavior of a gas bubble in viscoelastic liquids. *J. Appl. Phys.*, **41**, 4526–4531.

Tanguay, M. 2004. *Computation of bubbly cavitating flow in shock wave lithotripsy*. Ph.D. thesis, California Institute of Technology.

Theofanous, T. G., Li, G. J., & Dinh, T. N. 2004. Aerobreakup in Rarefied Supersonic Gas Flows. *J. Fluids Eng.*, **126**, 516–527.

Thompson, K. W. 1990. Time-dependent boundary conditions for hyperbolic systems, II. *J. Comput. Phys.*, **89**, 439–461.

Titarev, V. A., & Toro, E. F. 2002. ADER: Arbitrary high order godunov approach. *J. Sci. Comput.*, **17**, 609–618.

Tiwari, A., Freund, J. B., & Pantano, C. 2013. A diffuse interface model with immiscibility preservation. *J. Comput. Phys.*, **252**, 290–309.

Tomita, Y., & Shima, A. 1986. Mechanisms of impulsive pressure generation and damage pit formation by bubble collapse. *J. Fluid Mech.*, **169**, 535–564.

Tomita, Y., Robinson, P. B., Tong, R. P., & Blake, J. R. 2002. Growth and collapse of cavitation bubbles near a curved rigid boundary. *J. Fluid Mech.*, **466**, 259–283.

Tran, L., & Udaykumar, H. S. 2006a. Simulation of Void Collapse in an Energetic Material, Part 2: Reactive Case. *J. Propuls. Power*, **22**, 959–974.

Tran, L., & Udaykumar, H. S. 2006b. Simulation of Void Collapse in an Energetic Material, Part I: Inert Case. *J. Propuls. Power*, **22**, 947–958.

Tran, L., & Udaykumar, H. 2004. A particle-level set-based sharp interface cartesian grid method for impact, penetration, and void collapse. *J. Comput. Phys.*, **193**, 469–510.

Trangenstein, J. A., & Colella, P. 1991. A higher-order Godunov method for modeling finite deformation in elastic-plastic solids. *Commun. Pure Appl. Math.*, **44**, 41–100.

Udaykumar, H. S., Tran, L., Belk, D. M., & Vanden, K. J. 2003. An Eulerian method for computation of multimaterial impact with ENO shock-capturing and sharp interfaces. *J. Comput. Phys.*, **186**, 136–177.

Ván, P., Berezovski, A., & Papenfuss, C. 2014. Thermodynamic approach to generalized continua. *Contin. Mech. Thermodyn.*, **26**, 403–420.

Versluis, M., Schmitz, B., Heydt, A. V. D., Lohse, D., Smith, J. M., Szathmary, E., & Tran, T. M. 2010. Snapping Shrimp Through Cavitating Snap : Bubbles. *Science*, **289**, 2114–2117.

Vincent, O., & Marmottant, P. 2017. On the statics and dynamics of fully confined bubbles. *J. Fluid Mech.*, **827**, 194–224.

Vincent, O., Marmottant, P., Quinto-Su, P. A., & Ohl, C. D. 2012. Birth and growth of cavitation bubbles within water under tension confined in a simple synthetic tree. *Phys. Rev. Lett.*, **108**, 1–5.

Vincent, O., Marmottant, P., Gonzalez-Avila, S. R., Ando, K., & Ohl, C. D. 2014. The fast dynamics of cavitation bubbles within water confined in elastic solids. *Soft Matter*, **10**, 1455–1461.

Vlaisavljevich, E., Lin, K.-W., Warnez, M. T., Singh, R., Mancia, L., Putnam, A. J., Johnsen, E., Cain, C., & Xu, Z. 2015. Effects of tissue stiffness, ultrasound frequency, and pressure on histotripsy-induced cavitation bubble behavior. *Phys. Med. Biol.*, **60**, 2271–2292.

Wang, K. G., Lea, P., & Farhat, C. 2015. A computational framework for the simulation of high-speed multi-material fluid-structure interaction problems with dynamic fracture. *Int. J. Numer. Methods Eng.*, **104**, 585–623.

Wang, Q. 1998. The Evolution of a Gas Bubble Near an Inclined Wall. *Theor. Comput. Fluid Dyn.*, **12**, 29–51.

Wang, Y.-C., & Brennen, C. E. 1999. Numerical Computation of Shock Waves in a Spherical Cloud of Cavitation Bubbles. *J. Fluids Eng.*, **121**, 872–880.

Wang, Y., Quaini, A., & Čanić, S. 2018. A Higher-Order Discontinuous Galerkin/Arbitrary Lagrangian Eulerian Partitioned Approach to Solving FluidStructure Interaction Problems with Incompressible, Viscous Fluids and Elastic Structures. *J. Sci. Comput.*, **76**, 481–520.

Wang, Y., Qiu, L., Reitz, R. D., & Diwakar, R. 2014. Simulating cavitating liquid jets using a compressible and equilibrium two-phase flow solver. *Int. J. Multiph. Flow*, **63**, 52–67.

Warnez, M. T., & Johnsen, E. 2015. Numerical modeling of bubble dynamics in viscoelastic media with relaxation. *Phys. Fluids*, **27**, 1–28.

Weinberg, K., & Ortiz, M. 2009. Kidney damage in extracorporeal shock wave lithotripsy: A numerical approach for different shock profiles. *Biomech. Model. Mechanobiol.*, **8**, 285–299.

Wineman, A. S. 2000. *Mechanical Response of Polymers: An Introduction*. Cambridge University Press.

Yang, X., & Church, C. C. 2005. A model for the dynamics of gas bubbles in soft tissue. *J. Acoust. Soc. Am.*, **118**, 3595–3606.

Young, Y. L., Liu, Z., & Xie, W. 2009. Fluid-Structure and Shock-Bubble Interaction Effects During Underwater Explosions Near Composite Structures. *J. Appl. Mech.*, **76**, 1–10.

Zener, C. 1947. Mechanical Behavior of High Damping Metals. *J. Appl. Phys.*, **18**, 1022–1025.

Zhang, D. Z., & Prosperetti, A. 1994. Ensemble phase-averaged equations for bubbly flows. *Phys. Fluids*, **6**, 2956–2970.

Zhong, P., Chuong, C. J., & Preminger, G. M. 1993. Propagation of shock waves in elastic solids caused by cavitation microjet impact. II: Application in extracorporeal shock wave lithotripsy. *J. Acoust. Soc. Am.*, **94**, 29–36.

Zhu, S., Cocks, F. H., Preminger, G. M., & Zhong, P. 2002. The role of stress waves and cavitation in stone comminution in shock wave lithotripsy. *Ultrasound Med. Biol.*, **28**, 661–671.